EFFECTS OF TURBULENT FLOW REGIME ON PILOT AND PERFORATED PLATE STABILIZED LEAN PREMIXED FLAMES

A Dissertation

Submitted to the Faculty

of

Purdue University

by

Jupyoung Kim

In Partial Fulfillment of the

Requirements for the Degree

of

Doctor of Philosophy

August 2019

Purdue University

West Lafayette, Indiana

THE PURDUE UNIVERSITY GRADUATE SCHOOL
STATEMENT OF DISSERTATION APPROVAL

Dr. Jay P. Gore, Chair

School of Aeronautics and Astronautics

Dr. Robert P. Lucht

School of Aeronautics and Astronautics

Dr. Steven T. Wereley

School of Mechanical Engineering

Dr. Carson Slabaugh

School of Aeronautics and Astronautics

Approved by:

Dr. Weinong Chen

Head of the Graduate Program

To my wife See-eun Choi
and my son Levi Junsang Kim

ACKNOWLEDGMENTS

My most sincere appreciation goes to Professor Jay P. Gore who has provided me with opportunities and supports I could have had. He has professionally guided me to fascinating and diverse research environments. Most importantly, he allowed me to explore experimental data in various aspects which provided me to have this achievement.

I also gratefully thank Professor Robert P. Lucht for offering immense technical guidance in combustion diagnostics. His guidance has been important in the achievements. My appreciation is also continued to Professor Steven T. Wereley who has advised me for particle image velocimetry. Thanks are also due to Professor Carson Slabaugh for educating me about gas turbine engines.

My appreciation is extended to Dr. Aman Satija and Dr. Dong Han for their extensive help in experiments and technical discussions. I thank Veeraraghava Raju Hasti for his help in the design of the experimental apparatus. I also thank Dr. Jongmook Lim, Vikrant Goyal, Rathziel Roncancio, Seunghyun Jo, Yerbatyr Tursyn, Abhishek Navarkar, Mehmed Ulcay, Elihu Deneke, Luke Dillard, Tianxiao Yu, Hashad Lalit, Oluwatobi Busari, and Mingming Gu for valuable discussions.

I am grateful to my wife See-eun for her love and supports to me even in a lone faraway country. I am grateful to my son Junsang for giving delightful love to us. I am grateful to my parents Jijun and Sunnam and my parents in-law Yonseob and Miok for their love and sacrifice. I am grateful to my brother Juyoung and his wife Dabin for taking care of parents instead of me.

I would like to acknowledge the financial support provided by U.S. Department of Energy and Division of Chemical Sciences, Biosciences, and Geosciences (Grant No. DE-FG02-03ER15391) and U.S. Department of Energy, University Turbine Systems

Research Program, and National Energy Technology Laboratory (Grant No. DE-FE0011822).

TABLE OF CONTENTS

Page

LIST OF TABLES viii

LIST OF FIGURES ix

NOMENCLATURE xiv

ABSTRACT xvi

1 INTRODUCTION 1

1.1 Combustion and our life 1

1.2 Combustion 7

1.3 Premixed flames 8

1.4 Turbulent premixed flames 9

1.5 Motivation and objectives 13

2 LITERATURE REVIEW 15

2.1 Turbulent premixed flames 15

2.2 Turbulence generator: perforated plate 26

2.3 Particle image velocimetry 32

2.4 Planar laser-induced fluorescence 38

3 PREMIXED AXISYMMETRIC REACTOR ASSISTED TURBULENT BURENR 41

3.1 Burner design 41

3.2 Specification of turbulence generator plates 43

3.3 Degree of mixing of PARAT burner 45

3.3.1 Experimental setup of acetone PLIF 47

3.4 Capabilities for high temperature and high pressure testing 49

3.5 Capabilities for atmospheric pressure testing 50

4 OPERATING CONDITIONS AND FLAME IMAGES 54

Page

4.1 Operating Conditions 54
4.2 Flame Images 56
5 PARTICLE IMAGE VELOCIMETRY ON TURBULENT PREMIXED FLAMES64
5.1 Stereoscopic particle image velocimetry 64
5.2 Experimental setup 66
5.3 PIV processing 68
5.4 Results and discussion 72
6 OH PLANAR LASER-INDUCED FLUORESCENCE ON TURBULENT PREMIXED FLAMES 88
6.1 Experimental setup 88
6.2 OH PLIF data processing 89
6.3 Results and discussion 91
6.3.1 OH PLIF image 91
6.3.2 Mean progress variable 93
6.3.3 Flame brush thickness 96
6.3.4 Flame surface density 97
6.3.5 Global consumption speed 100
7 CONCLUSION 109
REFERENCES 113

LIST OF TABLES

Table Page

3.1 Operating condition of PARAT burner at high pressure and temperature . 50

4.1 Operating condition of PARAT burner at atmospheric pressure 55

5.1 Properties of flames. Axial (streamwise) mean velocity V_{mean} and rms velocity V_{rms} in m/s for B.R. 62% and B.R. 86% 79

LIST OF FIGURES

Figure Page

1.1 Annual energy consumption and production. Data distributed by U.S. Energy Information Administration (EIA) 2

1.2 (a) a photograph of general electric SGT-300 gas turbine engine from GE website, (b) a schematic of a gas turbine engine, and (c) a schematic of internal combustion engine 3

1.3 An example of a combustor of a gas turbine engine. Patent US 8,631,656 B2. (1) a cross-sectional view illustration of a gas turbine engine combustor with an array of fuel burners. (2) to (7) is six sequential arrays of injectors of the combustor. 6

2.1 Schematics of the turbulent flame front and brush. (a) an example of instantaneous flame front marked by CH layer [40], (b) superposition of instantaneous flame fronts obtained at different times, (c) a turbulent flame brush associated with a time-averaged view of the same flame [11]. . 16

2.2 Contour plot of the mean progress variable $\langle C \rangle$ [43] 19

2.3 Schematic of the wrinkled area (A_T) and the area of the $\langle C \rangle = 0.5$ contour (A_L). Also, labeled are the flamelet consumption speed ($S_{F,C}$) and the turbulent brush local consumption speed ($S_{T,LC}$). [39] 24

2.4 ① Drag coefficient, ② Strouhal number, and ③ vortex zone location versus porosity [81]. Porosity = 1 - B.R.. Castro [81] discovered that the turbulent flow generated by a perforated plate can be divided into two distinct regimes. 29

2.5 ① The normalized pressure drop, ② the normalized centerline velocity by inlet velocity, and ③ turbulence intensity as a function of downstream locations generated by different geometries of turbulence generator plate [87]. (a), (b), (c), and (d) represent sets of turbulence generator plates showing as figures on the left side of each graph. 31

2.6 The occurrence of the trigrams hot wire anemometry (HWA), laser Doppler velocimetry (LDV), and particle image velocimetry (PIV) in Google Books (http://books.google.com) between 1952 and 2008. The graph taken from [112] and the data taken from Google Ngrams. 33

2.7 Experimental arrangement for 2D PIV [113] 33

Figure Page

2.8 Two basic configurations for stereoscopic PIV systems: (a) translation method and (b) angular-displacement method [110] 36

2.9 Experimental arrangement for planar laser-induced fluorescence [155] . . . 39

2.10 Fluorescence phenomenon using energy level diagram from English Wikipedia39

3.1 Cross-sectional schematic of PARAT burner. 42

3.2 Photographs of PARAT burner. (Left: sideview of PARAT burner. Right: topview of PARAT burner) 44

3.3 A photograph of turbulence generator plates. 45

3.4 CAD diagram of the turbulence generator plates. Scale in inch. From top to bottom, 62 and 86 percent main turbulence generator plates and 90 percent base turbulence generator plate. 46

3.5 An image of acetone planar laser induced fluorescence. The flow consisting fuel, air, and acetone emits fluorescence showing uniform premixed condition generated from PARAT burner. 48

3.6 A radial profile of acetone intensity at the exit of the burner. It shows uniform premixed condition generated from PARAT burner. 48

3.7 Plumbing and Instrumental Diagram (P&ID) of the experimental arrangement of high-pressure and high-temperature tests 51

3.8 The control panel of LabVIEW of the high-pressure and high-temperature tests using 51

3.9 Image sequence of hydrogen pilot ignition of the PARAT burner under high-pressure and high-temperature condition. 52

3.10 Image sequence of natural gas turbulent premixed flame of the PARAT burner under high-pressure and high-temperature condition. 53

4.1 Flame images with 62 % blockage ratio of turbulence generator plate. (left to right: Re 10000, 12500, and 15000) 58

4.2 Flame images with 62 % blockage ratio of turbulence generator plate. (left to right: Re 17500, 20000, and 22500) 59

4.3 Flame images with 86 % blockage ratio of turbulence generator plate. (left to right: Re 10000, 12500, and 15000) 60

4.4 Flame images with 86 % blockage ratio of turbulence generator plate. (left to right: Re 17500 and 20000) 61

Figure Page

4.5 Procedure of image processing to determine a flame tip and an inner boundary of a potential core 62

4.6 Validation for the determination of a potential core through a flame image. Figure (a), (b), and (c) are from image processing. (d) is temperature profile measured by coherent anti-Stokes scattering (CARS) 63

5.1 Experimental setup of the stereo PIV system applied to characterize flow field of flames of PARAT burner. 67

5.2 A single-level calibration plate used to to build a three-dimensional mapping model for stereo PIV reconstruction as well as to align the laser sheet and cameras. The left image is a view from left side w.r.t the center of the burner. The right image is a view from right side w.r.t the center of the burner. 68

5.3 Seeded particle images of non-reacting flow (left) and reacting flow (right). The images are after background removal and intensity normalization . . . 70

5.4 A disparity map showing a misalignment between the laser sheet and the image plane. 71

5.5 Ensemble-averaged velocity profiles. Velocity profiles of non-reacting flow (left) and reacting flow (right) of 62 % B.R. Reynolds number is 10,000 . . 73

5.6 Velocity profiles along radial direction. Velocity profiles of 62 % B.R (left) and velocity profiles of 86 % B.R (right) at three axial locations, exit(x/D=0.13), x/D=2(36 mm above the exit), and x/D=4(72 mm above the exit). Reynolds number is 10,000 74

5.7 Probability density function (PDF) at three axial locations for 62 % B.R and Reynolds number 10,000. PDF is measured at the three axial locations, exit, 2D(36 mm above the exit), and 4D(72 mm above the exit) along the center of the burner exit. 76

5.8 Probability density function (PDF) at three axial locations for 86 % B.R and Reynolds number 10,000. PDF is measured at the three axial locations, exit, 2D(36 mm above the exit), and 4D(72 mm above the exit) along the center of the burner exit 77

5.9 Streamwise velocity profiles along radial direction for all Reynolds numbers performed in this study. Streamwise velocity profiles of 62 % B.R (left) and velocity profiles of 86 % B.R (right) at three axial locations, exit, 2D(36 mm above the exit), and 4D(72 mm above the exit). Reynolds numbers are from 10,000 to 22,500 with 2,500 interval. 78

Figure Page

5.10 Stream-wise velocity decay along the streamwise direction for B.R 62% and 86%. Normalized mean streamwise velocity (top) and normalized rms streamwise velocity (bottom) are presented. 81

5.11 Mean velocities along radial direction for both B.R.s. Re=10,000. x/D=0.13 82

5.12 RMS velocities along radial direction for both B.R.s. Re=10,000. x/D=0.13 83

5.13 An axial velocity decaying along streamwise direction for both B.R. Reynolds number is 10,000 85

5.14 Estimation of a height of a potential core for 62 % B.R using an axial velocity decaying along streamwise direction. 86

5.15 Estimation of a height of a potential core for 86 % B.R using an axial velocity decaying along the stream-wise direction. 87

6.1 Experimental setup of the OH PLIF system applied to characterize the structure of flames from PARAT burner. 89

6.2 The laser intensity profile of the sheet forming to OH PLIF. The resolution is identical for images of OH fluorescence (1024pixel x 1024pixel with 30 m per pixel). 90

6.3 The sequence of image processing for images of OH fluorescence. 91

6.4 (a) Flame image by a regular camera. (b) Instantaneous OH PLIF image. (c) Mean progress variable determined by the ensemble-averaged image of the reactant/product zones. The condition of the flames was at equivalence ratio 0.8 and Reynolds number 10,000. The image on the left side is for B.R. 62%, and the image on the right side is for B.R. 86%. 92

6.5 Mean progress variable along the radial direction for B.R. 62% and B.R. 86% at $x/D < 2.75$. The condition of the flames was at equivalence ratio 0.8 and Reynolds number 10,000. 94

6.6 Mean progress variable along the radial direction for B.R. 62% and B.R. 86% at $x/D > 2.75$. The condition of the flames was at equivalence ratio 0.8 and Reynolds number 10,000. 94

6.7 Mean progress variable along the axial direction for B.R. 62% and B.R. 86%. The condition of the flames was at Reynolds number 10,000. The lines indicate the maximum slopes of each curve. The distance in between intersections of the slope and x-axis indicates $\delta_{t,x}$ 95

Figure Page

6.8 Flame brush thickness normalized by the burner diameter along the axial direction normalized by the burner diameter. Reynolds number is 10,000. The empirical equation of flame brush thickness for the B.R. 86% requires a correction to fit with the experimental flame brush thickness, whereas the B.R. 62% does not. 97

6.9 Flame brush thickness normalized by the burner diameter along the axial direction normalized by the burner diameter. Reynolds number is 12,500. The empirical equation of flame brush thickness for the B.R. 86% requires a correction to fit with the experimental flame brush thickness, whereas the B.R. 62% does not. 98

6.10 Flame brush thickness normalized by the burner diameter along the axial direction normalized by the burner diameter. Reynolds number is 15,000. The empirical equation of flame brush thickness for the B.R. 86% requires a correction to fit with the experimental flame brush thickness, whereas the B.R. 62% does not. 99

6.11 Flame surface density vs. the mean progress variable for Reynolds number = 10000. 102

6.12 Mean flame surface density vs. the mean progress variable for the entire flame. Reynolds number = 10,000. 103

6.13 Mean flame surface density vs. the mean progress variable for the entire flame. Reynolds number = 12,500. 103

6.14 Mean flame surface density vs. the mean progress variable for the entire flame. Reynolds number = 15,000. 104

6.15 Mean flame surface density vs. the mean progress variable for $0.4 < x/D < 2$. Reynolds number = 10,000. 104

6.16 Mean flame surface density vs. the mean progress variable for $0.4 < x/D < 2$. Reynolds number = 12,500. 105

6.17 Mean flame surface density vs. the mean progress variable for $0.4 < x/D < 2$. Reynolds number = 15,000. 105

6.18 Flame surface density along the centerline. Reynolds number = 10,000. . 106

6.19 Flame surface density along the centerline. Reynolds number = 12,500. . 106

6.20 Flame surface density along the centerline. Reynolds number = 15,000. . 107

6.21 Global consumption speed versus turbulence fluctuation normalized by the unperturbed laminar flame speed. 108

NOMENCLATURE

Symbol	**Description**
A	burner exit area
$A_{\langle c \rangle}$	flame surface area in $\langle c \rangle$ contour
$B.R.$	blockage ratio
$\langle c \rangle$	mean reaction progress variable
D	burner exit diameter
L	integral length scale
L_p	instantaneous flame front length
m	mass
$\dot{m}$	mass flow rate
p	pressure
Q	volumetric flow rate
$Re = v_{bulk} D / \nu_{unburned}$	Reynolds number
$Re_t = v_{rms} L / \nu_{unburned}$	turbulent Reynolds number
$S_L^0 \quad or \quad S_L$	(unperturbed/unstretched) laminar flame speed
$S_{T,GC}$	turbulent flame global consumption speed
$S_{T,L}$	turbulent flame local consumption speed
t	characteristic time
T	temperature
$v_{bulk} = \frac{Q}{\pi D^2/4}$	bulk velocity
r	radial (span-wise) direction
x	axial (stream-wise) direction
z	azimuthal (out-of-plane) direction
u	radial (span-wise) velocity

v	axial (stream-wise) velocity
w	azimuthal (out-of-plane) velocity
u', v', w'	velocity fluctuation
$\overline{u}, \overline{v}, \overline{w} \quad or \quad \langle u \rangle, \langle v \rangle, \langle w \rangle$	mean velocity
$v_{rms} = \sqrt{\langle u'^2 \rangle}$	rms velocity
$u_{rms}/\langle u \rangle, v_{rms}/\langle v \rangle, w_{rms}/\langle w \rangle$	turbulent intensity
$\dot{w}$	mass rate of production or destruction
Y	mass fraction of a chemical species
δ	flame brush thickness
ρ	density
μ	dynamic viscosity
ν	kinematic viscosity
Σ	flame surface density
τ	shear stress
τ_L	integral time scale

ABSTRACT

Kim, Jupyoung Ph.D., Purdue University, August 2019. Effects of Turbulent Flow Regime on Pilot and Perforated Plate Stabilized Lean Premixed Flames. Major Professor: Jay P. Gore Professor.

An experimental study of the effects of turbulent flow regime on the flame structure is conducted by using perforated-plate-stabilized hydrogen-piloted lean premixed methane/air turbulent flames. The underlying non-reacting turbulent flow field was investigated using two-dimensional three-components particle imaging velocimetry (2D3C-PIV) with and without three perforated plates. The non-reacting flow data allowed a separation of the turbulent flow regime into axial velocity dominated and vortex dominated flows. A plate with 62% blockage ratio was used to represent the stream-dominant flow regime and another with 86% blockage ratio was used to represent the vortex-dominant flow regime. OH laser-induced fluorescence was used to study the effects of the turbulent flow regime on the mean progress variable, flame brush thickness, flame surface density, and global consumption speed. In comparison with the stream-dominant flow, the vortex-dominant flow makes a wider and shorter flame. Also, the vortex-dominant flow has a thicker horizontal flame brush thickness and a thinner longitudinal flame brush thickness. Especially, the horizontal flame brush thickness for the vortex-dominant flow does not follow the turbulence diffusion theory. Then, the vortex-dominant flow shows a relatively constant flame surface density along the stream-wise direction, while the stream-dominant flow shows a decreasing flame surface density. Lastly, the vortex-dominant turbulent flow improves the consumption speed in comparison to the stream-dominant turbulent flow regime with the same velocity fluctuation level.

1. INTRODUCTION

1.1 Combustion and our life

How long can people survive without electricity and transportation? In contemporary life, the energy represented by transportation and electricity is the most important source of human life, as shown in Fig. 1.1-(a). In terms of transportation, internal combustion (IC) engine and gas turbine engine are the dominant engines to operate transportation: airplanes, automobiles, watercraft, and locomotives. Electricity production is also predominantly satisfied by consuming fossil fuels. Even though alternative sources are evolving by utilizing wind and solar energies, energy production, namely electricity generation and power generation for transportation using combustion, has been dominant for many decades. Among fossil fuels, natural gas-fired energy production has been the highest percentage of energy production and will be expected drastic growth in the future, as shown in Fig. 1.1-(b). In addition, combustion is the most high-power density method to generate energy. That is, the combustion process provides a certain amount of energy with the smallest equipment compared with other energy sources.

With the fact that the combustion is significant to our life, pollutant emission regulations for energy-producing devices are getting strict with decreasing the amount of emission rate per device. Thus, research and development of the combustion process have to be done with the purposes of diminishing the impact of combustion on the environment, both by cutting down pollutant emissions and increasing the efficiency of combustion facilities. The traditional combustion process was not able to achieve these two aims. However, turbulent fuel-lean combustion can accomplish both goals.

In combustion, gas turbine engines and IC engines are the two primary devices not only in transportation but also in electricity production. Fig. 1.2 shows (a) a

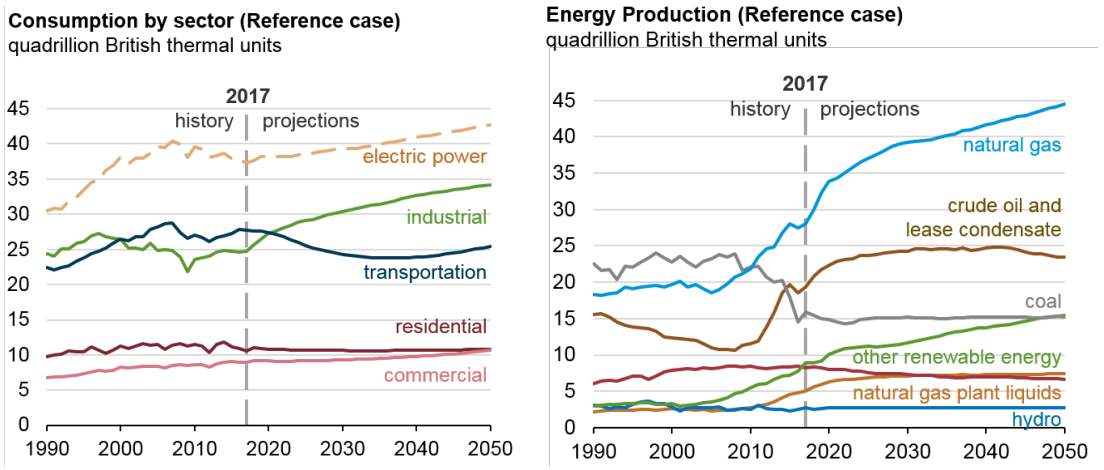

(a) (b)

Fig. 1.1. Annual energy consumption and production. Data distributed by U.S. Energy Information Administration (EIA)

photograph of general electric SGT-300 gas turbine engine from GE website, (b) a schematic of a gas turbine engine, and (c) a schematic of an internal combustion engine.

The author would like to focus on gas turbine engines, especially. Gas turbine engines, including natural-gas-fueled power plants as well as jet engines of airplanes, are complex machines. However, they involve three common sections. The compressor, which pulls air into the engine, pressurizes it and supplies it to the combustor. The speed of intaking air is at hundreds of kilometers per hour. The combustor generally made up of a ring or canisters arrangement of multiple burners. In the manifold of each burner, fuel is injected and mixes with the air from the compressor. The mixture is burned at the combustion chamber at temperatures of more than 1600 $^{\circ}C$ in today's gas turbine engines (H class). The combustion produces a high-temperature high-pressure gas stream that enters and expands through the turbine section. The turbine is a complex array of alternate stationery and rotating blades. As hot combusted gas expands through the turbine, it spins the rotating blades. The turbine

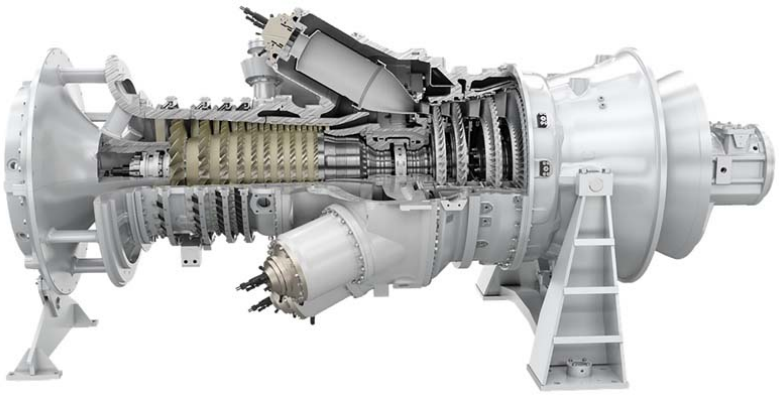

(a) GE SGT-300 gas turbine engine

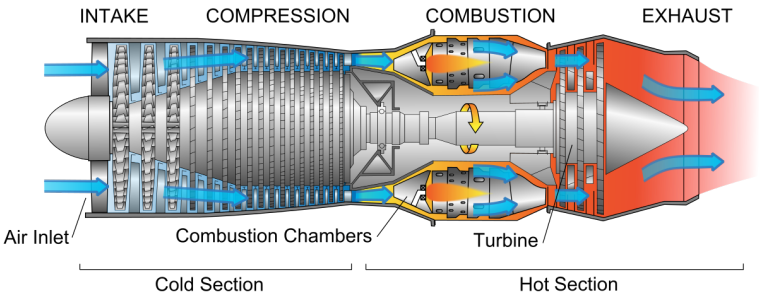

(b) Schematic of a gas turbine

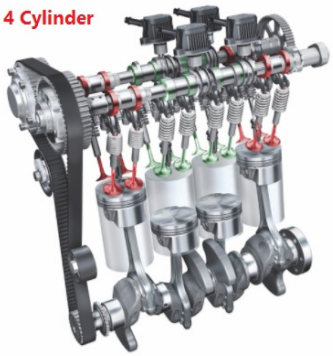

(c) Schematic of internal combustion engine

Fig. 1.2. (a) a photograph of general electric SGT-300 gas turbine engine from GE website, (b) a schematic of a gas turbine engine, and (c) a schematic of internal combustion engine

performs a dual function. It drives the compressor to operate and turns a generator to produce electricity.

Gas turbines can be categorized into two types: (1) aeroderivative engines and (2) heavy frame engines. Aeroderivative engines operate at very high compression ratios (usually more than 30). Aeroderivative engines tend to be very compact and are useful when smaller power productions are demanded. Heavy frame engines are characterized by lower pressure ratios (typically below 20) and tend to be physically large. Because large frame turbines have higher power productions, they produce more massive amounts of emissions and must be designed to achieve low emissions of pollutants. One fundamental feature of a gas turbine engines' fuel-to-power efficiency is the turbine inlet temperature. Higher temperature generally means higher efficiency, which can lead to a more economical operation. H class gas turbine engine has 1600 $^{\circ}C$ turbine inlet temperature providing typically 170 - 230 MW and 1000 MW with a combined-cycle plant. The engines achieve efficiencies as high as 60 percent.

Fig. 1.3 present an example of a combustor of a gas turbine engine, patent US 8,631,656 B2. Figure (1) is a cross-sectional view illustration of a gas turbine engine combustor with an array of fuel burners for operating with a number of circumferential flame temperature nonuniformities. Figure (2) is a schematical illustration of the first array of carburetors in burners to reduce or eliminate acoustics for a 3 per rev frequency in a gas turbine engine combustor with a single annular ring of fuel injectors. Figure (3) is a schematical illustration of the second array of carburetors in burners to reduce or eliminate acoustics for a 3 per rev frequency in a gas turbine engine combustor with two annular rings of fuel injectors. Figure (4) is a schematical illustration of the third array of carburetors in burners to reduce or eliminate acoustics for a 3 per rev frequency in a gas turbine engine combustor with three annular rings of fuel injectors. Figure (5) is a schematical illustration of the fourth array of carburetors in burners to reduce or eliminate acoustics for a 5 per rev frequency in a gas turbine engine combustor with a single annular ring of fuel injectors. Figure

(6) is a schematical illustration of the fifth array of carburetors in burners to reduce or eliminate acoustics for a 5 per rev frequency in a gas turbine engine combustor with two annular rings of fuel injectors. Figure (7) is a schematical illustration of the sixth array of carburetors in burners to reduce or eliminate acoustics for a 5 per rev frequency in a gas turbine engine combustor with three annular rings of fuel injectors.

A diverse concept of combustors has been designed and applied to the gas turbine engines in order to achieve better performance and better fuel efficiency. Currently, as a future map of gas turbine engines and IC engines, new concepts of a combustor are evolving.

One of the concepts includes exhaust-gas recirculation (EGR) or flue-gas recirculation (FGR). Mazas et al. [1] studied that the effects of CO_2 and H_2O addition on premixed oxyfuel combustion with experiments and numerical simulations on the laminar flame speed of $CH_4/O_2/CO_2/H_2O(v)$ and $CH_4/O_2/N_2/H_2O(v)$ mixtures. Kim et al. [2] investigated NO emission characteristics experimentally for the oxy-fuel combustors using FGR technology. They found the optimal inlet arrangement and operating conditions of the FGR oxy-fuel combustor with two separate oxidizer nozzles yields the most stable flames in a wide range of CO_2 ratios. Flame speed at atmospheric and high pressures were numerically and experimentally investigated using the CO_2 diluted outwardly propagating CH_4/O_2/He flames by Chen et al. [3]. Han et al. [4] studied chemical effects including flame surface density and flame burning velocity of CO_2 diluted, piloted, turbulent CH_4/air premixed flames using high-repetition-rate OH PLIF. EGR or FGR are experimentally simulated mostly by CO_2 addition as you have seen because of a difficulty of addition of H_2O into a combustor.

Another concept is lean premixed pre-vaporised (LPP) combustors. Lieuwen et al. [5] provided special writing to combustion society about combustion dynamics of LPP combustor. Dhanuka et al. [6] experimentally investigated the mechanism that causes a periodic combustion oscillation in a LPP combustor. The combustor was run with high flow rates of preheated air at elevated pressures, with Jet-A as the fuel. The injector provided LPP combustion and featured a stable premixed

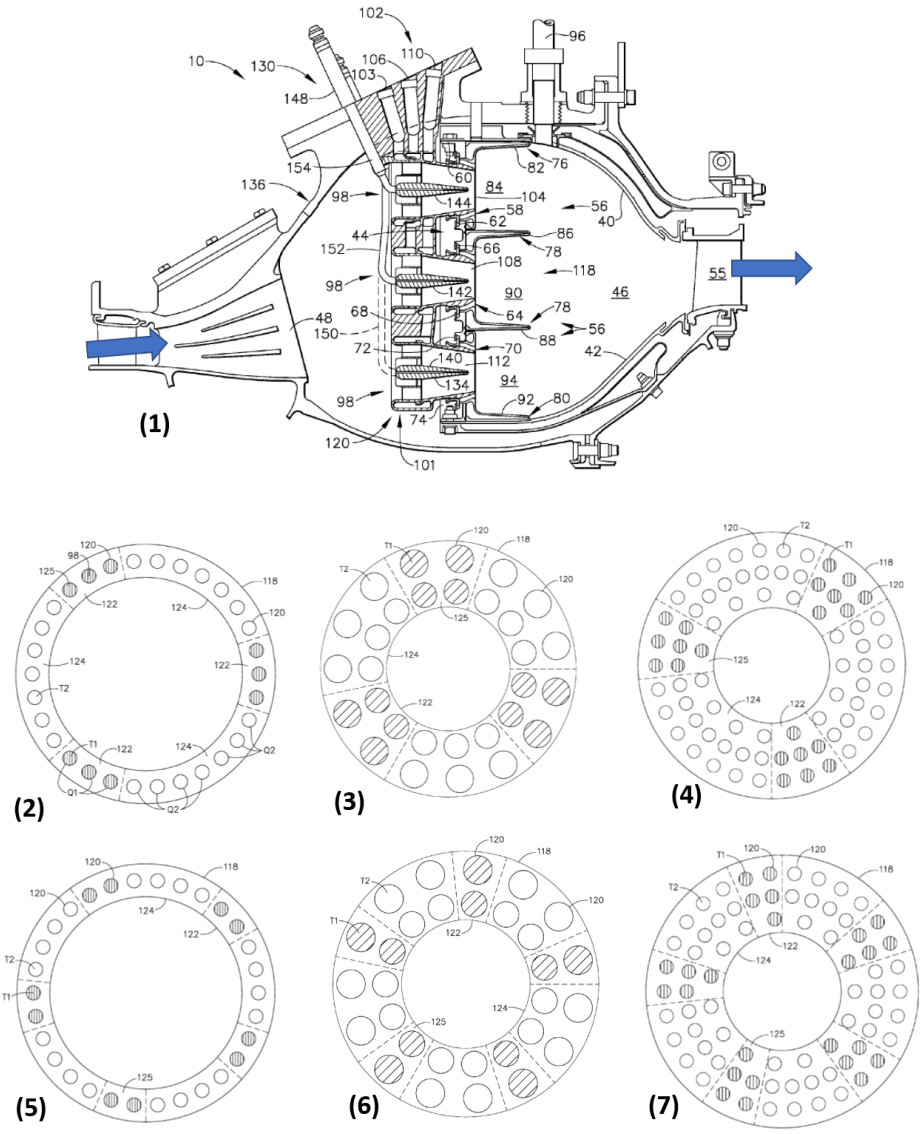

Fig. 1.3. An example of a combustor of a gas turbine engine. Patent US 8,631,656 B2. (1) a cross-sectional view illustration of a gas turbine engine combustor with an array of fuel burners. (2) to (7) is six sequential arrays of injectors of the combustor.

flame surrounded by a pilot flame. The combustor was indentified as stable over a wide range of conditions, but instability associated with unsteady flashback and liftoff of the flame were observed. Temme et al. [7] studied a LPP combustor showing

surpassing features in reducing pollutant emissions. Phase-averaged particle image velocimetry was first applied to a LPP combustor.

The last concept is a combustor through axial staged lean-mixture injection. A staged fuel nozzle with a pilot mixer and the main mixer was developed and tested using a single-sector combustor to control emissions by Yamamoto et al. [8]. The test results showed that the combustor enables an 82% reduction in NO_x emissions relative to the ICAO CAEP/4 standard and a drastic decrease in smoke and CO emissions. Saitoh et al. [9] investigated the emissions characteristics of a gas turbine combustor characterized by the reaction enhancement of the secondary mixtures of lean compositions by the burned gas from the primary stage. Adachi et al. [10] developed a three-stage combustor to prove that lean premixed mixtures supported by the hot burned gas from the upstream stage can be used for obtaining a better trade-off between ultra-low-NOx and high combustion efficiency over a wide range of operation conditions.

1.2 Combustion

Combustion is an exothermic chemical reaction, which means energy generated by a chemical reaction is released into the environment. Deflagration and detonation are two ways energy can be released. If the combustion process propagates at subsonic speeds, it is deflagration. If the combustion process moves at supersonic speeds, it is detonation.

The definition of deflagration is a fire in which a flame travels rapidly, but at subsonic speed, through a gas. That is, a deflagration has the speed of burning lower than the speed of sound in the surroundings. Everyday fire and most controlled combustion are examples of a deflagration. The flame propagation velocity is less than 100 m/s and the over-pressure is less than 0.5 bar. Because it is controllable, a deflagration can be harnessed to do work. Examples of a deflagration include an internal combustion engine, gas stove, fireworks, and gas turbine engine. A deflagration burns

outward radially and requires fuel to spread. Thus, for example, a wildfire starts with a single spark and then expands in a circular pattern if there is fuel available. If there is no fuel, the fire burns out. The speed at which a deflagration moves depends upon the quality of the available fuel.

Detonation means explosion. When a combination of reactions releases a lot of energy in a very short time, the explosion may occur. It is characterized by a supersonic exothermic front above 100 m/s up to 2000 m/s and significant over-pressure up to 20 bars. The front drives a shock wave ahead of it. Although technically a form of oxidation reaction, a detonation doesn't require combination with oxygen. Unstable molecules release considerable energy when they split and recombine into new forms. For Example, chemicals produce detonations include any high explosives, such as TNT (trinitrotoluene), nitroglycerine, dynamite, picric acid, C-4. Detonations, of course, can be used in explosive weapons such as nuclear bombs. In a much more controlled manner, they are also used in mining, road construction, and the destruction of buildings or structures.

In daily life, a deflagration has been utilized more than a detonation. A deflagration is used for power generation or electricity generation in order to maintain billions of lives. Two main applications of the deflagration for the power generation and electricity generation are the IC engine and gas turbine engine in aero and on the ground. In the subsection, these engines will be discussed deeply.

1.3 Premixed flames

A terminology, a flame, is more widely and frequently used than deflagration. Because deflagration is a fundamental component of a flame, a flame is the most appropriate terminology rather than deflagration. That is, a flame consists of tons of deflagration waves propagating in a localized area. Scientists and engineers are focusing on the investigation of a characteristic of the combustion process by observing a flame and related features.

Herein, it may be pertinent to define a flame. A flame is a self-sustaining propagation of a localized combustion zone at subsonic velocities [11]. There are several key words in this definition. First, we require a flame to be confined; that is, the flame occupies only a small portion of the combustible mixture at any one time. The second keyword is subsonic. A discrete combustion wave that travels subsonically in termed a deflagration.

A flame can be sustained by burning a mixture comprising a fuel and an oxidant, for example, methane and oxygen in the air. The burned mixture consists a mixture of water, carbon dioxide, and nitrogen at a high temperature, typically at about 2000 K. Most of cases, the burned mixture includes minor species such as carbon monoxide and nitrogen monoxide. As temperature increases along with a flame, the pressure is assumed constant even though there is a small pressure drop across the flame, from the unburned mixture to the burned mixture. The density drops about six times across the flame.

A flame can be divided into three modes in terms of fuel to air (oxidant) mixing status: non-premixed flame, premixed flame, and partially premixed flame. First, a non-premixed flame is when fuel and air are not mixed at all until the moment of burning. Before fuel and air are burned, the two reactants exist separately. A representative example of a non-premixed flame is a candle flame. Before a wax and a surrounding air are burned and make a flame, the wax and the surrounding air cannot be mixed at all. A premixed flame is, on the other hand, when fuel and air are mixed completely so that the fuel and air mixture is spatially and temporally homogeneous before a flame. Lastly, if fuel and air are mixed but not completely and not homogeneously, it is a partially premixed flame.

1.4 Turbulent premixed flames

A turbulent premixed flame is a premixed flame with a turbulent flow speed defined with Reynolds number and turbulent motion. Steps of physical mechanisms

are: An energy released in the chemical reactions heats the product mixture. A part of this energy is transported to the unburned mixture due to not only heat transport by molecular heat conductivity but also mass transport of the product mixture toward the unburned mixture, increasing the temperature of the unburned gas mixture in the vicinity of the zone where the chemical reaction occurs. The increase in temperature initiates chemical reactions ahead of the zone mentioned above, which moves toward the unburned mixture, and the flame propagates. Therefore, the flame propagation is controlled by molecular transport and chemical reactions.

Conservation equations for reacting flows will be to investigate flames in this study. The physical mechanism during combustion can be understood by exploring mass conservation equation, momentum conservation equation, species balance equation, energy conservation equation, and a few basic equations described in [12] and [13]. Energy conservation equation can be manipulated to enthalpy conservation equation, and then, temperature balance equation.

A turbulent premixed flame can be expressed by the following conservation equations.

Mass conservation equation

$$\frac{\partial \rho}{\partial t} + \frac{\partial}{\partial x_k}\Big(\rho u_k\Big) = 0 \tag{1.1}$$

where t is the time and $x_k = (x_1, x_2, x_3) = (r, x, z)$ and $u_k = (u_1, u_2, u_3) = (u, v, w)$ are the spatial coordinates and the flow velocity vectors, respectively. The summation convention applies for the repeated index k. ρ is density of the mixture.

Momentum conservation equation

$$\frac{\partial}{\partial t}\big(\rho u_i\big) + \frac{\partial}{\partial x_k}\big(\rho u_k u_i\big) = \frac{\partial \tau_{ik}}{\partial x_k} - \frac{\partial p}{\partial x_i} + \rho \sum_{n=1}^{N} \big(Y_n f_{ni}\big) \tag{1.2}$$

where

$$\tau_{ik} = \mu\Big(\frac{\partial u_i}{\partial x_k} + \frac{\partial u_k}{\partial x_i} - \frac{2}{3}\frac{\partial u_j}{\partial x_j}\delta_{ik}\Big) \tag{1.3}$$

is a shear-stress component in ith direction on a surface whose outward normal is in the kth direction. δ_{ik} is the Kronecker delta and μ is the dynamic molecular viscosity of the mixture. The terms on the RHS of equation 1.2 are associated with the viscous force, the pressure force, and the body force. p is pressure and Y_n is the mass fraction of a chemical species n, where $n = 1 \cdots N$ and f_{ni} is a body force per unit volume acting on species n in the direction i. If this body force is due to a gravitational acceleration g, the body force term can be written as $\overline{\rho}_n g$.

Species conservation equation

$$\frac{\partial}{\partial t}\big(\rho Y_n\big) + \frac{\partial}{\partial x_k}\big(\rho u_k Y_n\big) = \frac{\partial}{\partial x_k}\Big(\rho D_n \frac{\partial Y_n}{\partial x_k}\Big) + \dot{w}_n \tag{1.4}$$

where Y_n is the mass fraction of a chemical species n, where $n = 1 \cdots N$. The molecular diffusivity, D_n, is of the nth species in the mixture and the mass rate, $\dot{w}_n$, is of production or destruction of the nth species. The first term on the RHS of equation 1.4, the mass molecular flux of species n in direction k, has been approximated by Fick's law.

Energy conservation equation

The energy conversation equation can be written in many alternative forms [12–15]. One of the equations is,

$$\frac{\partial}{\partial t}\big(\rho h\big) + \frac{\partial}{\partial x_k}\big(\rho u_k h\big) = \frac{\partial p}{\partial t} + \frac{\partial}{\partial x_k}\big(u_k p\big) + \tau_{ik}\frac{\partial u_i}{\partial x_k} - \frac{\partial q_k}{\partial x_k} - \rho\sum_{n=1}^{N} D_n f_{nk}\frac{\partial Y_n}{\partial x_k} + \dot{Q}_{rad} \tag{1.5}$$

where

$$q_k = -\lambda\frac{\partial T}{\partial x_k} - \rho\sum_{n=1}^{N} h_n D_n \frac{\partial Y_n}{\partial x_k} \tag{1.6}$$

is the molecular flux of enthalpy. $\dot{Q}_{rad}$ is the energy exchange per unit volume due to radiation. T is temperature and λ is the thermal conductivity of the mixture. The equation 1.5 and 1.6 can be simplified after a few assumptions:

- It is assumed that the flow Mach number is sufficiently low for compressibility effects to be neglected, allowing the first, second, and third terms on the RHS of equation 1.5 to be set zero.
- Radiative heat transfer is assumed to be negligible.
- Energy transfer due to body forces is assumed to be negligible.
- A mixture is treated as an ideal gas.

With the assumptions, now the energy conservation equation becomes

$$\frac{\partial}{\partial t}(\rho h) + \frac{\partial}{\partial x_k}(\rho u_k h) = \frac{\partial}{\partial x_k}\left[\frac{\mu}{Pr}\frac{\partial h}{\partial x_k} + \mu \sum_{n=1}^{N}\left(\frac{1}{Sc_n} - \frac{1}{Pr}\right)h_n \frac{\partial Y_n}{\partial x_k}\right] \tag{1.7}$$

$Pr = \mu/(\rho a) = \nu/a$ and $Sc_n = \mu/(\rho D_n) = \nu/D_n$ are the Prandtl and Schmidt numbers, respectively. $a = \lambda/(\rho c_p)$ is the molecular heat diffusivity of the mixture. The ratio of $a/D_n = Sc_n/Pr$ is called the Lewis number, and Le_n is for the nth species.

Herein, the energy conservation equation can be more simplified if we apply one more assumption:

- It is assumed that $Sc_n = Pr$ for all species; this requires both that D_n can be approximated by a common value D for all species and that $Sc = Pr$ for all species. This means Lewis number is unity.

Then, the molecular-diffusion term, the second term on the RHS is canceled. The equation 1.7 can be written as

$$\frac{\partial}{\partial t}(\rho h) + \frac{\partial}{\partial x_k}(\rho u_k h) = \frac{\partial}{\partial x_k}\left[\frac{\mu}{Pr}\frac{\partial h}{\partial x_k}\right] \tag{1.8}$$

1.5 Motivation and objectives

As aforementioned in the very first section, new concepts of a combustor are evolving to enhance the performance and efficiency of a combustor. This study will investigate lean premixed flames, especially in turbulent flow conditions associated with high gas velocity in a combustor. In lean premixed turbulent flames as well as any turbulent flames, stabilization of the flames is essential for the efficient performance and the reliable operation of gas turbine engines.

In gas turbine engines, the flowing gas velocities are much faster than the maximum flame speeds. The burning velocity must be identical to the flow velocity for a stationary flame front. The two important factors which determine the rate of movement of the flame front across the combustion chamber are the reaction rate and the transposition rate [16]. Flame stabilization is usually achieved by creating recirculation of some of the combustion products and hence to continuously preheat and ignite the fuel/air mixture. The hot recirculating gases transfer heat to the colder ones ignite those and initiate flame spread. The burned gases convey heat to the recirculation zone to balance the heat lost in igniting the combustible gas. Sufficient energy must be fed to the stabilization region to ignite the coming gas flow continuously.

To stabilize a flame on a burner, a few devices, flame holders, are utilized: (1) bluff body [17–23], (2) swirler [24–29], (3) mesh [17, 18, 30, 31], and (4) perforated plate [17, 18, 31–37]. Generally, the main flame is stabilized using a combination of the flame holders, not using a single flame holder. In the combinations, a perforated plate is the most widely used in the sequence of flame holders to stabilize a flame and control the structure and dynamics of a flame. Though its high usage and importance, the studies about the perforated plate are rarely done. In this study, a perforated plate will be investigated. Particularly, the effects of turbulent flow regime generated by a perforated plate on the flame structure will be discussed.

In the following chapter, chapter 2, there will be a literature review about turbulent premixed flames, perforated plates as turbulence generators, particle image

velocimetry measurements for turbulent flames and flows, and planar laser-induced fluorescence measurements for turbulent premixed flames. Chapter 3 will describe the burner used in this study. Then, chapter 4 will draw flame conditions and flame images. Chapter 5 and 6 are about particle image velocimetry and planar laser-induced fluorescence measurements for the flames. Finally, chapter 7 presents the summary and conclusion of this study.

2. LITERATURE REVIEW

A literature review of four different schemes will be performed. First of all, I will summarize studies about turbulent premixed flames to understand flames from the burner used in this study. Second, turbulence generators will be reviewed to understand what types of turbulence generators are used in combustors and why this study selects a perforated plate as a turbulence generator. Third, researches with particle image velocimetry applied to turbulent flames/flows will be reviewed. Lastly, researches with planar laser-induced fluorescence applied to turbulent flames will be studied.

2.1 Turbulent premixed flames

Since Damköhler reported the effect of turbulence on premixed flames [38], there have been extensive studies about turbulent premixed flames. Not only about comprehensive investigations for turbulent premixed flames, but also about specific characteristics such as flame brush thickness, flame brush density, and consumption speed (burning velocity) for the flames have been documented.

Turbulent flame brush

The turbulent flame brush thickness δ_T is one of the significant aspects of flames. The turbulent flame brush indicates the spatial region over which the instantaneous turbulent flame fronts are located [39]. The instantaneous flame fronts can be measured of the reaction layers of CH (Methylidyne) or OH (hydroxyl) radicals. Note that the flame front has its thickness. Because the flame brush is a time-averaged quantity, the average progress variable distribution through the flame brush can also

be extracted or vice versa. In other words, where the leading edge and trailing edge of the flame brush are the locations of mean progress variables equal to unity and zero. Fig. 2.1 shows a schematics of the turbulent flame front and brush with (a) an instantaneous flame front marked by CH layer [40], (b) superposition of instantaneous flame fronts obtained at different times, and (c) a turbulent flame brush associated with a time-averaged view of the same flame [11].

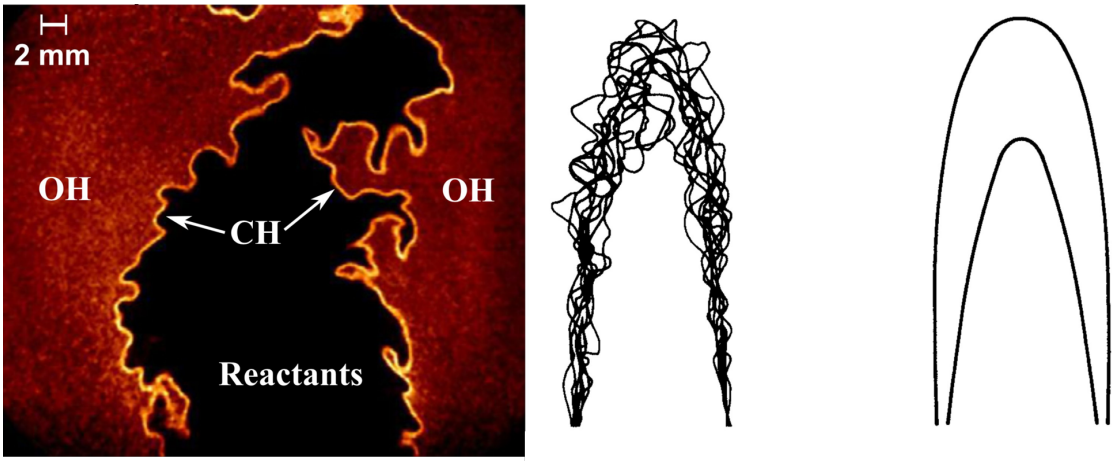

(a) (b) (c)

Fig. 2.1. Schematics of the turbulent flame front and brush. (a) an example of instantaneous flame front marked by CH layer [40], (b) superposition of instantaneous flame fronts obtained at different times, (c) a turbulent flame brush associated with a time-averaged view of the same flame [11].

The turbulent flame brush thickness can be determined in several ways. Gouldin et al. and others [41–45] determined the thickness by finding the distance between two specific mean progress variable surfaces; for instance the horizontal distance between $\langle C \rangle = 0.9$ and $\langle C \rangle = 0.1$. Whereas, Namazian et al. and others [46–52] determined the thickness by the maximum gradient method followed by

$$\frac{1}{\delta_{T,x}} = \max \left| \frac{d \langle C(x, r = 0) \rangle}{dx} \right| \tag{2.1}$$

$$\frac{1}{\delta_{T,r}(x=x^*)} = \max\left|\frac{d\left\langle C(x=x^*,r)\right\rangle}{dr}\right| \tag{2.2}$$

where the mean flame brush thickness along the burner centerline $\delta_{T,x}$ and those along the radial direction $\delta_{T,r}(x=x^*)$ at a specific axial location. x and r are axial and radial coordinates. Herein, the reaction progress variable C is defined as

$$\begin{aligned} C &= \frac{Y_{F,u} - Y_F}{Y_{F,u} - Y_{F,b}} \\ &= \frac{T - T_u}{T_b - T_u} \end{aligned} \tag{2.3}$$

where Y_F is the mass fraction of fuel and T is the gas temperature. Subscripts u and b represent unburned reactants and burned products, respectively. $\langle C\rangle$ is mean progress variable for transient state. The different two methods for the turbulent flame brush thickness present different quantitative values, whereas the qualitative trends remain unaltered [44, 45].

Summerfield et al. [30] proved the difference between a laminar premixed flame and a turbulent premixed flame through chemiluminescence images. The images of the laminar and turbulent premixed flames provided that it is noticeable the thickness of turbulent flame brush is broadened than the thickness of the laminar flame which is roughly constant along the position of flame brush. Karlovitz et al. [53] showed that the increase of δ_T is controlled by the turbulent diffusion. That is, turbulence tends to increase the flame brush thickness. Also, they developed the turbulent diffusion model based on Taylor theory. Karlovitz et al. [53] showed that turbulent diffusion controls the behavior of the flame brush thickness. They related the root mean square displacement of the flame surface to the Taylor [54] length scale. According to Karlovitz, turbulent diffusion broadens the distribution of an assembly but does not produce a net motion. Starting from an arbitrary wavy flame front which is thought to be produced by turbulent fluctuations, the flame front propagates in the normal direction for short time intervals, while the turbulence motion is thought to be absent. Portions of the flame front soon intersect each other, thus producing the characteristic

shape of the instantaneous flame front. Sharp edges appear on the burned-gas side and slightly curved surface elements on the unburned-gas side. Because of their oblique positions, the back portions of the flame move forward with increased velocity. The increased velocity compensates for backward diffusion and causes the entire flame to move forward. Damköhler [38] stated that the fine-scale turbulence increases the transport within the flame brush, whereas the large-scale turbulence does not affect the structure of the instantaneous flame front. He further added that the diffusion caused by the turbulent motion proceeds forward and backward within the flame brush with equal velocity represented by the root-mean-square (rms) velocity.

The turbulent diffusion model by Karlovitz et al. predicted δ_T well with the agreement of the turbulent flame brush measurement [45–47, 51, 55, 56], even though it does not account for the non-homogeneous turbulence or radiation heat release in flames. It was observed that the growth of the turbulent flame brush is linear to the rms displacement of the flame front Y_{rms},

$$\delta_T = \sqrt{2\pi} Y_{rms}, \tag{2.4}$$

with the two approximations which are a Gaussian distribution of displacement of the instantaneous flame front and the thin flame front. The rms displacement of the flame front Y_{rms} can be thought as the thickness of a turbulent mixing layer from an admixture source in a statistically stationary case. The thickness of a turbulent mixing layer can be derived using Taylor theory which is about the turbulent diffusion process masked by the convection of the mixing layer by the mean flow. As a result, the growth of the turbulent flame brush can be described with the equation [48],

$$\delta_T^2 = 4\pi u_{rms}^2 \tau_L t \left\{ 1 - \frac{\tau_L}{t} \left[1 - \exp\Big(- \frac{t}{\tau_L} \Big) \right] \right\} \tag{2.5}$$

where u_{rms} is the rms of velocity fluctuation, τ_L is Lagrangian timescale, and $t = x/\bar{u}$. x is the distance from the flame stabilization area and $\bar{u}$ is mean velocity. It has proven experimentally [4, 48, 49].

Namazian et al. [46] measured the instantaneous flame front positions with the two approximations: a Gaussian distribution of displacement of the instantaneous flame front and the thin flame front. Boukhalfa and Gökalp [47] showed the increase of the turbulent flame brush thickness with the azimuthal distance. Gouldin et al. [55] reported the increase of the turbulent flame brush thickness with the axial distance. Goix et al. [56] showed the important role played by the turbulent length scale at the flame holder, where the burner exit is, in determining the flame behavior. The evolution of the rms displacement of the flame front was shown to be very sensitive to the turbulent intensity at the flame holder: the slope of rms displacement of the flame front versus the downstream distance was found to be proportional to the turbulence intensity. Lee et al. [42] observed the thickness of turbulent flame brush increases as the mean flow velocity increases. Also, the thickness non-dimensionalized by the integral length scale tends to show linear dependence on the H-factor derived from the first moment equation of the reaction progress variable. Griebel et al. [43] showed clearly the thickness of turbulent flame brush from a contour plot of the mean progress variable in Fig. 2.2. Venkateswaran et al. [44] reported several results about the flame

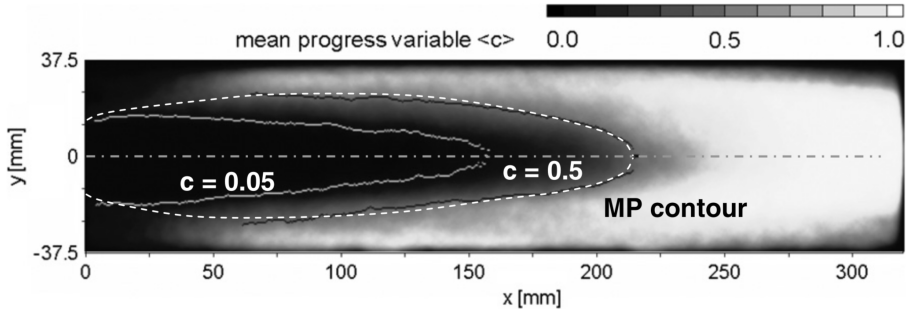

Fig. 2.2. Contour plot of the mean progress variable $\langle C \rangle$ [43]

brush thickness. The thickness is independent of turbulence intensity near the burner exit, where the distance of ($\langle C \rangle = 0.5$) is shorter than 0.5D. However, the thickness is controlled by turbulence from the location where ($\langle C \rangle = 0.5$) is farther than 0.5D, and higher levels of jet turbulence result in a thicker flame brush. D is the burner diame-

ter, 20 mm. Second, the thickness is independent of the fuel composition. Third, the pressure thickens the thickness. Tamadonfar et al. [45, 57] also reported diverse variations of flame brush thickness. The trend of the normalized centerline flame brush thickness is similar to the behavior of normalized characteristic flame height. The normalized horizontal flame brush thickness develops with increasing axial distance from the burner exit and increasing equivalence ratios from 0.7 to 1.0. The normalized horizontal flame brush thickness increases with increasing total turbulence intensity, whereas it decreases with increasing bulk flow velocity under a constant equivalence ratio. The normalized centerline mean flame brush thickness decreases with increasing equivalence ratio from lean to stoichiometric mixtures, whereas it remains relatively constant with increasing equivalence ratio for rich mixtures. The normalized centerline mean flame brush thickness for lean/stoichiometric mixtures is higher than the corresponding value for rich mixtures. Kheirkhah et al. [51, 52] also showed that the enhancement of turbulence intensity increases the flame brush thickness. In addition, they clearly presented a correlation between the flame brush thickness and the rms of the flame front position with a linear relationship, which proposed as the equation 2.4.

Flame brush can be used to characterize other important parameters of flames including flame surface density, consumption speed, and flame front curvature.

Flame surface density

The flame surface density Σ is the flame surface area per unit volume (m^2/m^3) indicating the flame front convolution. A higher flame surface density means more flame fronts exist in the area corresponding to a higher mean reaction rate [15]. Thus, the flame surface density exists within the flame brush. There are three methods to define the flame surface density. The first method is proposed by Shepherd et al. [58–60] which is to overcome a two-dimensional measurement of a three-dimensional flame surface density by a direct measurement of the flame front length and flame zone

area as a function of the mean progress variable. It is obtained using the following expression

$$\Sigma_{2D}(\langle C\rangle) = \frac{1}{n_f}\frac{\sum_{p=1}^{n_f} L_{i,p(\langle C\rangle)}}{A(\langle C\rangle)} \tag{2.6}$$

where n_f is the number of flame images analyzed for each flame condition, and $L_{i,p}(\langle C\rangle)$ is the instantaneous flame front length of a flame realization p with respect to the mean progress variable. It has been evaluated throughout Lachaux et al. [61], Halter et al. [62], Yuen and Gülder [63], Cohé et al. [64], and Zhang et al. [65, 66] for Bunsen-type flames, Shepherd [59] for V-shaped and stagnation-point flames, and Shepherd et al. [67] for low-swirl stabilized flames.

The second method is obtained from the mean flame front length per unit area. Following Filatyev et al. [68], the instantaneous flame front images are divided into interrogation boxes. The instantaneous flame front length for each interrogation box is obtained by multiplying the number of flame front pixels into the resolution of the image. For each interrogation box, the mean value of all these lengths, which is obtained by taking an average, divided by the area of the interrogation box is then equal to the flame surface density of the desired region

The third method to evaluate the flame surface density was developed by Pope [69]. This method is based on the gradient of the progress variable in the flame zone. In addition, Halter et al. [70] improved the equation proposed by Pope [69] for a Bunsen-type burner. The flame surface density can be expressed as

$$\Sigma_{2D}(r,h) = \sqrt{\left\langle \left(\frac{\partial C}{\partial r}\right)^2 + \left(\frac{\partial C}{\partial h}\right)^2 \right\rangle} \tag{2.7}$$

where r and h are the radial and axial directions. The instantaneous flame surface density is evaluated by calculating $\partial C/\partial r$ and $\partial C/\partial h$ for each pixel with the central differencing scheme and determining its norm. The next step is to take an average of all these values for each interrogation box. If the boxes are identical for the second and third methods utilized to evaluate the flame surface density in the space coordinates,

this will help to compare the flame surface density values using both methods at the same physical locations.

Lee et al. [42] claimed that the maximum flame surface density increases as increasing of normalized turbulent fluctuation velocity by laminar flame speed $u^{'}/S_L$ or decreasing of integral length scale. The maximum flame surface density tends to show linear dependence on the K-factor. Also, the peak location of the flame surface density in $\langle C \rangle$ space is correlated in terms of the degree of gradient or counter-gradient diffusion by turbulence. The flame surface density increases at a higher ambient pressure due to decrease in the laminar burning velocity and the length scales of flame wrinkling. Renou et al. [49] The maximum of flame surface density decreases as the flame propagates and remains independent of the Lewis number in the $\langle C \rangle$ space. The results also indicate a decreasing of the maximum flame surface density with $u^{'}/S_L$. The peak location is a little less than the symmetrical value $\langle C \rangle = 0.5$, and increases slightly as the flame propagates. Tamadonfar et al. [57] reported that the maximum flame surface density decreased with increasing equivalence ratio for many different flames. In addition, the maximum flame surface density decreased with increasing total turbulence intensity. The maximum flame surface density for rich mixtures was higher than the corresponding value for lean/stoichiometric mixtures. Filatyev et al. [68] reported that the maximum flame surface density decreases as mean flame brush thickness increases due to turbulent diffusion. They also noticed the changes in the flame surface area flame do play a major role in determining the trends in the burning velocity results. To be specifically, merging of flamelets leads to a decrease in flame surface area and S_T. The geometric factor that causes flame wrinkling is associated with flame height. That is, increasing the turbulence level tends to make the flame propagate faster, but this is counteracted by the fact that a faster Bunsen flame becomes shorter, which reduces the residence time during which stretch is applied.

Consumption speed

The consumption speed of flames S_T is the how rapidly the leading edge of the flame brush will traverse a certain distance [39]. Physically, the consumption speed can be divided into two concepts: global and local consumption speeds.

The global consumption speed provides an evaluation of total reactants consumption rate for the defined flame. It is expressed as

$$S_{T,GC} = \text{Global consumption speed} = \frac{\dot{m}_R}{\rho_R A_{\langle C \rangle}} \tag{2.8}$$

where $\dot{m}_R$ is the mass flow rate of the reactants, ρ_R is the density of the reactants, and $A_{\langle C \rangle}$ is defined as the area of a certain value of the $\langle C \rangle$ contour; for example, $A_{\langle C \rangle = 0.5}$ means the area of the $\langle C \rangle = 0.5$ contour. The global consumption speed $S_{T,GC}$ that is typically measured in Bunsen geometries. It is proportional to the mass flow rate of reactants. To use this definition it is necessary that all of the reactants pass through the flame brush. Bunsen flames meet this requirement. Counterflow and V-flames, on the other hand, are not appropriate because reactants flow not only through the flame brush, but also through the region where there is on flame. To readily understand the equation 2.8, consider a flat turbulent flame that has contours of $\langle C \rangle$ that are flat planes. In the time Δt the entire brush moves forward a distance $S_{T,GC}\Delta$t. The volume of reactants that was traversed by the wave is $S_{T,GC}\Delta \text{t} A_{\langle C \rangle = 0.5}$. The mass of reactants in this volume is $\rho_R S_{T,GC}\Delta \text{t} A_{\langle C \rangle = 0.5}$. Dividing this number by Δt yields the mass per second of reactants traversed by the wave, which then is set equal to the mass per second of reactants exiting the burner $\dot{m}_R$, which leads to the equation 2.8. $S_{T,GC}$ can be determined in the same way from experimental or DNS results.

The local consumption speed is a local fuel consumption rate at an interrogation region with more insights into wrinkled flame surface area. It is defined as following expression

$$S_{T,LC} = \text{Local consumption speed} = S_L^0 I_0 \int_{-\infty}^{\infty} \Sigma \, d\eta \tag{2.9}$$

where η is normal to the flame brush, S_L^0 is unstretched laminar flame speed, and I_0 is the stretch factor. Profiles of flame surface density Σ are measured generally using laser-imaging diagnostics. If we recall that the local consumption speed is defined at an interrogation region, a control volume analysis can be adopted to the interrogation region. The control volume analysis shown in Fig. 2.3 gives a relationship between the area of wrinkled flame surface A_T to the area of unwrinkled flame surface ($A_{\langle C \rangle = 0.5}$ or A_L). The following expression is the relationship [39].

$$A_T = \int_{-\infty}^{\infty} \Sigma \, dV = \int_{-\infty}^{\infty} \Sigma \, (A_L d\eta) \tag{2.10}$$

Then, the equation 2.9 can be simplified with the equation 2.10 into

$$\frac{S_{T,LC}}{S_L^0} = I_0 \frac{A_T}{A_L} \tag{2.11}$$

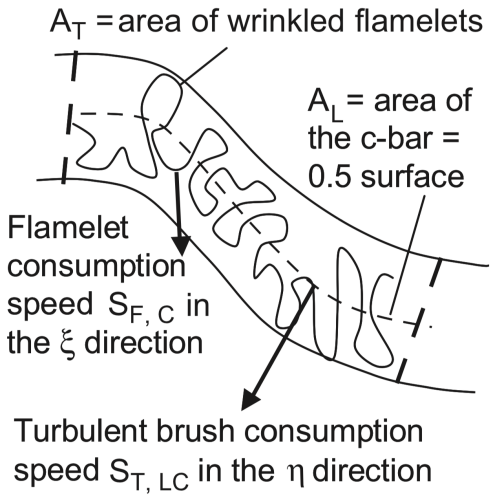

Fig. 2.3. Schematic of the wrinkled area (A_T) and the area of the $\langle C \rangle = 0.5$ contour (A_L). Also, labeled are the flamelet consumption speed ($S_{F,C}$) and the turbulent brush local consumption speed ($S_{T,LC}$). [39]

The other studies developed empirical correlations, as well. For example, Driscoll [39] developed the following correlation,

$$\frac{S_{T,LC}}{S_L^0} = I_0 \Sigma_{max} \delta_T \tag{2.12}$$

based on the empirical correlations [71, 72]

$$\Sigma = 4\Sigma_{max} \langle C \rangle (1 - \langle C \rangle) \tag{2.13}$$

$$\langle C \rangle = \left[1 + \exp\left(\frac{-4(\eta - \eta_m)}{\delta_T} \right) \right]^{-1}. \tag{2.14}$$

The coordinate η is normal to the brush and η_m is the value of η where $\langle C \rangle$ equals 0.5. Schmidt et al. [73] showed the following correlation,

$$\frac{S_{T,LC,\infty}}{S_L^0} = \frac{u_{rms}}{S_L^0} \left(1 + Da^{-2} \right)^{-1/4}. \tag{2.15}$$

They defined $S_{T,LC,\infty}$ is the fully developed turbulent local consumption speed. Kawanabe et al. [74] reported the following correlation,

$$\frac{S_{T,LC}}{S_L^0} = 1 + 1.25 \left(\frac{u_{rms}}{S_L^0} \right)^{0.7}. \tag{2.16}$$

Peters [75, 76] obtained the following correlation,

$$\frac{S_{T,LC,\infty}}{S_L^0} = 1 + \frac{0.39}{2} \frac{L}{\delta_L} \left[\sqrt{1 + 20.5 Da^{-1}} - 1 \right] \tag{2.17}$$

in the planar, one-dimensional case. L is the integral length scale of turbulence and δ_L is laminar flame thickness.

Turbulence effect on consumption speed is also the key concept of turbulent flame. According to Damköhler [38], fine-scale turbulence increases the transport phenomena within the flame front, thereby increasing the burning velocity. The increased burning velocity is an effect of the increased flame surface. The burning velocity would increase almost linearly with the intensity of turbulence. Griebel et al. [43] observed an increase of the turbulence intensity and the integral length scale at the combustor inlet leads to shorter flames i.e. to higher $S_{T,GC}$. Tamadonfar et al. [45] observed

that the leading edge and half-burning surface turbulent burning velocities increase with increasing turbulence intensity, while they decrease with increasing bulk flow velocity. Also, they increase with increasing longitudinal integral length scale. Two correlations to represent the leading edge and half-burning surface turbulent burning velocities were derived with respect to the equivalence ratio, non-dimensional turbulence intensity, non-dimensional bulk flow velocity, and non-dimensional longitudinal integral length scale. Results showed that the half-burning surface turbulent burning velocity decreases with increasing flame height.

Comprehensive parameters such as characteristic flame height, mean volume of the turbulent flame region, mean fuel consumption rate, two-dimensional flame front curvature, local flame front angle, wrinkled flame surface area, mean flamelet consumption velocity, and mean turbulent flame stretch factor were documented in the other researches as well as the researches mentioned in this chapter. Also, their work is well reviewed by authors such as Lipatnikov [12] and Driscoll [39].

2.2 Turbulence generator: perforated plate

Among various flame stabilization methods, the flame stabilization by a perforated plate is the method have frequently been using. Since Videto and Santavicca [77] documented a turbulent flow system using perforated plates, numerous burners utilized perforated plates as one of flame stabilization tools have been studied; recently studied by Chowdhury et al. [18], Skiba et al. [78], Tamadonfar and Gülder [45, 57], and Won et al. [35]. In this section, two topics will be discussed. First, it will be about what is the effects of the perforated plate on flows or flames. Next, it will be reviewed about how perforated plates are utilized in combustion.

The turbulent flows generated by a perforated plate including the details of the plates have been shown by a limited number of studies. Videto and Santavicca [77,79] introduced freely propagating turbulent flows/flames with perforated plates which are two slots in a rectangular duct resulting in 97.5% blockage ratio or 32 holes in a circu-

lar duct resulting in 99.5% blockage ratio. For the latter case, they added a mesh grid to break down the turbulence length scale. They emphasized the importance of perforated plates by describing many disadvantages of the configurations of conventional flame stabilization mechanisms: rod stabilized flame, rim stabilized flame, edge stabilized flame, and wall stabilized (stagnation). Using laser Doppler velocimetry (LDV), they reported (i) The spanwise turbulence intensity increased lightly ahead of the flame and by a factor of five to six across the flame, while the streamwise turbulence intensity was relatively constant ahead of the flame and increased by only two to three times across the flame, (ii) The spanwise, transverse integral length scale increased 100% across the flame, while the streamwise component increased by only 50%, (iii) The degree of autocorrelation of both streamwise and spanwise velocities increased across the flame, resulting in an increased turbulence time scale behind the flame, (iv) The density-weighted kinetic energy doubled across the flame. This increase began well ahead of flame arrival, (v) For the spanwise velocity component, there was an increase of high-frequency fluctuations ahead of the flame and a slight shift in turbulence energy towards lower frequency fluctuations behind the flame. In contrast, the spectral distribution of the streamwise component was relatively unchanged through the flame. Thole et al. [80] used the two-dimensional turbulent flows in a wind tunnel with perforated plates of holes with 5.08 mm in diameter in a lateral spacing S=3D. Castro [81] discovered that the turbulent flow generated by a perforated plate can be divided into two distinct regimes: a stream-dominated turbulent flow regime and a vortex-dominated turbulent flow regime. The stream-dominated turbulent flow regime exists when the blockage ratio (B.R.) is lower than 70%, whereas a B.R. higher than 80% leads to a vortex-dominated turbulent flow regime. He observed the distinct regimes from the drag coefficient, Strouhal number, and vortex zone location versus porosity, as shown in Fig. 2.4. Porosity is 1 - B.R.. He proposed that, between B.R. 80% to 99%, a vortex dominates the wake, although its strength gradually decreases as the vorticity in the shear layers decreases with air entrainment. The reversed flow region and the vortex formation region move downstream as the B.R. decreases. Be-

tween B.R. 70% and 0%, a far wake instability causes the periodic effects and a vortex zone is not seen. The transition between the two flows is over a narrow range of B. R. Several characteristic properties are observed to change under the two distinct flow regimes.

Liu et al. [82] examined the effect of the plate blockage ratios (35%, 50%, and 60%) and the plate hole diameters (25.4, 38.1, and 50.8 mm) through wind tunnel tests using hot-wire anemometry (HWA). They claimed that the normalized turbulence intensity and turbulence integral length scale can be varied independently by using perforated plates with different hole diameters, blockage ratios, and downstream distances. The increase of blockage ratio leads to the increase of turbulence intensity $u_{rms}/\langle u \rangle$. They found a variation of turbulent intensity by Reynolds number, but could not find a correlation. Also, Liu et al. [83, 84] said that the turbulence intensity is higher and more isotropic in the perforated plate with orifice-shaped holes than the perforated plate with straight-shaped holes. Quinn [85] studied that potential core lengths, mean streamwise velocity decays, jet spreading rates, and evolution of the jet. Griebel et al. [43] used perforated plates of 50% and 65% blockage ratios with holes in a hexagonal array to stabilized flames. The plates provided the non-dimensionalized turbulent intensity 5 - 52. Coppola and Gomez [86] investigated not only the effect of perforated plates of a range between 95.5% and 99.65% blockage ratio but also the effect of the geometric parameter of holes in the plates. Using HWA to measure mean streamwise velocity, turbulence intensity, and turbulence length scales, they concluded that the plates with circular holes generate higher turbulent levels at a given flow rate and preserve radial uniformity. From the work done by Nicolleau et al. [87], it is clear that a perforated plate with holes in a hexagonal array gives advantages as shown in Fig. 2.5: (i) the least pressure drop than any other geometries of hole, and maintains constant pressure along streamwise direction, (ii) the perforated plate with holes in a hexagonal array gives the uniform radial profile of streamwise velocity, but the other plates with fractal holes or fractal arrays of holes do not, and (iii) the perforated plate with holes in a hexagonal array generates the peak turbulence intensity near

①

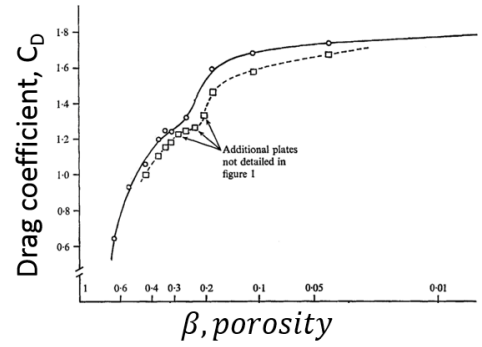

②

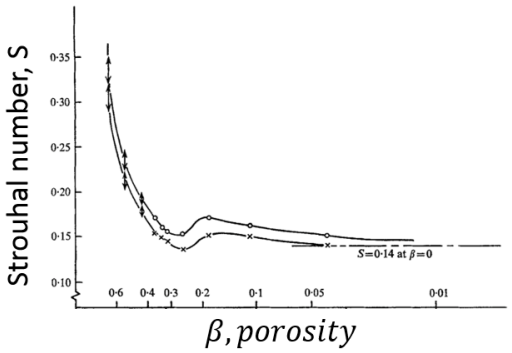

③

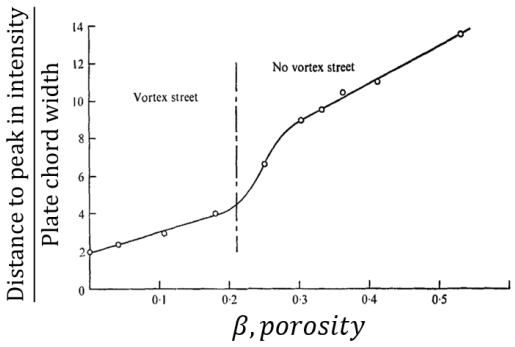

Fig. 2.4. ① Drag coefficient, ② Strouhal number, and ③ vortex zone location versus porosity [81]. Porosity = 1 - B.R.. Castro [81] discovered that the turbulent flow generated by a perforated plate can be divided into two distinct regimes.

the plate, but the other plates with fractal holes or fractal arrays of holes generates the peak turbulence intensity further than the case of perforated plate.

Marshall et al. [88] reported characteristics of flow field by the perforated plates with the movable holes arranged in a hexagonal array. They confirmed uniformity of mean streamwise velocity and rms velocity fluctuation as well as the increase of turbulence intensity by increasing blockage ratio from 69% to 93%. They also argued that the longitudinal length scale is sensitive to blockage ratio, but has no correlation.

Based on the work reviewed in the previous paragraph, many researches about combustion have been used perforated plates to generate turbulence and to stabilize flames [18, 23, 25, 31, 35, 36, 40, 45, 51, 52, 57, 65, 78, 89–105]. A perforated plate with the holes arranged in a hexagonal array is the classical and general shape of plate to stabilize flames, so that most of researches used the configuration of the perforated plate Won et al. [35, 89] and Windon et al. studied two-dimensional turbulent flames with perforate plates of 78% and 50% blockage ratios. Kheirkhah et al. [31, 51, 52] equipped a plate with blockage ratio of 58%, and establish V-flame with a rod. Sundaram et al. [90] installed three perforated plates of blockage ratio 46%, 57%, and 67% in series on their burner. Tamadonfar and Gülder [45, 57] Chowdhury et al. [18] used multiple turbulence generators for turbulence including bluff body, mesh, impinging jet, perforated plate (blockage ratio 60%, 67%, and 78%). They achieved turbulence intensities of 4%, 14%, 24%, and 30%. Skiba et al. [78, 91], Wabel et al. [92], and Marshall et al. [25, 93, 94, 99] adopted the design of perforated plates by Marshall et al. [88].

The studies including the details of flow field and flames documented mean velocity, rms velocity fluctuatoin, and corresponding length and time scales using HWA, LDV, or PIV. However, their spatial resolutions were too big to analyze velocity profiles and velocity decays in an appropriate scale. Furthermore, specific analysis with high spatial resolution measurement was not achieved. In addition, no work about flame has been done for the comparison of blockage ratios less than 70% and higher than 80%. A range of blockage ratio of perforated plates between 70% and

①

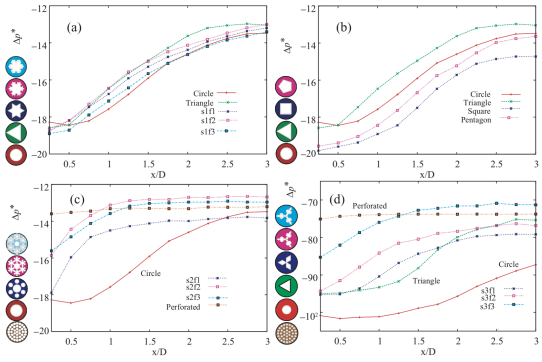

②

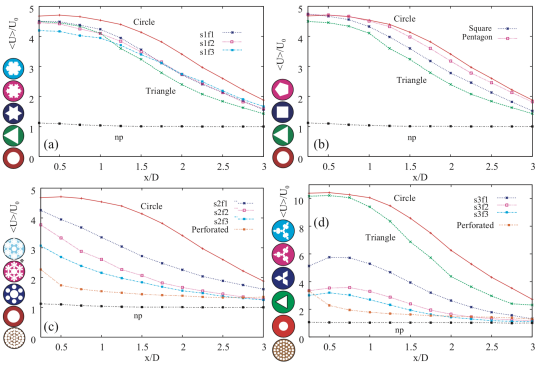

③

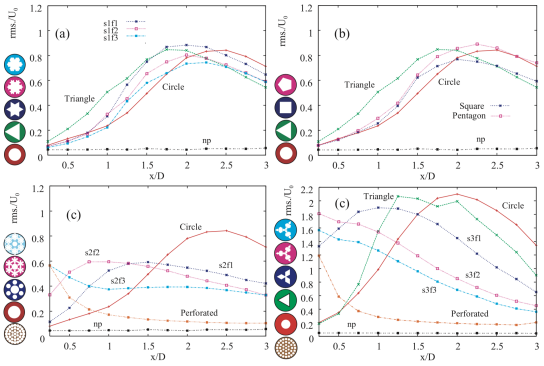

Fig. 2.5. ① The normalized pressure drop, ② the normalized centerline velocity by inlet velocity, and ③ turbulence intensity as a function of downstream locations generated by different geometries of turbulence generator plate [87]. (a), (b), (c), and (d) represent sets of turbulence generator plates showing as figures on the left side of each graph.

80% is the threshold which distinguishes flow characteristics [81, 106, 107]. Thus, it is required what is the effect of those blockage ratios on flow characteristics and then flames [81, 106, 107].

2.3 Particle image velocimetry

Particle image velocimetry (PIV) is the latest and the most widely used technique for the measurement of the flow field as proven in Fig. 2.6. It shows that PIV has emerged to the dominant approach in experimental fluid mechanics since the last three decades. This technique provides instantaneous velocity fields over global domains. The techniques can be classified into 2D PIV and 3D PIV. The 3D PIV techniques can again be divided into two categories: 3D PIV techniques that measure in a three-dimensional domain (3D3C) and 3D PIV techniques that measure in a two-dimensional domain (2D3C). The first category includes the tomographic PIV (TPIV) [108] and holographic PIV [109] techniques. The stereoscopic PIV (SPIV) [110] and dual-plane correlation PIV [111] techniques belong to the second category. The 3D3C PIV techniques give complete three-dimensional velocity data in a 3D measurement volume. However, they need an elaborate and costly experimental equipment and long computation times but have low accuracy in comparison to the 2D and 2D3C PIV techniques. These factors significantly narrow the practical utilization of the 3D3C PIV measurement techniques.

The principle of PIV is well explained in the books by Raffel et al. [113] and Adrian et al. [114]. Most applications of PIV are described in the book by stanislas et al. [115] and schroeder et al. [116]. The typical experimental setup of a PIV system requires four basic components (Fig. 2.7):

- An optically transparent test-section containing the flow/flame with seeded tracer particles
- A light source (pulsed laser) to illuminate the region of interest and light sheet optics to deliver the light to the test-section

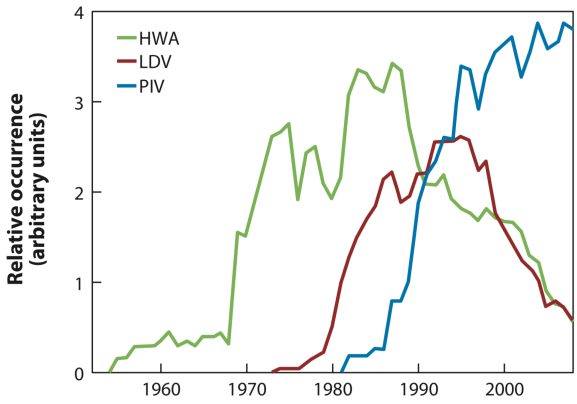

Fig. 2.6. The occurrence of the trigrams hot wire anemometry (HWA), laser Doppler velocimetry (LDV), and particle image velocimetry (PIV) in Google Books (http://books.google.com) between 1952 and 2008. The graph taken from [112] and the data taken from Google Ngrams.

- Recording hardware: a CCD/CMOS camera and a computer
- A computer with a suitable software to process the recorded images and extract the velocity vectors.

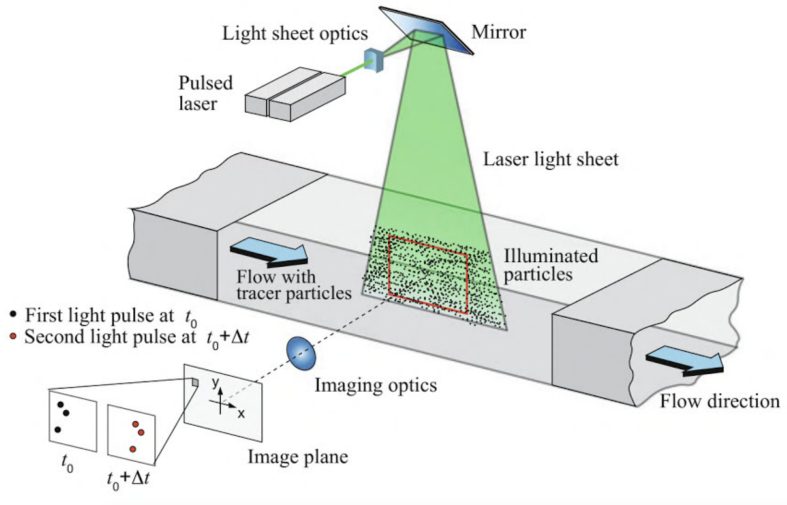

Fig. 2.7. Experimental arrangement for 2D PIV [113]

Using the experimental setup, the typical procedure of PIV technique consists of [113]

- **Seeding**: The tracer particles have to be seeded to the flow.
- **Illumination**: These tracer particles have to be illuminated in a plane or volume of the flow at least twice within a short and known time interval.
- **Recording**: The light scattered from the tracer particles has to be recorded either on two separate frames or on a sequence of frames of a camera.
- **Calibration**: A calibration obtains the relation between the particle image displacement in the image plane and the tracer particle image in the flow.
- **Evaluation**: The displacement of the particle in the particle images between the light pulses has to be determined through evaluation of the PIV recordings.
- **Post-Processing**: To detect and removed invalid measurements and to extract complex flow quantities of interest, complicated post-processing is required.

The general stereoscopic PIV technique employs two CCD/CMOS cameras addition to the experimental setup of a 2D PIV system, with each camera simultaneously capturing the same instantaneous particle configuration from a different angle [110] as shown in Fig. 2.8. The current trend of stereoscopic PIV have been to use digital cameras to record the two views in the angular displacement configuration while incorporating the Scheimpflug condition [110].

The geometric relationship between the real particle displacements (Δx, Δy, and Δz), and the apparent displacements measured by the first camera (ΔX_1,ΔY_1), and the second camera (ΔX_2,ΔY_2) are presented below.

$$\Delta z = \frac{-d_o \left(\Delta X_1 - \Delta X_2\right)}{M_n S - \left(\Delta X_1 - \Delta X_2\right)} \tag{2.18}$$

$$\Delta x = \frac{\Delta X_1 \left(x - S/2\right) - \Delta X_2 \left(x + S/2\right)}{M_n S - \left(\Delta X_1 - \Delta X_2\right)} \tag{2.19}$$

$$\Delta y = -\frac{y\Delta z}{d_o} + \frac{\Delta Y_1 + \Delta Y_2}{2M_n}\left[\frac{\Delta z}{d_o} - 1\right] \tag{2.20}$$

where $M_n = d_i/d_o$. d_o is the object distance to the middle of the light sheet, and d_i is the corresponding image distance. For the Scheimpflug system, M_n can be calculated from $tan\alpha/tan\theta$. S is the distance between the two cameras.

The measuring volume is confined by the thickness of the laser light sheet. Two cameras at different angles capture each particle images associated with the laser sheet. The particle displacements in the image planes captured by each camera are calculated to 3D velocity fields. More calibration procedure addition to The typical procedure of PIV technique is required to reconstruct the two particle images at different angles related with a flow in a real world. There are two methods to construct the images. First method developed by Willert [117] is by reconstructing the two particle images at different angles and then extracting flow quantities. The other method developed by Soloff et al. [118] is by extracting flow quantities from each particle images and then reconstructing the extracted flow quantities.

Extensive developments on PIV algorithm have been done to increase the accuracy of PIV such as cross-correlation [119–125], window offset [126, 127], multi-grid and multi-frame [127, 128], window deformation [129], outlier [130, 131], and uncertainty analysis [132–135].

Eckstein et al. [119] showed improvement in vector detection and accuracy using Gaussian transformed phase correlation (GTPC) compared to standard Fourier-based cross-correlation (SCC) techniques. They [121] advanced GTPC to robust phase correlation (RPC) with the use of median image filtering. They [120] presented a capability of RPC by providing a reliable digital particle image velocimetry estimate that substantially improves the measurement accuracy and resolution by attenuating Fourier-based error image edge effects. A window offset is another way to decrease the noise of PIV. Westerweel et al. [126] showed the use of a window offset that is equal to the integer part of the displacement in pixel units reduces the noise level of the measurement. Scarano et al. [127] performed improvement in accuracy for quantita-

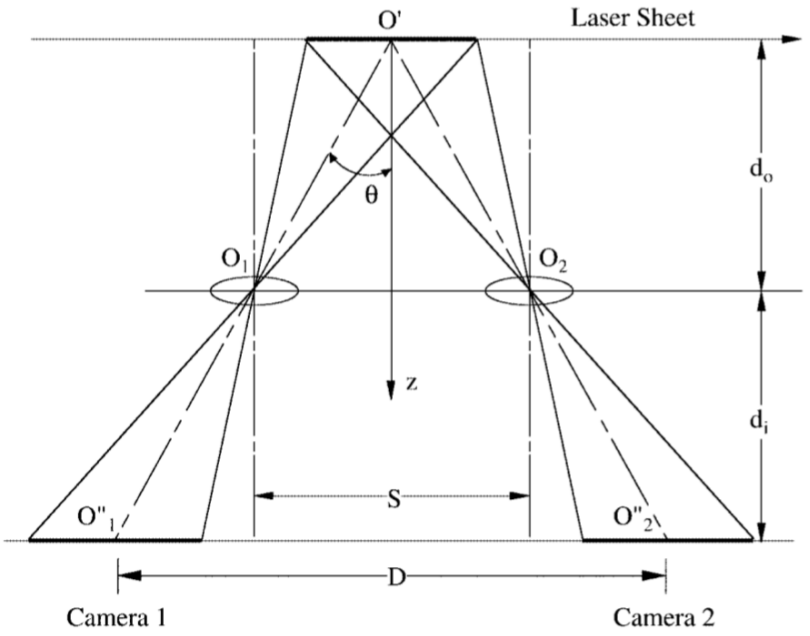

(a) Translation system

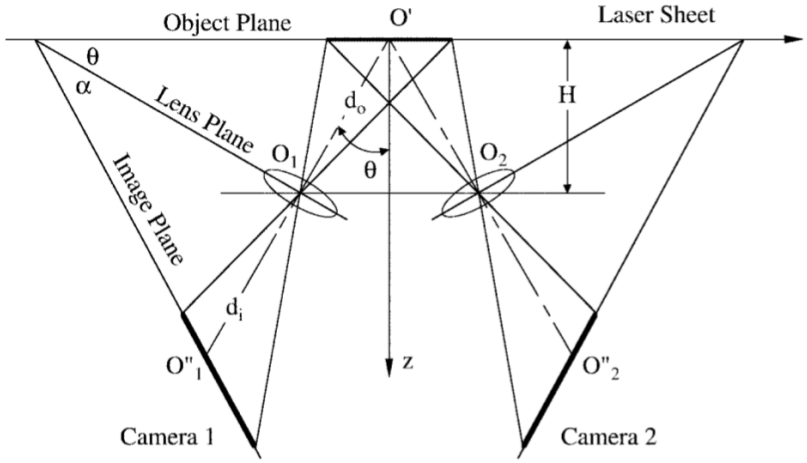

(b) Angular displacement system

Fig. 2.8. Two basic configurations for stereoscopic PIV systems: (a) translation method and (b) angular-displacement method [110]

tive turbulence measurements using a window offset. They also showed that iterative multi-grid approach allows a more precise displacement prediction. Sciacchitano et al. [128] adapted an adaptive multi-frame technique providing a higher signal-to-noise ratio and a more accurate velocity estimation. Scarano et al. [129] showed that a win-

dow deformation gives the significantly improved accuracy and robustness of vector estimation in the presence of highly sheared flows.

In order to quantify accuracy of vector estimation, outlier and uncertainty analysis can be implemented. Westerweel et al. [131] demonstrated that the outlier detection called the normalized median test yields universal probability density function for the residual and that a single threshold value can be applied to effectively detect spurious vectors. The percentage of the outlier, which reveals how many spurious vectors exist in a vector filed, can give a PIV user to select the optimum combination of PIV algorithms. The uncertainty can be analyzed in a few methods. The first method [113] is by mapping the effects of selected primary error sources such as shear, displacement, seeding density, and particle diameter to the true error for a given measurement. The second method is particle image matching [136]. The uncertainty of measured displacement is calculated from the ensemble of disparity vectors, which are due to incomplete match between particle pairs within the interrogation window. This method accounts for random and systematic sources of error; however peak-locking errors and truncation errors cannot be detected. Also, the disparity can be calculated only for particles that are paired within the interrogation window. The last method is using signal-to-noise within the cross-correlation plane [135, 137]. The ratio of primary-peak to secondary-peak in the cross-correlation plane gives the measurement uncertainty.

Stereoscopic particle image velocimetry is used in many applications. Hof et al. [138] and Kapakli et al. [139] used the technique to observe turbulent pipe flows. ElHassan et al. [140] measured turbulent jet flows using the technique. Herpin et al. [141] measured a turbulent boundary layer. Tanahashi et al. [142] developed dual-plane stereoscopic particle image velocimetry. Stereoscopic particle image velocimetry is also adapted to measure premixed turbulent flames by many researcher: Boxx et al. [143], Weinkauff et al. [144], Trunk et al. [145], Steinberg et al. [146, 147], and Petersson et al. [148].

2.4 Planar laser-induced fluorescence

PLIF stands for planar laser induced fluorescence. PLIF has been used to measure species concentration, temperature, pressure, and velocity [149, 150]. Details of PLIF can be found in Kychakoff et al [151] and a schematic of a PLIF experiment is shown in Fig. 2.9.

Hydroxyl (OH) and methylidyne (CH) are two representative species to reveal a flame structure. Hydroxyl radical is generally abundant in flames from the reaction zone to products, and has a peak near the flame front. Furthermore,excitation wavelengths, $\lambda_{ex} \approx 280315$ nm for the $A^2\Sigma^+ - X^2\Pi$ $\left(v^{'} = 0, v^{"} = 0\right)$ and $\left(v^{'} = 1, v^{"} = 0\right)$ bands, are conveniently generated with Nd:YAG-pumped dye lasers using efficient, long-lived red dyes. OH has thus been used as a flame front marker, though with some ambiguity in complex flow fields [152]. Methylidyne exists in low concentrations so that it is difficult to detect and susceptible to fluorescence [152]. However, its primary advantage over hydroxyl is that its distribution within a flame corresponds reasonably well to the region for peak heat release rate [153]. Initially, it was employed of the $A^2\Delta - X^2\Pi \left(v^{'} = 0, v^{"} = 0\right)$ band near 431 nm for excitation. Next, it was demonstrated of $B^2\Sigma^- - X^2\Pi \left(v^{'} = 0, v^{"} = 0\right)$ band near 390 nm for excitation. Recently, $C^2\Sigma^+ - X^2\Pi \left(v^{'} = 0, v^{"} = 0\right)$ band near 314 nm for excitation has shown to detect CH. The C-X band has advantages: (1) the fluorescence yield is not significantly affected by pressures, (2) large emission coefficient, and (3) the coincidence of OH and CH bands enables simultaneous OH and CH measurement [154] and/or easy tuning between OH and CH.

The fluorescence phenomenon using energy level diagram is shown in Fig. 2.10. The left image shows the vibrational and electronic energy levels of an absorbing molecule. An electron in the lower energy level (ground energy level) absorbs a photon specified by a wavelength of laser. Then, it is excited to an upper (excited) energy level. There is a spontaneous emission to a certain energy level. If this electron

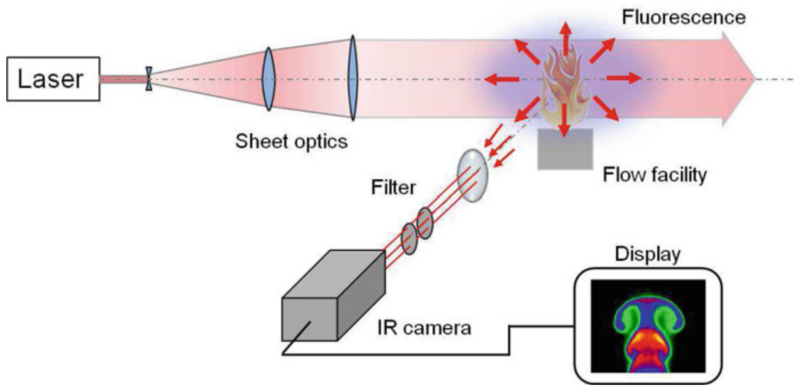

Fig. 2.9. Experimental arrangement for planar laser-induced fluorescence [155]

gives out a photon during the process of releasing energy, then that photon is seen as a fluorescence signal.

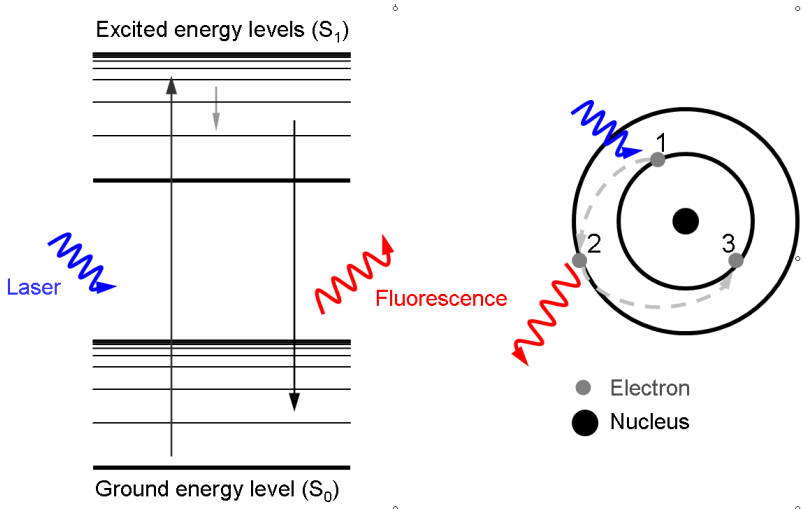

Fig. 2.10. Fluorescence phenomenon using energy level diagram from English Wikipedia

Simultaneous OH/CH PLIF, which has the signal excitation at 314.415 nm and fluorescence at 320 nm (in the CH C-X band and the OH A-X band), has been done by Skiba et al. [78] with LDV measurement. Simultaneous OH PILF/CH_2O PLIF has been done by Marshall et al. [93, 94], Pfadler et al. [156], Skiba et al. [91] with

LDV measurement, Chowdhury et al. [18] with PIV measurement, Won et al. [35] with HWA measurement.The simultaneous OH PILF/CH_2O PLIF has OH signal excitation at near 283 nm and fluorescence at 310 nm and CH_2O signal excitation at 355nm and fluorescence at between near 370 and 530 nm.

The fluorescence signal is given by

$$N_{photon} = n_1^0 W_{12} \left(\frac{A_{v'v"}}{Q_{quench} + A_{v'v"}} \right) \forall_c \left(\frac{\Omega_c}{4\pi} \right) \eta_c \Delta t_L \tag{2.21}$$

where N_{photon} is the number of photons collected per CCD array pixel, n_1^0 is the number density of OH molecules in the ground state, W_{12} is the stimulated emission rate coefficient, and $A_{v'v"}$ is the fluorescence transition rate coefficient. $\forall_c$ is the volume from which LIF signal is collected, Ω_c is the solid angle subtended by collection lens, η_c is the transmission efficiency of optical collection system, and Δt_L is the pulsing time of the laser. n_1^0, Q_{quench}, and W_{12} are the variables changing in the interrogation image. n_1^0 and Q_{quench} are temperature dependent. Also, W_{12} is influenced by collisional and Doppler broadening as well as laser intensity collected per CCD array pixel as $W_{12} = \frac{A_{21} I_L \lambda_{21}^3}{8\pi\hbar c} g_v(\omega)$. A_{21} is the spontaneous emission rate coefficient, I_L is the laser intensity per CCD array pixel, λ_{21} is the wavelength of the laser, $\hbar$ is normalized Planck's constant, c is the speed of light, and $g_v(\omega)$ is the Voigt profile by collisional and doppler broadenings.

3. PREMIXED AXISYMMETRIC REACTOR ASSISTED TURBULENT BURENR

A premixed axisymmetric reactor assisted turbulent burner is developed to investigate characteristics of stabilized turbulent premixed flames sustained by a pilot flame. A turbulent premixed flame in this burner cannot be sustained without a pilot flame. The burner can be operated at both atmospheric and high-pressure conditions up to 20 bars. The burner is also called as PARAT burner by way of abbreviation of premixed axisymmetric reactor assisted turbulent.

3.1 Burner design

A cross-sectional schematic diagram of the burner [157] is shown in Fig. 3.1. The burner is 523 mm long and consists of four components: a fuel/air injection component (red part in the figure), a diverging duct (yellow part in the figure), a converging duct (purple part in the figure), and an outlet (green part in the figure). The gray part in the figure is the casing of the burner. The fuel/air injection component is 178 mm long, the diverging duct is 168 mm long, the converging duct is 147 mm long, and the outlet is 30 mm long. The duct diameter varies from 18 mm to 27 mm along the longitudinal direction of the burner.

The outlet has a main exit and an annular exit. The main exit has an 18 mm diameter (D), and the annular exit has a 28 mm outer diameter and 24 mm inner diameter. Premixed fuel/air stream flows out through the main exit. Pilot fuel flows into separately embedded feeding lines and is ejected through the annular exit. The path of the pilot fuel stream is depicted in the figure.

Air enters the inlet of the air/fuel injection component. Then, fuel is injected from the side of the fuel/air injection component through the fuel inlet. Fuel-air mixing

occurs as it passes through the different mixing stages along the burner. The first stage is a bluff body (gray disk in the middle of the injection component in Fig. 3.1). The second stage includes the diverging and converging ducts. The third stage is the base perforated plate located between the diverging and converging ducts. The fourth stage is the main perforated plate located between the converging duct and the outlet. Hence, the premixed fuel and air mixture is achieved at the outlet. The premixed condition can be identified using acetone planar laser-induced fluorescence, described in the next section.

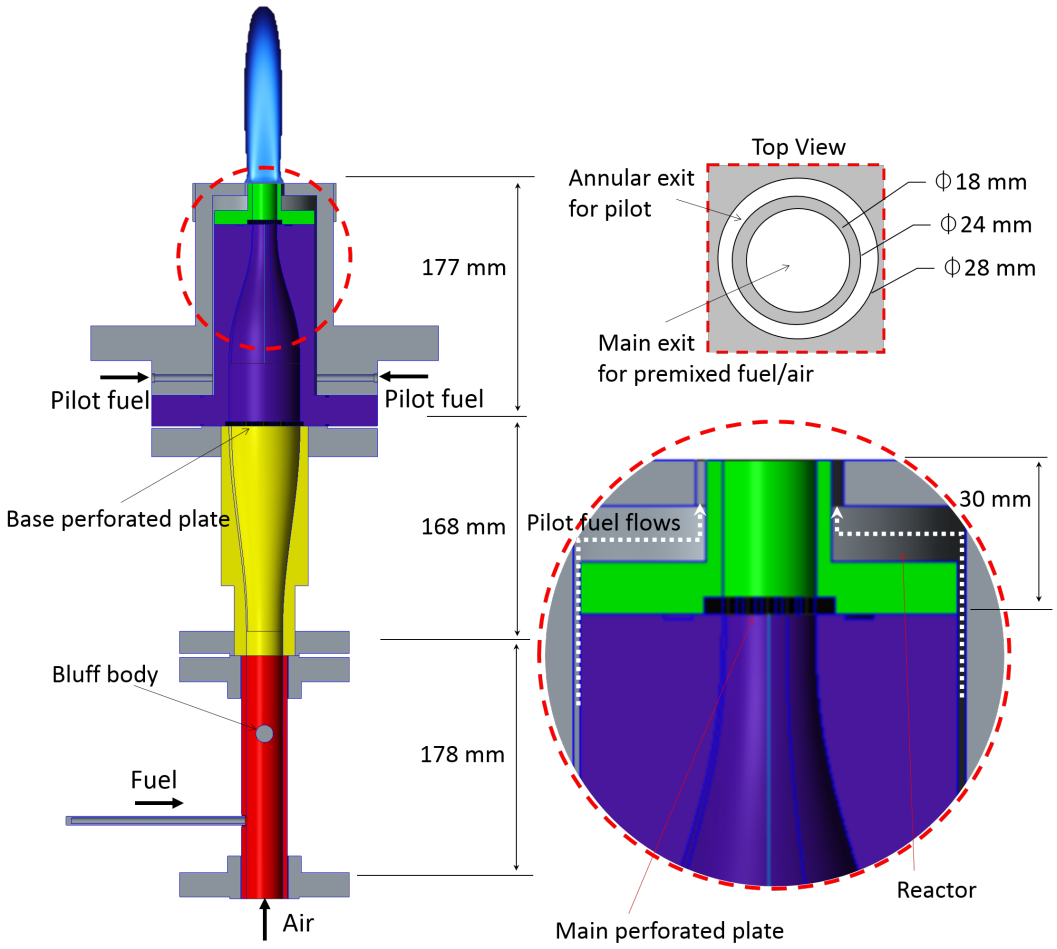

Fig. 3.1. Cross-sectional schematic of PARAT burner.

In terms of turbulence, the bluff body and the two turbulence generator plates have an important role in this burner. Not only high turbulent Reynolds number but also the turbulence intensity can be increased with utilization of a bluff body and turbulence generator plates. The initiation of turbulence is from the bluff body. Furthermore, the diverging and converging components have a function to make fully developed turbulent flow providing thinner boundary layer by preventing flow separation and recirculation zones near the duct wall. This geometry of the duct with enough length provides uniform integral scale as well as uniform mean and fluctuating velocities along the cross section of the duct. At the end of the diverging component, the enhanced turbulent eddies are created by the turbulence generator plate of blockage ratio 90 percent. The eddies are broken down into smaller scales throughout the converging component [158]. Thus, before the second turbulence generator plate located at the end of converging duct component, the scale of turbulent eddies is already approached to fine scale. In addition to these steps, the second turbulence generator plate augments integral scale and turbulent eddies. The purpose of the combination of these four devices is to achieve uniform and high turbulent Reynolds number including high turbulence level.

Photographs of the hardware of PARAT burner is shown in Figure 3.2 as the sideview (left) and the topview. There is a support leg to hold the burner on the ground in the photographs.

3.2 Specification of turbulence generator plates

Based on literature review, the geometry of the most effective and widely used turbulence generator plate is circular perforated plate with hexagonal hole arrangement. This is applied to this study as well. A photograph of turbulence generator plates is shown in Fig. 3.3. The greatest disk is the base turbulence generator plate where is at between converging and diverging duct components. The two other disks are the main turbulence generator plates. The upper disk has 86 percent blockage ratio, and

Fig. 3.2. Photographs of PARAT burner. (Left: sideview of PARAT burner. Right: topview of PARAT burner)

the lower disk has 62 percent blockage ratio. The blockage ratios are determined from the threshold, the blockage ratio between 70 and 80 percent: one is smaller than the threshold and the other is greater than the threshold.

Depending on blockage ratio, Castro demonstrated experimentally that two distinguishable flow regimes exist. In the low blockage ratio, more bleed air is allowed to pass through a turbulence generator plate resulting in the re-circulation region moving further downstream although its strength gradually decreases as the eddies in the shear layer decrease with the introduction of bleed air. In the high blockage ratio, in the other hand, the re-circulation region is only located near field of a turbulence

generator plate [81]. In addition to this study, Othman suggests the range between 70 and 80 percent is in this range, where makes the bleed air is not allowing the flow to come around to create the re-circulating region. Some geometry alter this range such as decreasing the bar thickness ratio of the turbulence plate or moving lower blockage region close to the duct center and therefore produce large velocities in the central region of the duct [107].

One of the two main disks can be installed at between converging duct and exit components. The configuration of holes for all disks are based on hexagonal arrangement as shown in Figure 3.4.

3.3 Degree of mixing of PARAT burner

To prove the reactant from PARAT burner is 100 percent premixed before the burner exit, acetone planar laser induced fluorescence (acetone PLIF) is performed [159]. The experimental setup of acetone PLIF will be described in the following

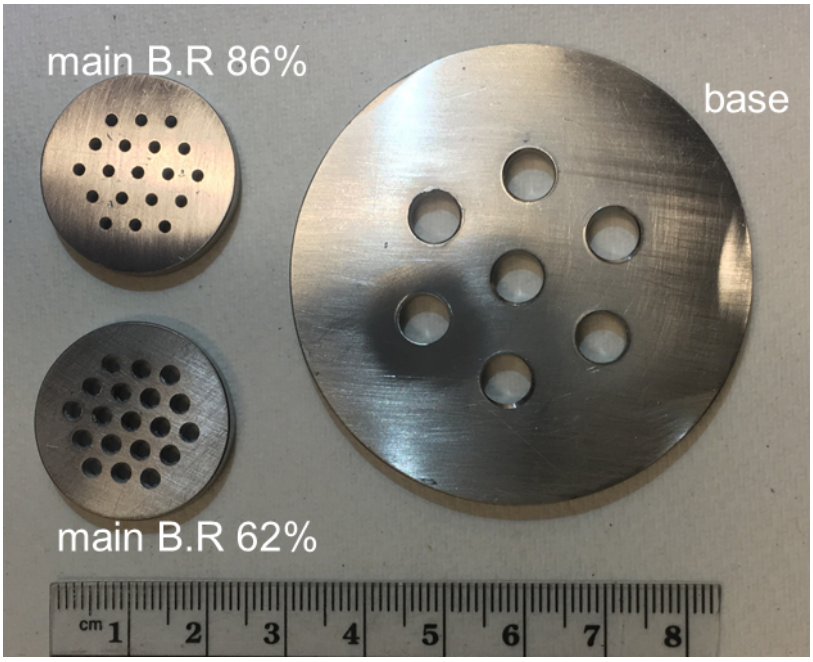

Fig. 3.3. A photograph of turbulence generator plates.

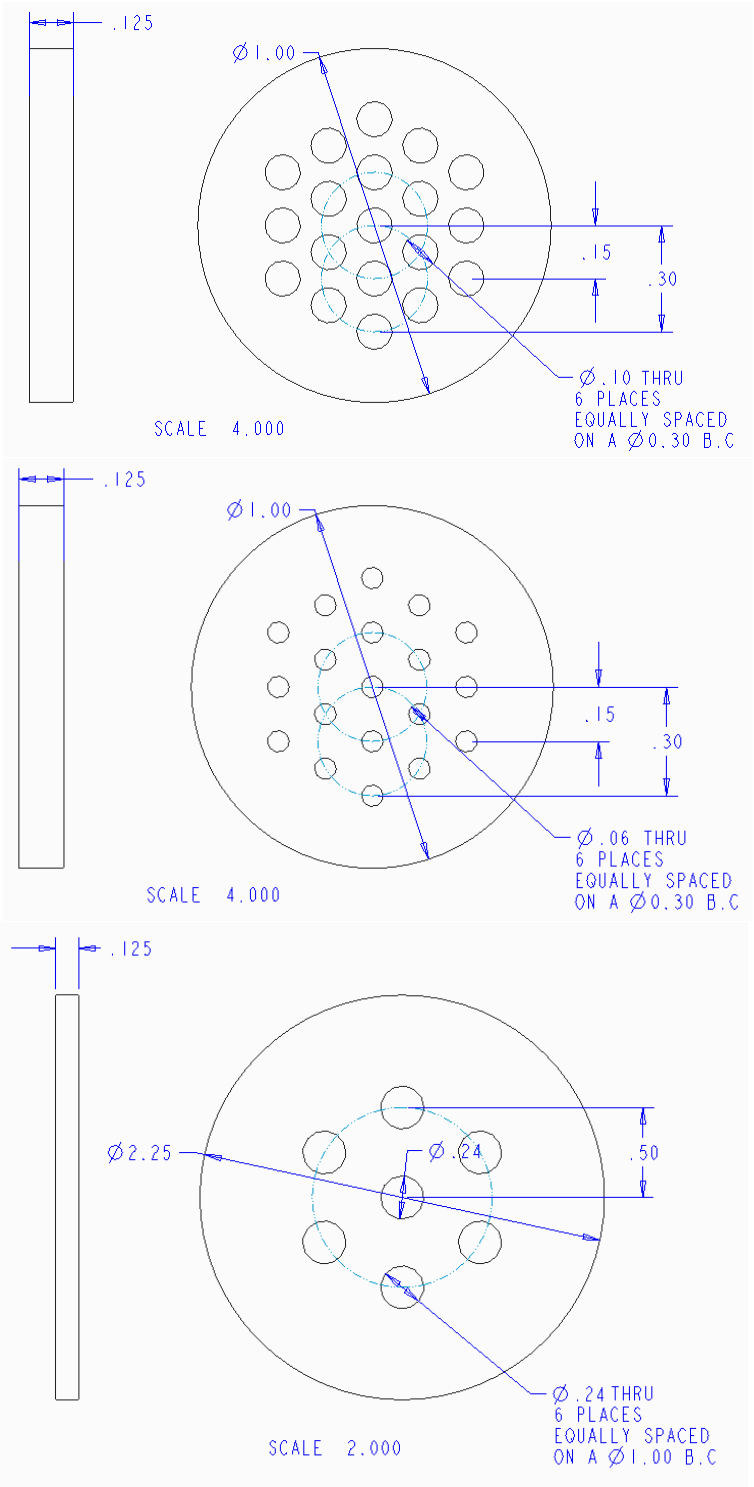

Fig. 3.4. CAD diagram of the turbulence generator plates. Scale in inch. From top to bottom, 62 and 86 percent main turbulence generator plates and 90 percent base turbulence generator plate.

subsection 3.3.1. Figure 3.5 shows the image of acetone PLIF of the flow at the exit of PARAT burner. Qualitatively, the image shows the status of mixing is uniform. In Figure 3.6, but also, the graph shows a constant acetone intensity along the radial direction extracted from the figure 3.3.1. Acetone is a marker of how much mixing is proceeded. If the intensity of acetone is inhomogeneous and having numbers of spots, the fuel and air inserted at the first stage of the burner are not premixed. However, if the fuel and air are mixed well and exist in the constant percentage of mole fractions or volume/mass fractions in any given sample, the intensity of acetone is shown as Fig. 3.6.The degree of mixing is consistent with the figure 3.5 and the graph 3.6 in different Reynolds numbers this study explored: from 10,000 to 25,000.

Decreasing of the intensity of fluorescence from acetone at the boundary of the flow shown in the graph 3.6 is because of mixing between the main stream from the burner and the surrounding air. In the region where there is the surrounding air only, the intensity of fluorescence from acetone becomes zero. Because Fig. 3.5 is without any background removal, it can be readily interpreted that there is definitely no signal if there is no acetone.

Found on the mixing level, PARAT burner is defined as a premixed burner. This results in a flame from PARAT burner is a premixed flame. Among the characteristics of premixed axisymmetric reactor assisted turbulent (PARAT) burner, the first term is attached as the reason mentioned above. The next term, axisymmetric, is because the burner is designed and fabricated as a duct shape is circular. The reason why the term, reactor assisted, is added is because a pilot flame initiated from a reactor assists to sustain a main flame. The last term, turbulent, is hinge on turbulent flames this study will examine.

3.3.1 Experimental setup of acetone PLIF

Methane as a fuel side is mixed with acetone vapor and inserted to the fuel inlet. Air is injected to the air inlet. To capture the acetone concentration in a mixture, it is

Fig. 3.5. An image of acetone planar laser induced fluorescence. The flow consisting fuel, air, and acetone emits fluorescence showing uniform premixed condition generated from PARAT burner.

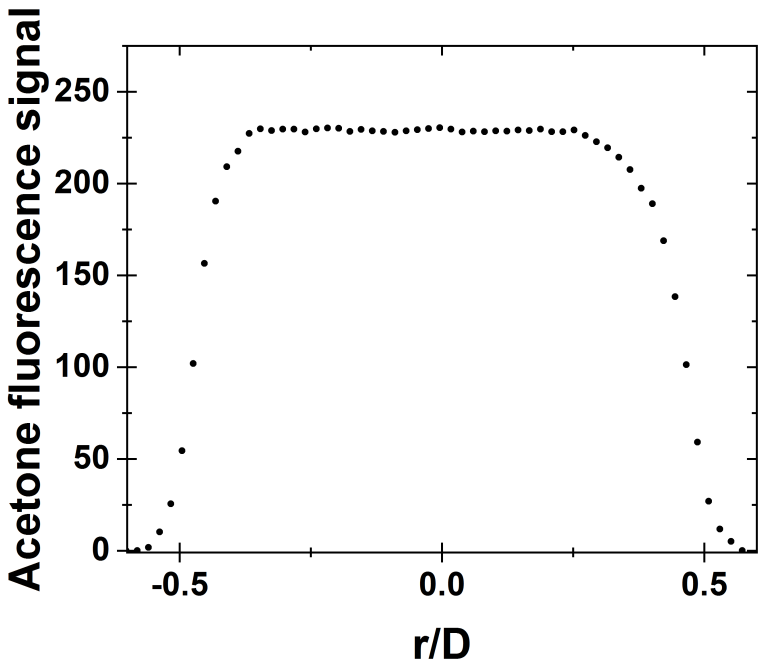

Fig. 3.6. A radial profile of acetone intensity at the exit of the burner. It shows uniform premixed condition generated from PARAT burner.

used of the system consisting of a double-pulsed, frequency-quadrupled, Q-switched Nd:YAG laser (Spectra-Physics Quanta-Ray GCR200 PIV400-10), an optical system, and a high-speed CCD camera (PIVCAM 10-30, TSI Inc., 1000x1016 pixels) with a camera lenses (Tamron AF 28-300 mm F3.5 lenses). The fundamental wavelength of the laser is 1064 nm. The laser operates at 266 nm after the fourth harmonic crystal and emits 150 mJ per pulse at 10Hz, with a pulse duration of 9 ns. Images of fluorescence from acetone excited by 266 nm were collected through the high-speed CCD camera. A blue colored glass filter was used to filter out 266 nm and admit only acetone signal. A laser-pulse synchronizer (Model: 610034, TSI Inc.) was used to synchronize the laser and the CCD cameras

3.4 Capabilities for high temperature and high pressure testing

The PARAT burner was established on a quartz-windowed combustor for a high-pressure test. Plumbing and instrumentation diagram (P&ID) is shown in Figure 3.7. The high-pressure air system in Zucrow laboratories supplied the compressed air for oxidant for combustion, film cooling surrounding inner wall of the combustor, and pressurizing of the gap of quartz windows of the combustor. An electric heater also heated the air. The pipes were insulated by wrapped tape. The primary fuel system injected natural gas for fuel at the main exit, and the secondary fuel system injected the hydrogen for a pilot flame. Water circulation system cooled the combustor shell to prevent overheating. Another water supplied at a downstream of the test facility to cool the exhaust gases for quenching NOx and protecting the gaskets of the back-pressure control valve. The entire system was remotely operated using the LabVIEW system shown in Figure 3.8.

The flame operating condition is shown in Table 3.1. The inlet air was heated to 587 K. THe back-pressure of combustor was increased to 0.52 MPa by flowing the heated air at 0.16 kg/s (0.045 kg/s from burner injector and 0.12 kg/s from film cooling) before the ignition test. Air inlet velocity was about 60 m/s, which is selected

to be far away from the laminar flame speed of 0.4 m/s at standard conditions (0.1 MPa bar, 300 K). An ignition laser was set to 300 mJ per pulse at 10Hz. The hydrogen flow rate was 0.091 g/s. Image sequence of ignition test is shown in Figure 3.9. After the ignition of the hydrogen pilot flame, the CH_4/air flame was established as shown in Figure 3.10.

Table 3.1.
Operating condition of PARAT burner at high pressure and temperature

Re #	100,000
Equivalence ratio	0.8
H_2 flow rate	4.9 g/min
Inlet mixture temperature	587 K
Combustor pressure	0.53 MPa
Film cooling flow rate	7.3 kg/min K

3.5 Capabilities for atmospheric pressure testing

Capabilities for atmospheric pressure testing are proven in the next chapter. The next chapter will show flame conditions and images under atmospheric pressure, which this study focuses on.

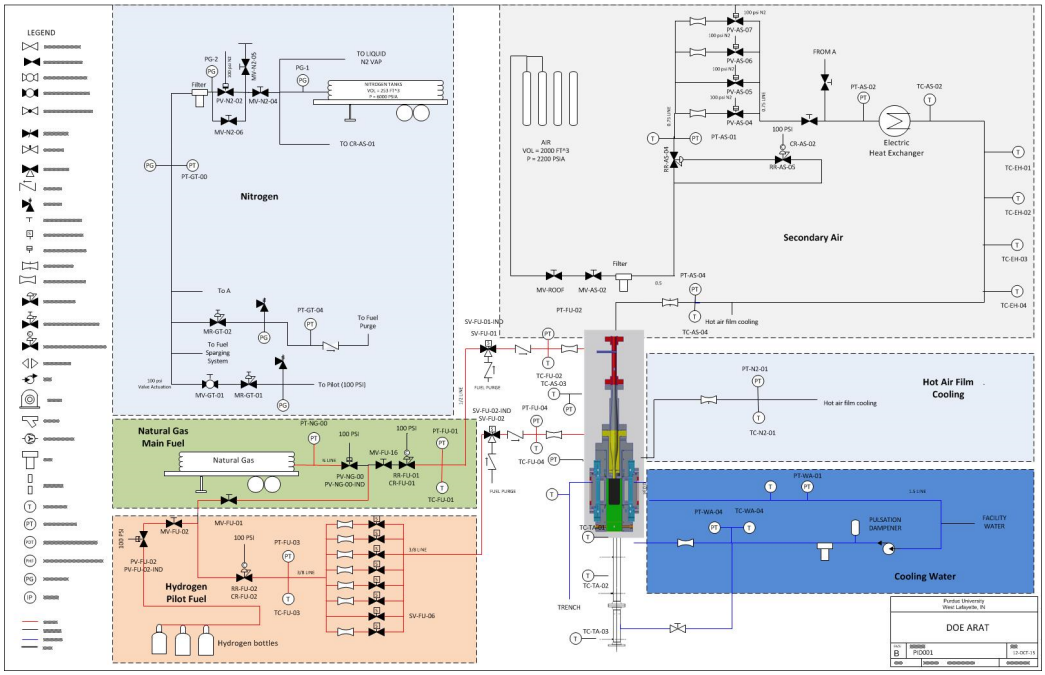

Fig. 3.7. Plumbing and Instrumental Diagram (P&ID) of the experimental arrangement of high-pressure and high-temperature tests

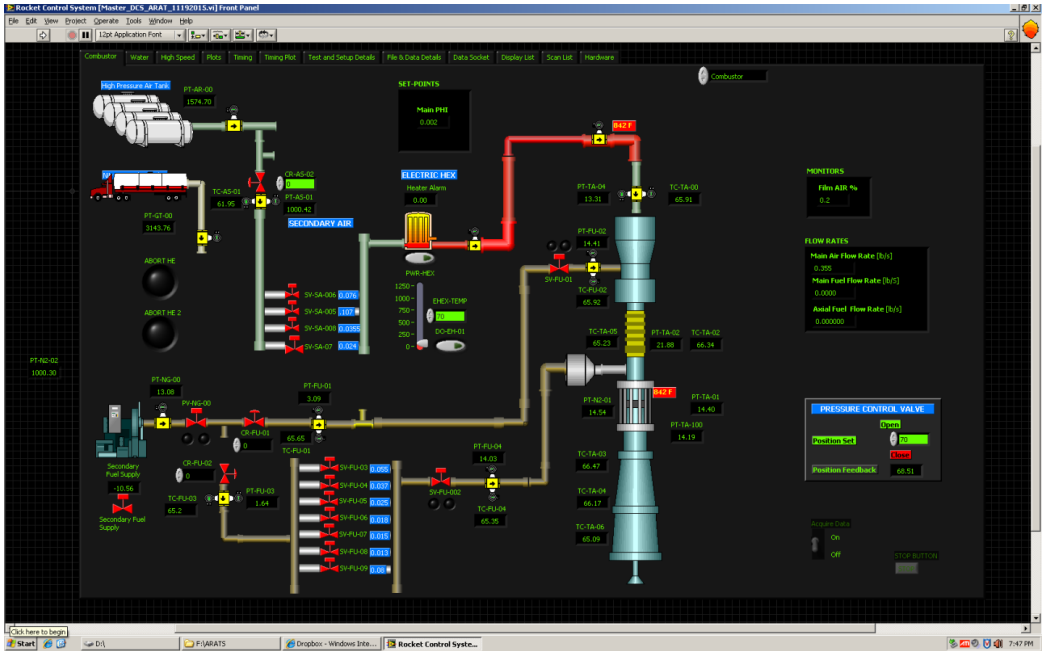

Fig. 3.8. The control panel of LabVIEW of the high-pressure and high-temperature tests using

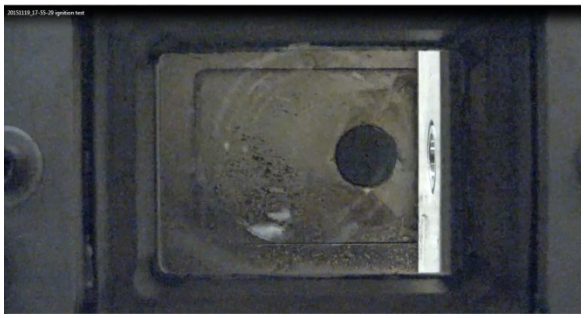

Before ignition

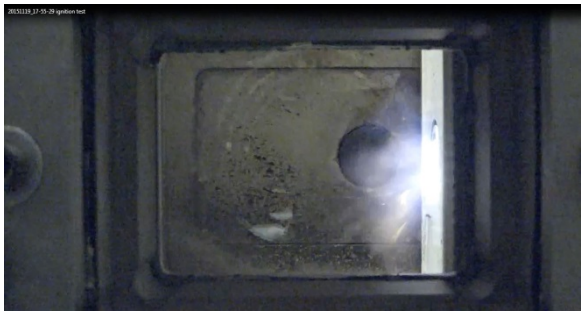

Ignition

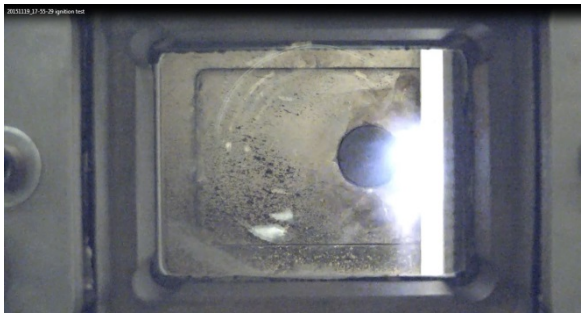

2 minutes after ignition

Fig. 3.9. Image sequence of hydrogen pilot ignition of the PARAT burner under high-pressure and high-temperature condition.

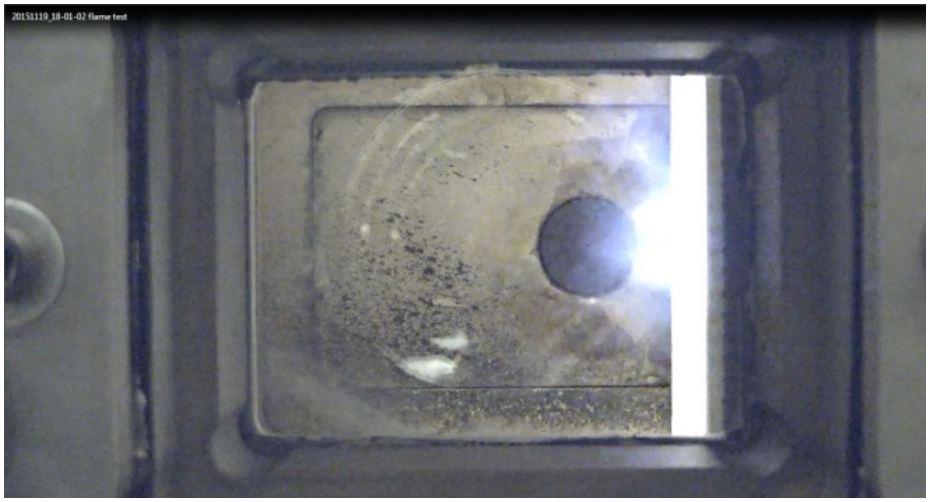

Hydrogen pilot flame

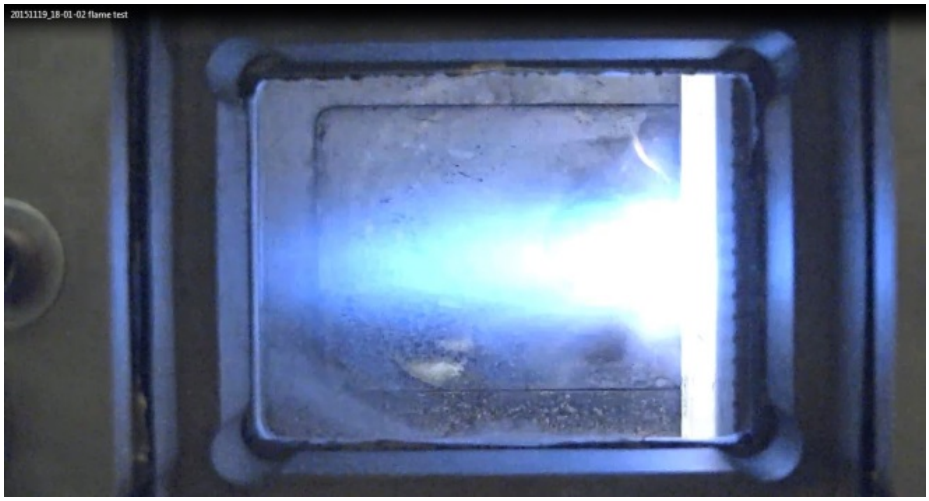

Main flame with Hydrogen pilot flame

Fig. 3.10. Image sequence of natural gas turbulent premixed flame of the PARAT burner under high-pressure and high-temperature condition.

4. OPERATING CONDITIONS AND FLAME IMAGES

This chapter provides operating conditions of experiments under atmospheric pressure and corresponding flame images.

4.1 Operating Conditions

A rule across the conditions is fuel lean and turbulence in order to investigate flame characteristics can be utilized in a combustor of gas turbine engine following high performance and low NOx. First of all, this study will see the difference between reacting and non-reacting flows. Secondly, it will be examined the difference between 62 % and 86% blockage ratios. Lastly, it will be shown how flames change as Reynolds number increases. The flame conditions described above is attached in Table 4.1. The table shows different Reynolds numbers following by the constant equivalence ratio and pilot hydrogen mass flow rate. For the two different blockage ratio, 62 % and 86 %, this operating conditions are repeated. Not only flames, presented also as reacting flows, but also non-reacting flows are examined for all conditions. Thus, total 24 cases are studied.

Flames conditions are calculated using engineering equation solver (EES). The properties of gases are based on gas mixture at NTP, 25 °C and 1 atm. Density of methane is 0.6483 kg/m^3, density of air is 1.169 kg/m^3, and density of hydrogen is 0.08128 kg/m^3.

The uncertainty shown in the table includes uncertainties of a flow calibrator and a flow meter.

Table 4.1.
Operating condition of PARAT burner at atmospheric pressure

Flame #	1	2	3	4	5	6
Equivalence ratio	0.8					
Re # (± 1 %)	10,000	12,500	15,000	17,500	20,000	22,500
Bulk velocity (± 0.05 m/s)	8.5	10.6	12.7	14.9	17.0	19.1
CH_4 flow rate (mg/s ± 1 %)	111	138	166	194	221	249
Air flow rate (mg/s ± 1 %)	2,381	2,975	3,571	4,166	4,762	5,356
Pilot H_2 flow rate (mg/s ± 1 %)	2.71					

4.2 Flame Images

Flames are visualized by a camera, Panasonic Lumix DMC-LX100 with 13 megapixel and 60 fps. Figure 4.1 and 4.2 show ensemble averaged flame images for 12 seconds. A focus and an exposure are identical for the images. A white scale bar indicates a height of an inner boundary of a potential core, which presents a border line of reactant gases and intermediate product gases. It can be also interpreted as a start line of reaction zone at the center of the flame along the streamwise direction. The reaction zone in an ensemble averaged flame image exists until the flame tip. This flame tip is shown as a yellow scale bar. The procedure of image processing to determine a flame tip and a a boundary of a potential core is depicted in Figure 4.5. In order to capture a flame tip, a raw image is split into red, green, and blue (RGB) regimes (step 1 in the figure). The gradient filter is applied to the RGB images, and then, it is applied a threshold filter, which is 1 or minimum value, to the images (step 2 in the figure). This will gives where is a flame tip. There are two method to capture a boundary of a potential core. The first method is through applying a threshold filter to RGB images (step 3-1 in the figure). The second method is by using hue, sensitivity, and brightness (HSB) color threshold filter (step 3-2 in the figure). Both methods give the same result. To set the threshold for the step 3-1 and step 3-2, the set value is determined when a structure of a potential core in the image is attached with the burner surface.

Figure 4.1 and 4.2 show flame images with 62 % blockage ratio (B.R). As increases Reynolds number, a height of flame tip increases until there is extinction. Simultaneously, a potential core grows and its height is 1/5 of a height of flame tip, as measured. In the same trend, Figure 4.3 and 4.4 show flame images with 86 % B.R. The height of flame tip as well as the height of potential core are shorter than the case of 62 % B.R. This is because high B.R turbulence generator makes high turbulence level resulting in higher re-circulation degree. This will be proven in the experiment section quantitatively. In terms of flame extinction, the 86 % B.R reaches earlier than the 62

%. This is because too much powerful turbulence extinguishes a flame by suppressing chemical reaction in the certain flow time and reaction time, represented as Damkhler number. That is, even if the mean velocity is identical, high turbulence leads to high instantaneous velocity, which results in the instantaneous velocity exceeds the limit of chemical reaction time of a flame. This causes extinction of a flame.

The growth of a flame tip is increases linearly, and a potential core is growing exponentially. By far, when a rate of increase of a potential core reaches a certain value, a flame is extinguished. This will also be investigated.

The estimation of height of potential core is validated using coherent anti-Stokes scattering (CARS) in Figure 4.6. The determination of a potential core through flame (a), (b), and (c) is well matched with the height of (d) which is temperature profile measured by coherent anti-Stokes scattering (CARS).

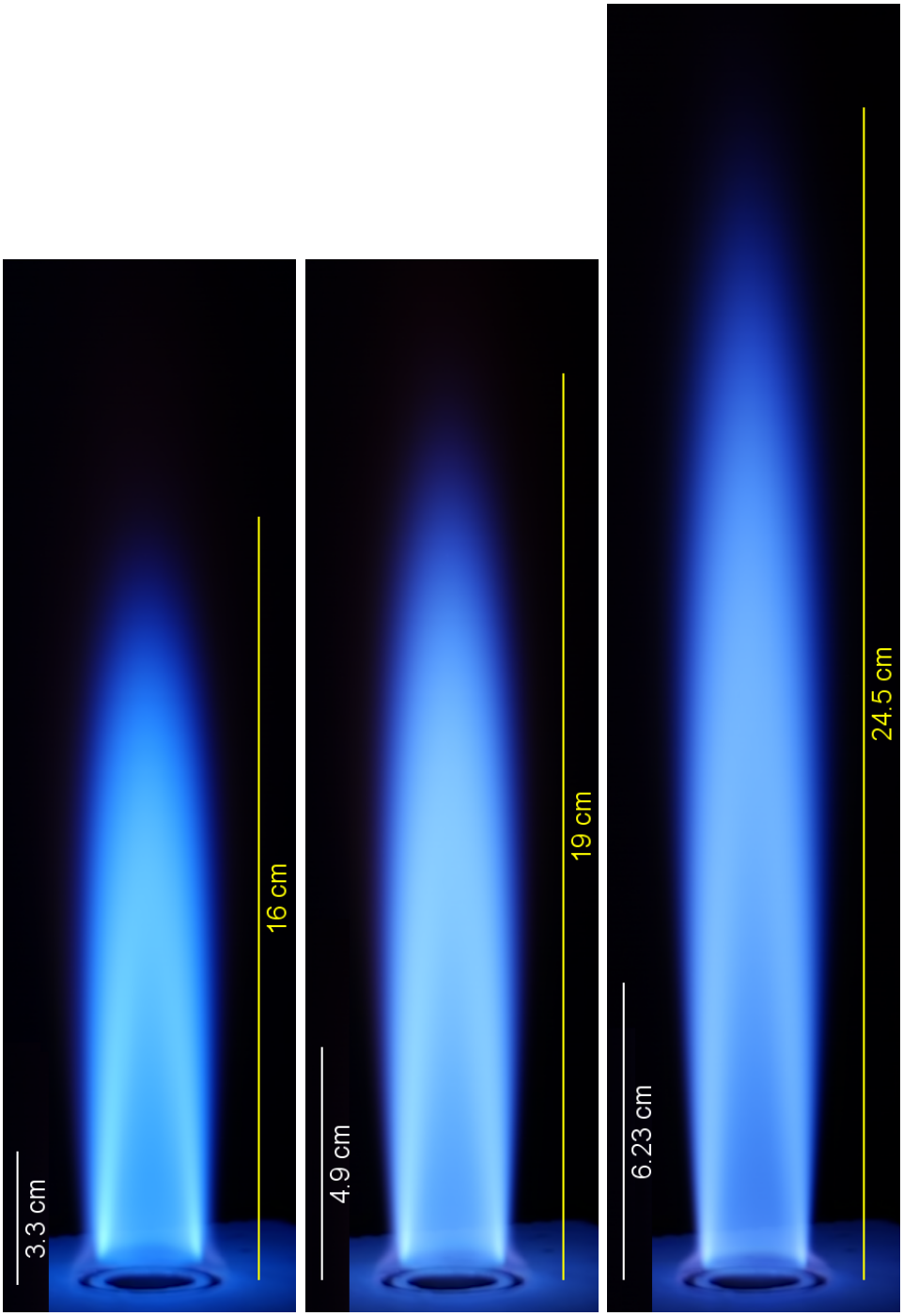

Fig. 4.1. Flame images with 62 % blockage ratio of turbulence generator plate. (left to right: Re 10000, 12500, and 15000)

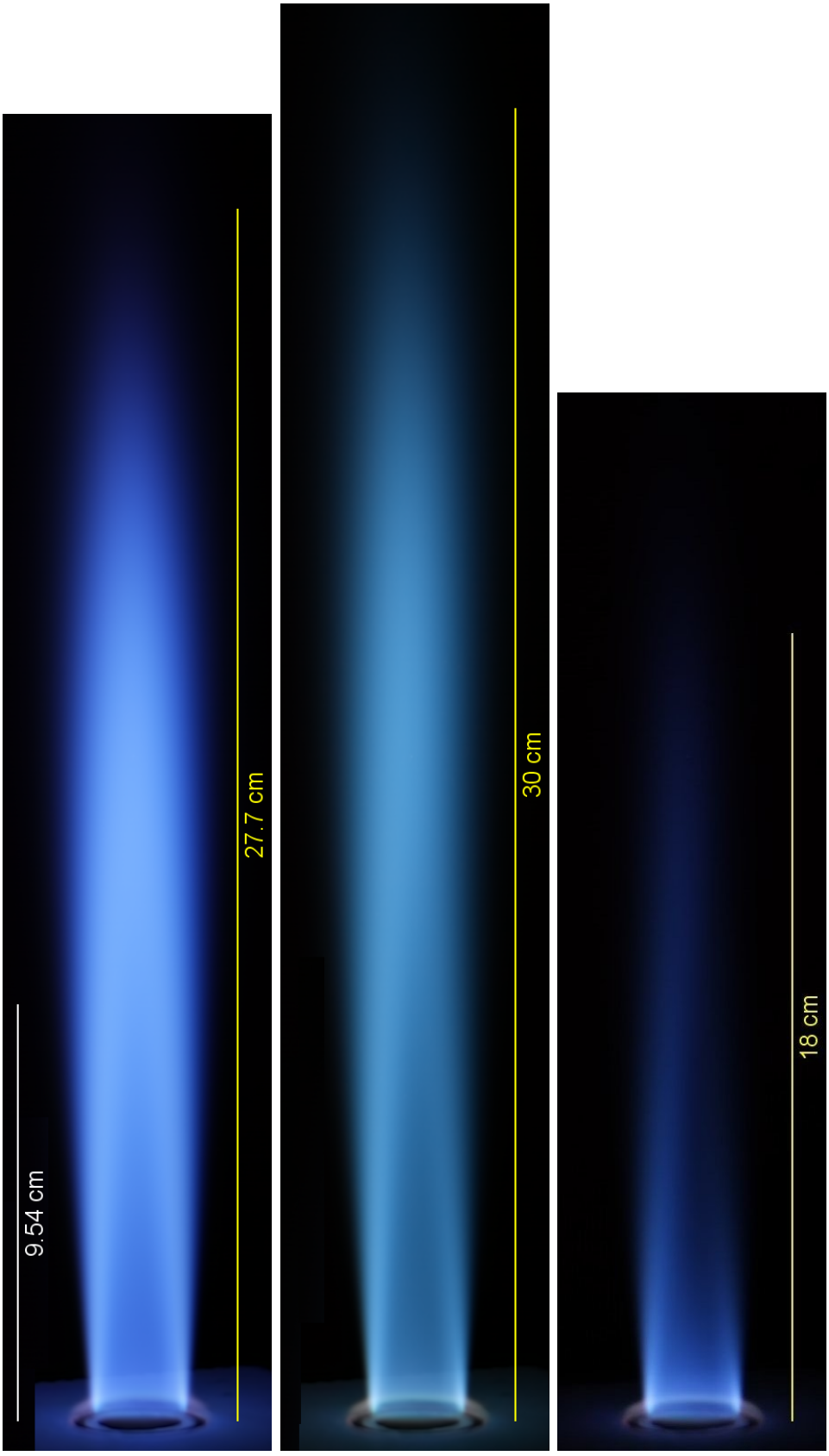

Fig. 4.2. Flame images with 62 % blockage ratio of turbulence generator plate. (left to right: Re 17500, 20000, and 22500)

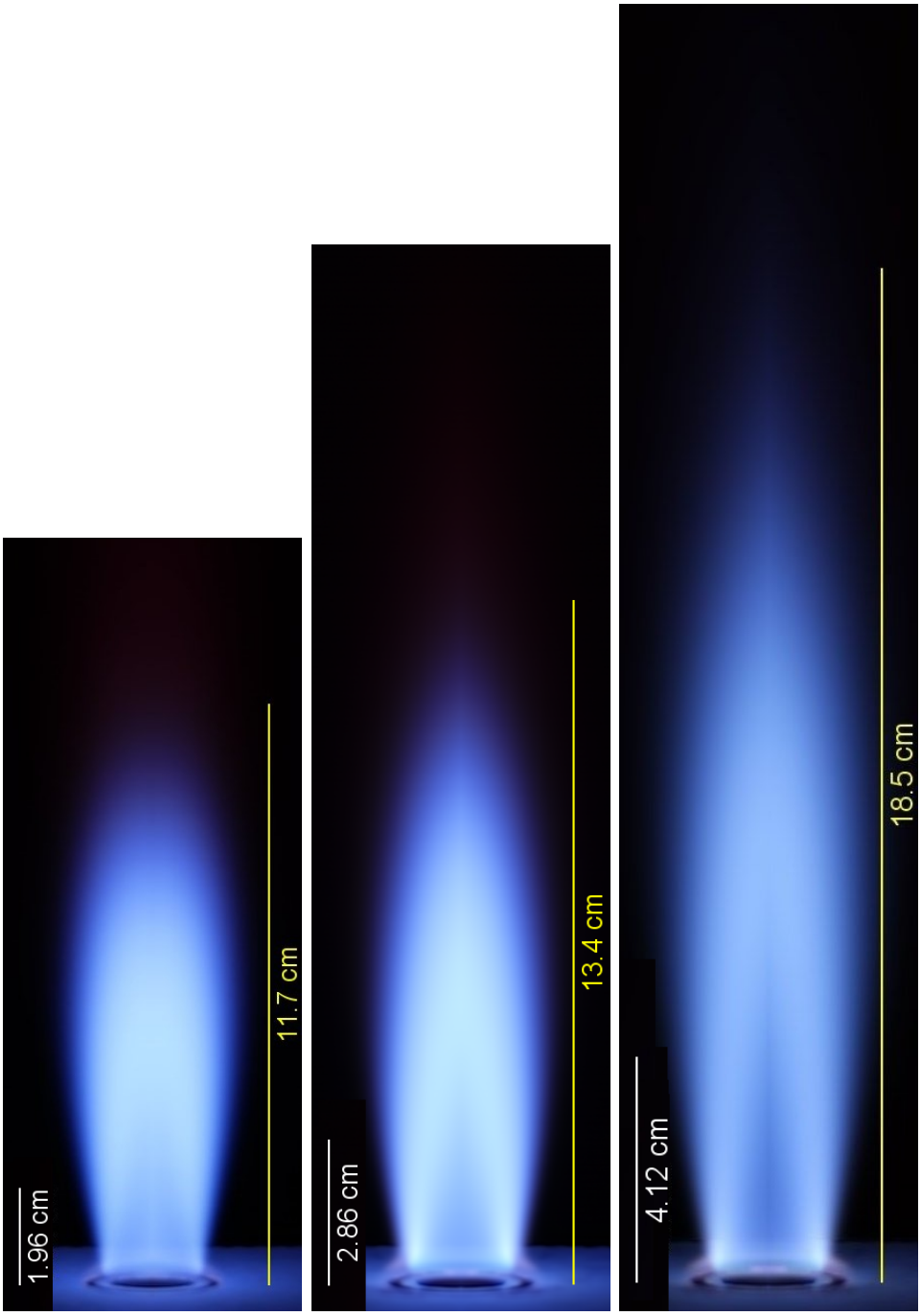

Fig. 4.3. Flame images with 86 % blockage ratio of turbulence generator plate. (left to right: Re 10000, 12500, and 15000)

Fig. 4.4. Flame images with 86 % blockage ratio of turbulence generator plate. (left to right: Re 17500 and 20000)

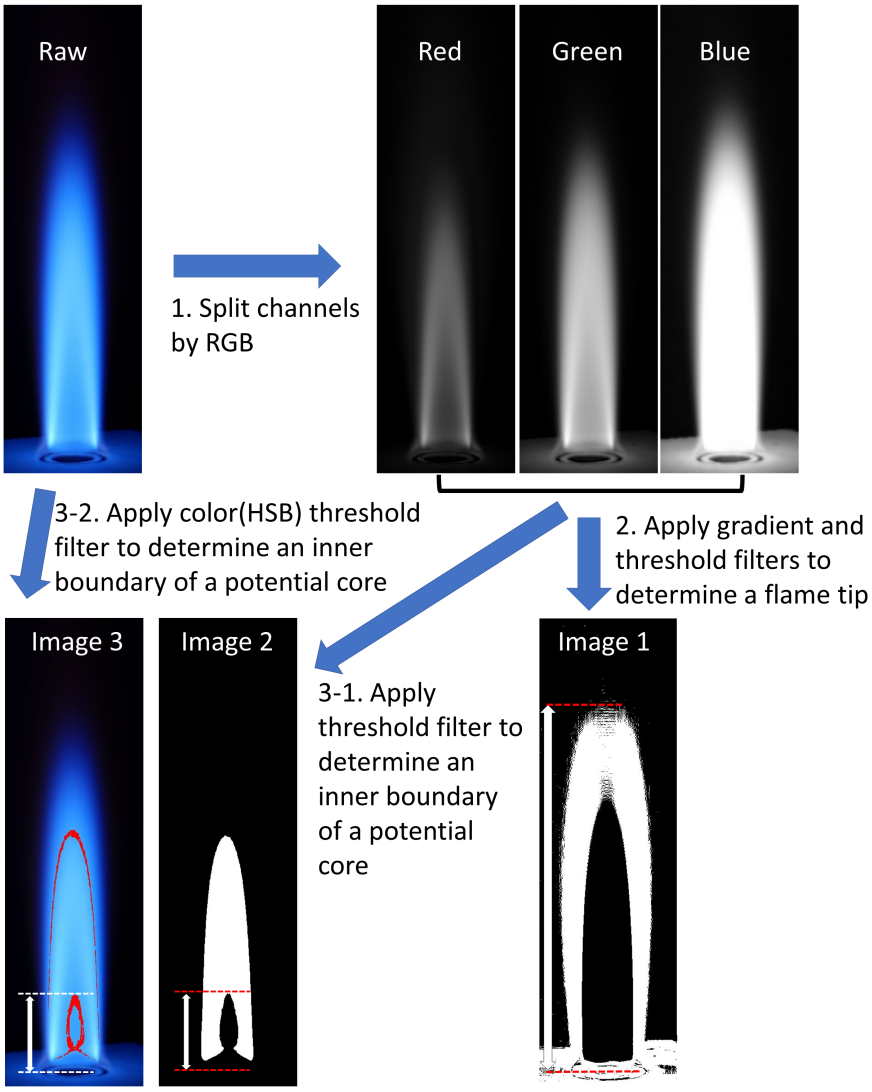

Fig. 4.5. Procedure of image processing to determine a flame tip and an inner boundary of a potential core

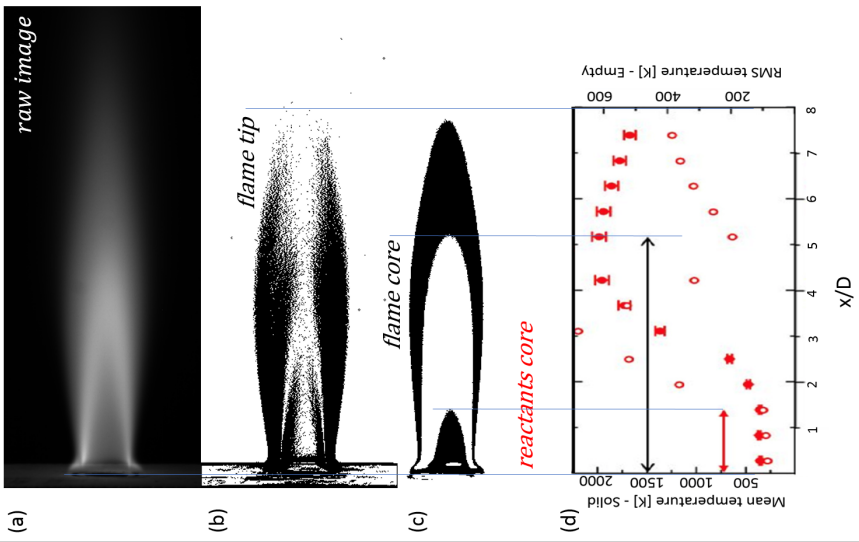

Fig. 4.6. Validation for the determination of a potential core through a flame image. Figure (a), (b), and (c) are from image processing. (d) is temperature profile measured by coherent anti-Stokes scattering (CARS)

5. PARTICLE IMAGE VELOCIMETRY ON TURBULENT PREMIXED FLAMES

Particle image velocimetry (PIV) is performed in order to investigate flow structure. Stereo particle images velocimetry (SPIV or stereo PIV) is mainly used to examine the flow structure, but planar particle image velocimetry is also utilized to support SPIV in the sense of accuracy.

5.1 Stereoscopic particle image velocimetry

Most fluid flows are three-dimensional flows. The flames from the PARAT burner, as shown in the previous chapter, cannot be an exception. Simultaneous measurement of three velocity components is essential for the analysis of three-dimensional flows. Planar PIV technique using a single camera provides only in-plane velocity components, which are two components. Stereo PIV technique, however, offers out-of-plane velocity component as well as in-plane velocity components using depth-perception employing two cameras simultaneously. Such dual camera systems resemble the binocular vision that allows human beings to distinguish between near objects and far objects. Fundamentally, a single camera cannot resolve the out-of-plane motion. Instead, the out-of-plane component is projected on to the image plane and causes an error in the in-plane component due to perspective. The stereoscopic PIV method can eliminate the perspective error, yielding accurate three-dimensional velocity data. In order to measure three-dimensional particle displacements, a processing algorithm characterizes this situation as having three unknowns Δx Δy Δz) with a single camera providing only two equations. The addition of a second, different camera, provides two additional equations which may be used to solve for the three-dimensional information.

Accurate calibration is an essential prerequisite for measuring accurately the three velocity components. Mostly, calibration is achieved by placing a planar calibration target with a regularly spaced grid of marks at exactly the position of the light sheet and moving the target by a specified amount in the out-of-plane direction. From the information of the images of the calibration target captured at multiple positions in the out-of-plane direction, the mapping functions are calculated. The mapping functions are the functions that transfer coordinates from the image world to the real world.

A disparity vector map is computed on the real particle images by cross-correlation of the images from cameras 1 and 2 to determine if the calibration plate coincides with the light sheet. This determination is done in terms of distance and angle. From the disparity vectors, the actual position of the laser sheet in space is fitted and the mapping functions are corrected accordingly. From the computed correlation maps, the position and thickness of the two laser sheets can be derived to determine the thickness, degree of overlap and the flatness of the two sheets.

Some general recommendation for stereo PIV as described by Raffel et al. [113] are:

- Multi-level or translated targets provide a good calibration environment.
- Calibration from a single image of a planar target is possible but should only be used if translation is not possible.
- For optimum measurement accuracy the enclosed angle between the camera viewing axes should be close to 90°.
- The unavoidable misalignment between calibration target and light sheet plane requires disparity correction or self-calibration schemes using the actual particle images.
- Disparity correction can also be used to correct for movement of the cameras during the measurements (i.e. vibration).

- The minimum PIV sample size should be at least the same size as the light sheet thickness.

- Image reconstruction should use in appropriate image interpolation schemes. Iterative image deformation and image back-projection can be combined in a single step for the best performance.

5.2 Experimental setup

A stereo PIV system was implemented to the burner in order to investigate flow structure in a flame. A schematic diagram of stereoscopic PIV system is shown in Fig. 5.1. This system consists of a double-pulsed, frequency-doubled, Q-switched Nd:YAG laser (Spectra-Physics Quanta-Ray GCR200 PIV400-10), an optical system, and two high-speed CCD cameras (PIVCAM 10-30, TSI Inc., 1000x1016 pixels) with two camera lenses (Tamron AF 28-300 mm F3.5 lenses). The fundamental wavelength of the laser is 1064 nm. The laser operates at 532 nm after the second harmonic crystal and emits 400 mJ per pulse at 10Hz, with a pulse duration of 9 ns. The illumination of seeded tracer particles was achieved using the 532 nm laser. Images of Mie scattering from the particles were collected through the two high-speed CCD cameras. The particle images were recorded through two TSI 600067 Frame Grabber after the two camera lenses. A laser-pulse synchronizer (Model: 610034, TSI Inc.) was used to synchronize the laser and the CCD cameras. Two CCD cameras have 45° angle with respect to orthogonal plane to a laser sheet. Both cameras were adapted with Scheimpflug adaptors in order to adjust a depth of field with a laser sheet. The laser beam was formed into a 50 mm diameter collimated beam using spherical lenses (f1 = - 15 mm, f2 = 50 mm) and focused to a waist using a cylindrical lens (f3 = 200 mm). The thickness of laser sheet was 800 m and the visualized flow field was 40 mm x 40 mm. A single-level calibration plate (Fig. 5.2) was used to build a three-dimensional mapping model for stereo PIV reconstruction as well as to align the laser sheet and cameras. Since a single-level calibration plate was utilized, a

motorized linear slide was used to move the calibration plate. This allows to build multiple calibration planes for a three-dimensional reconstruction mapping model. The sampling frequency was 10 Hz and the temporal separation, t, was between 7 and 12 s. The temporal separation was adjusted depending on calculated bulk velocity. The pixel resolution was 42 m/pixel and the spatial resolution is 0.7 mm x 0.7 mm x 0.8 mm. Nominal diameter 0.5 m alumina (Al_2O_3) particles were seeded into the air flow after heating at 100C for 24 hours. Stokes number reflect how well seeded particles characterize the flow behavior is 0.003. One thousand particle image pairs were captured for statistical analysis. Images were capture at the center of the burner. To capture images at the different axial location, a linear slide was utilized for moving the burner up and down.

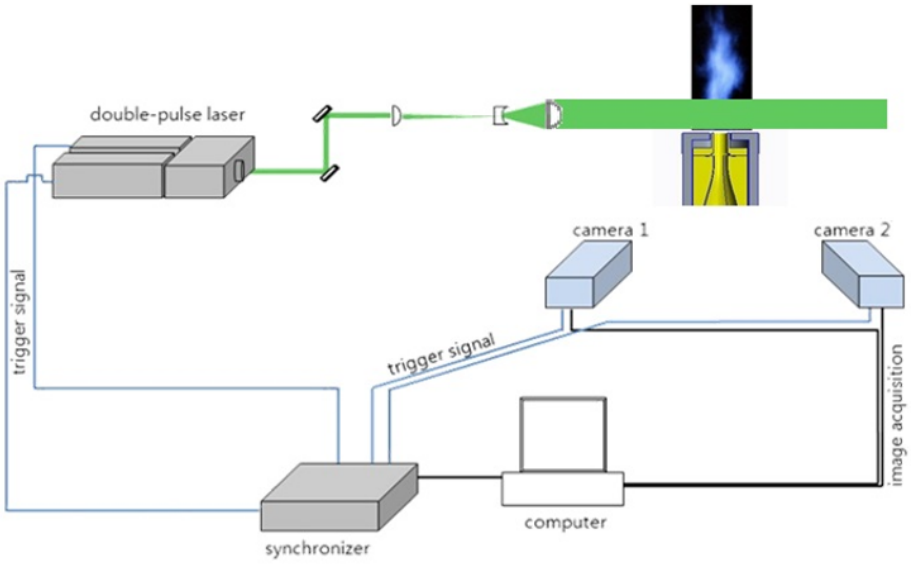

Fig. 5.1. Experimental setup of the stereo PIV system applied to characterize flow field of flames of PARAT burner.

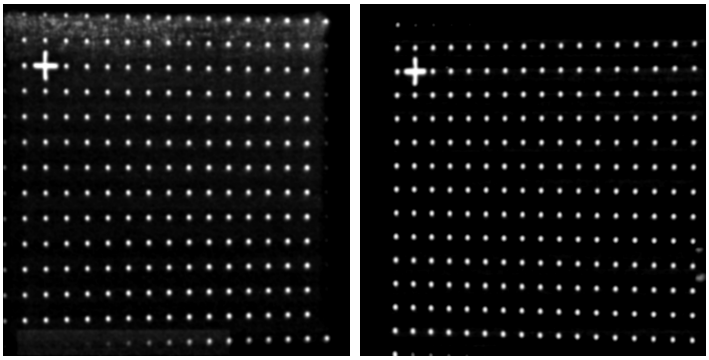

Fig. 5.2. A single-level calibration plate used to to build a three-dimensional mapping model for stereo PIV reconstruction as well as to align the laser sheet and cameras. The left image is a view from left side w.r.t the center of the burner. The right image is a view from right side w.r.t the center of the burner.

5.3 PIV processing

For the analysis of stereo PIV, PRANA [160] software was used. As a three-dimensional mapping model which is used to dewarp the coordinates of images to the coordinate of real-world, third-order polynomial model was selected. Self-calibration procedure [161] was adopted to correct the disparity between two cameras due to misalignment as shown in Fig. 5.4. The average X Disparity is 4.213 Pixels, the average Y Disparity is 0.46408 Pixels, the rms X Disparity is 3.9415 Pixels, the rms Y Disparity is 0.42401 Pixels. These values corresponds to the misalignment of alpha = 0.791843 deg, beta = 0.77327 deg, gamma = 0.118655 deg, δ z = 0.531872 mm, δ x = 0.214525 mm, and δ y = 0.0111554 mm.

Before the analysis of stereo PIV, an image processing was performed to remove background and noise in the particle images. The minimum intensity over all images was subtracted for the particle images, and then, image intensity was normalized. The particle images for non-reacting flow and reacting flow are shown in Fig. 5.3. In the image of non-reacting flow, there are two border lines at left and right sides of the jet flow. The border lines are the shear layers between the jet flow and boundary area. Vortex by mixing of the jet flow and boundary air also can be seen. In the

image of reacting flow, however, there are two border lines at left and right sides of reactants. The border lines are between reactants and products. That is, the border lines present the reaction layer. The reason is because the density of products is generally 5 times less than the density of reactants. This leads to decreasing of particle density in the gas resulting in less particle images in products' area than reactants' area. The reaction layer will be seen more clear in OH PLIF or CH/OH PLIF, which will be introduced in the next chapter.

To calculate flow velocity vectors, multi-pass multi-grid window-deform with discrete window offset was employed. Corresponding to multigrid method, bicubic multigrid method was used for velocity interpolation with Gaussian smoothing. The interrogation window sizes were 64x64 pix^2 and 50% overlap (first pass) and 25x25 pix^2 and 50% overlap (final pass). Corresponding to window-deform method, Sinc with Blackman filter deform method was used for image deformation. The image deformation was converged within 5 times, seldom within 10 times. To calculate particle displacement, robust phase correlation (RPC) [162] and three-point Gaussian estimator for subpixel peaks were implemented. Stereo reconstruction process was achieved using a generalized reconstruction (Soloff reconstruction [118]). Error sources based on focusing effects, diffraction and aberration artifacts, forward and backward scattering intensity variation, and calibration error were tried to be minimized so that uncertainty is lower than turbulent fluctuation level. In addition, the reason why this study use self-calibration is that the choice of the stereo reconstruction algorithm and camera calibration model does not give a significant effect on the out-of-plane velocity error, however, an accurate self-calibration is vital to producing high-quality stereo reconstructions [163]. Following this, an accurate 2D PIV process is essential for high-quality stereo 2D3C PIV results.

Uncertainty analysis is achieved through two methods: (1) image condition investigation [113] and (2) PPR based on cross correlation [133,135]. The first method requires displacement, displacement gradients, seeding density in a certain interrogation window size and particle image diameter on the true errors for a given measurement.

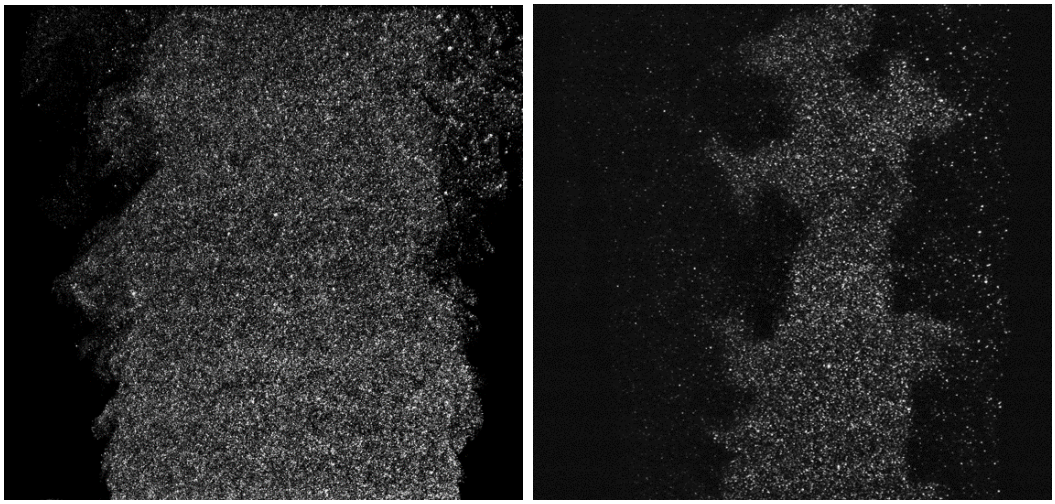

Fig. 5.3. Seeded particle images of non-reacting flow (left) and reacting flow (right). The images are after background removal and intensity normalization

This method gives 0.02 pix uncertainty. The second method requires PPR that is originated from the cross-correlation plane. This method provides local uncertainty in the image plane for a given measurement. The magnitude of uncertainty through PPR analysis is larger than the one from image condition analysis. The uncertainty from the second method gives between 0.1 and 0.2 pix/frame. In addition to the uncertainty, we observed an edge effect on PIV result. Specifically, there was small velocity decreasing right above the burner exit, 3% difference from the streamwise velocity along the burner center line. There are two reasons. The first reason is the use of multipass multigrid PIV algorithm that was utilized in order to enhance the accuracy of PIV calculation. At the initial grid size, the interrogation window includes the outside of the burner exit. The second reason is the burner surface in the particle image. Even though background removal was applied, the image of the burner surface cannot be removed. Thus, the velocity vector in a certain range (from x/D=0 to x/D=0.13) was not selected for this study.

Less than 8% of vectors were found as outliers (erroneous vectors) in the final pass using the universal outlier detection method. Most of the outliers were located

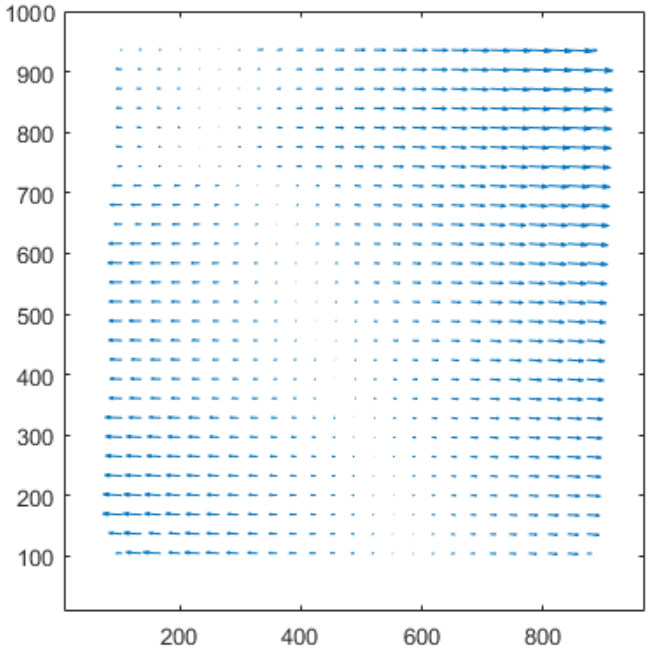

Fig. 5.4. A disparity map showing a misalignment between the laser sheet and the image plane.

inside the shear layer due to lack of seeding particles. The universal outlier detection was performed for 3x3 vectors. Vectors more than 3 standard deviations from the mean were removed from the ensemble for mean and RMS calculation. The PIV measurements do not resolve the smallest scale of velocity fluctuations (0.05 mm). Therefore, the uncertainties in the turbulent fluctuation measurements result from both spatial averaging effects and measurement uncertainties.

Following the PPR uncertainty method [133, 135], our PIV data has the upper limit of uncertainty, 0.18 pixel, and the lower limit of uncertainty, 0.10 pixel for 68.5 % confidence level. In the case of the 95 % confidence level, the PIV data has the upper limit of uncertainty, 0.60 pixel, and the lower limit of uncertainty, 0.014 pixel. The graphs are shown in this study use 68.5 % confidence level with the averaged value of upper and lower limits. The range of uncertainty bar in the graphs, however, is too small to present in the graphs. The uncertainty error bar is hidden by dots in

the graphs. A reader can understand the magnitude of uncertainty is as much as the size of dots in the graphs.

5.4 Results and discussion

Velocity profiles with a contour plot of total velocity are shown in Fig. 5.5. Reynolds number is 10,000. Flow direction is presented in arrows, and the magnitude of the flow direction is shown in color. The velocity presented here is total velocity, $V = \sqrt{u^2 + v^2 + w^2}$. Uniform blue areas, mean o m/s, on the left-bottom and right-bottom side of the figures are due to masks to prevent erroneous vector calculation during PIV processing. The area has almost no particles because it is the outside of burner (nozzle) exit and right above the burner surface. The non-reacting flow has a freely propagating jet flow with decreasing core area (red area in the figure) and an approximately constant width of jet flow. The reacting flow, on the other hand, has a expanding jet flow with increasing core area (red area in the figure) and a broaden width of jet flow. The plot of 86% B.R dose not have a difference with the plot of 62% B.R shown in Fig. 5.5.

Fig. 5.6 shows more detailed velocity profiles along radial direction for the reacting case of the Fig. 5.5 at three axial locations where are exit, 2D (36 mm above the exit), and 4D (72 mm above the exit). Because stereo PIV was performed for the flows, three velocity components can be extracted. From the figure, a few observations are available : (1) extremely different streamwise velocity profiles at exit with the turbulence generator plates of 62% and 86% blockage ratio with the same flow rate, equivalence ratio, burner configuration except the plates, (2) the different streamwise velocity profiles are converged to the same velocity profile as approaching to x/D = 4 (D is the burner diameter 18.2 mm), and (3) locally isotropic turbulent fluctuation based on the same magnitude of rms velocities u_{rms}, v_{rms}, and w_{rms}. There is no significant observation of the radial and out-of-plane velocity profiles except radially

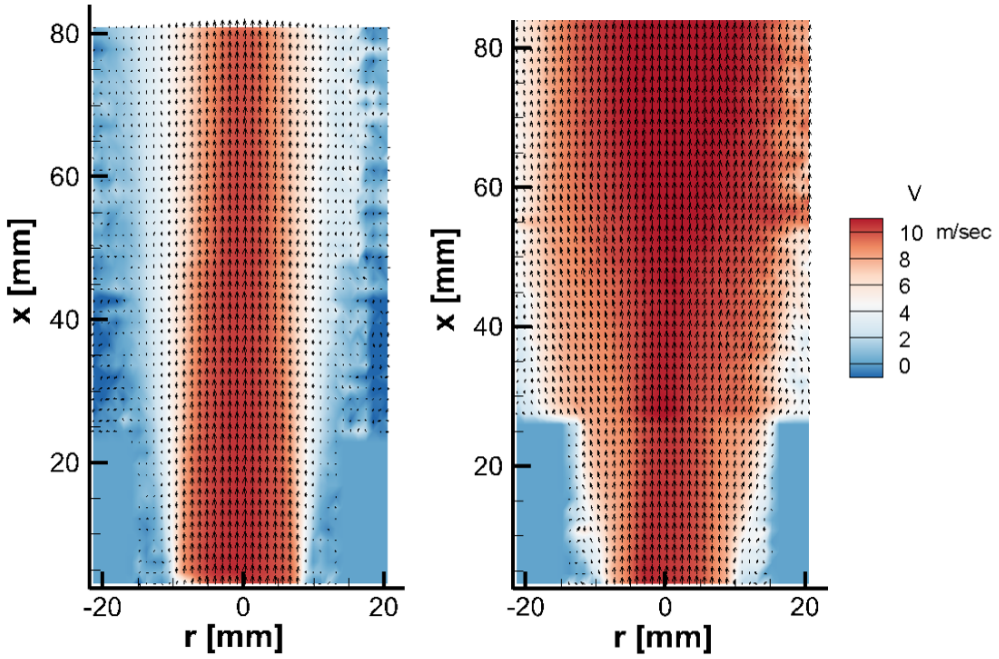

Fig. 5.5. Ensemble-averaged velocity profiles. Velocity profiles of non-reacting flow (left) and reacting flow (right) of 62 % B.R. Reynolds number is 10,000

outward flow exists at near x/D=2. This is because the flows are freely propagating jet flow and the measurement is at the center of the burner.

The previous studies [81,107] suggest that the threshold of the stream and vortex dominated regimes is between a B.R. of 70% and 80% for non-reacting jets. From the stereo PIV measurements reported here, the threshold appears to be between 62% and 86%, which is consistent with the past data. There is a sudden jump in the turbulence level between B.R. 62% and 86%. As the B.R. increases, the turbulence level rises as many studies have revealed. However, turbulence level increases sharply from 18% to 40% when B.R. changes from 62% to 86%. Second, the changing shape of the mean flow profiles indicate that there is a threshold dividing the flow profiles into two groups. The flow profiles for B.R. 62% has a top-hat profile, while the flow profiles for B.R. 86% has a sharp central cone.

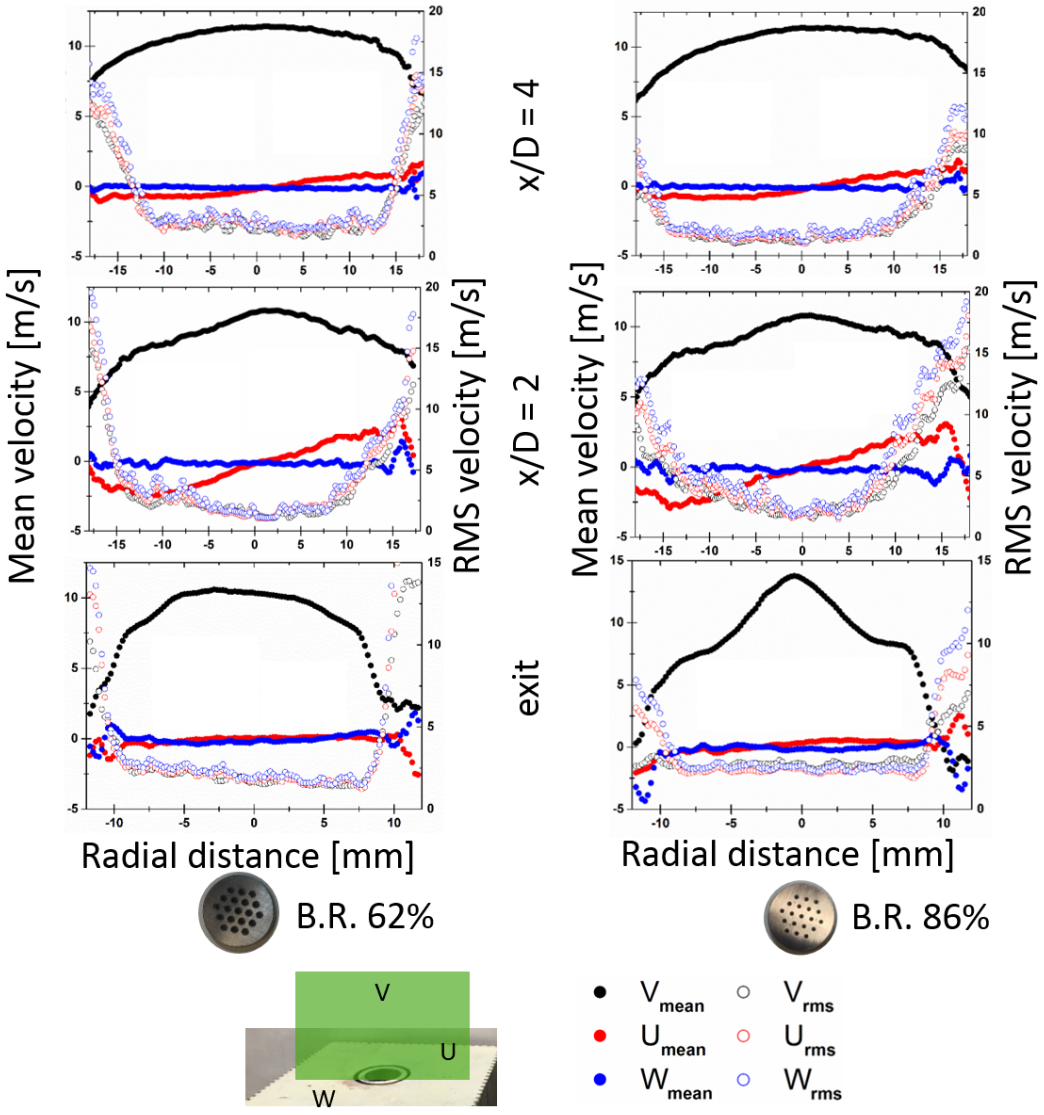

Fig. 5.6. Velocity profiles along radial direction. Velocity profiles of 62 % B.R (left) and velocity profiles of 86 % B.R (right) at three axial locations, exit(x/D=0.13), x/D=2(36 mm above the exit), and x/D=4(72 mm above the exit). Reynolds number is 10,000

Probability density function (PDF) of the three velocity components for the two plates of 62% and 86% B.R at Re 10,000 is shown in Figure 5.7 and 5.8. At the exit, 86% B.R has a broaden width of PDFs compared to 62% B.R resulting in higher rms velocity. But, as approaching to x/D=4, the shape of PDF is getting equal.

As increase Reynolds number by increasing flow rate, velocity is proportionally increased with Reynolds number. In Fig. 5.9, streamwise velocity profiles along radial direction for different Reynolds numbers are presented. The magnitude of mean and rms axial (streamwise) velocities are tabulated in Table 5.1. The reasons why only the streamwise velocity is given are the mean radial and out-of-plane velocities have no noticeable change and the magnitude of the rms radial and out-of-plane velocities can be represented as the rms axial (streamwise) velocity due to isotropic turbulent fluctuation. The streamwise velocity is increased linearly while maintaining the shape of profile. However, the velocity at shear layer (the left-end and right-end of radial distance shown in the graphs) seems to have a fixed value, near 3 m/s.

Axial (streamwise) mean velocity V_{mean} and rms velocity V_{rms} in m/s for B.R. 62% and B.R. 86% flames as indicated in the Table 5.1. Mean and rms axial velocities increase with a higher B.R. As Reynolds number increases, both B.R 62% and 86% generate higher mean and rms streamwise velocities.

The one of the motivation for this study, a decay of streamwise velocity, is shown in Fig. 5.10.

Normalized mean streamwise velocity and normalized rms streamwise velocity for B.R 62% and 86% with different Reynolds numbers at non-reacting condition are presented. It is obvious that the two B.R generate absolutely different decay, and strongly supports the assertion that the two blockage ratios result in significantly different flow regimes. The B.R. 62%, which represents a stream-dominated flow regime shows a decrease of only 5% to 10% in the streamwise velocity between x/D=0 and x/D = 4.5. While the B. R. of 86% causes as much as 40% decrease in the mean streamwise velocity. With respect to rms turbulent fluctuations in the streamwise velocity, the B.R. 62% flame shows a decrement to 80% of the exit rms turbulent

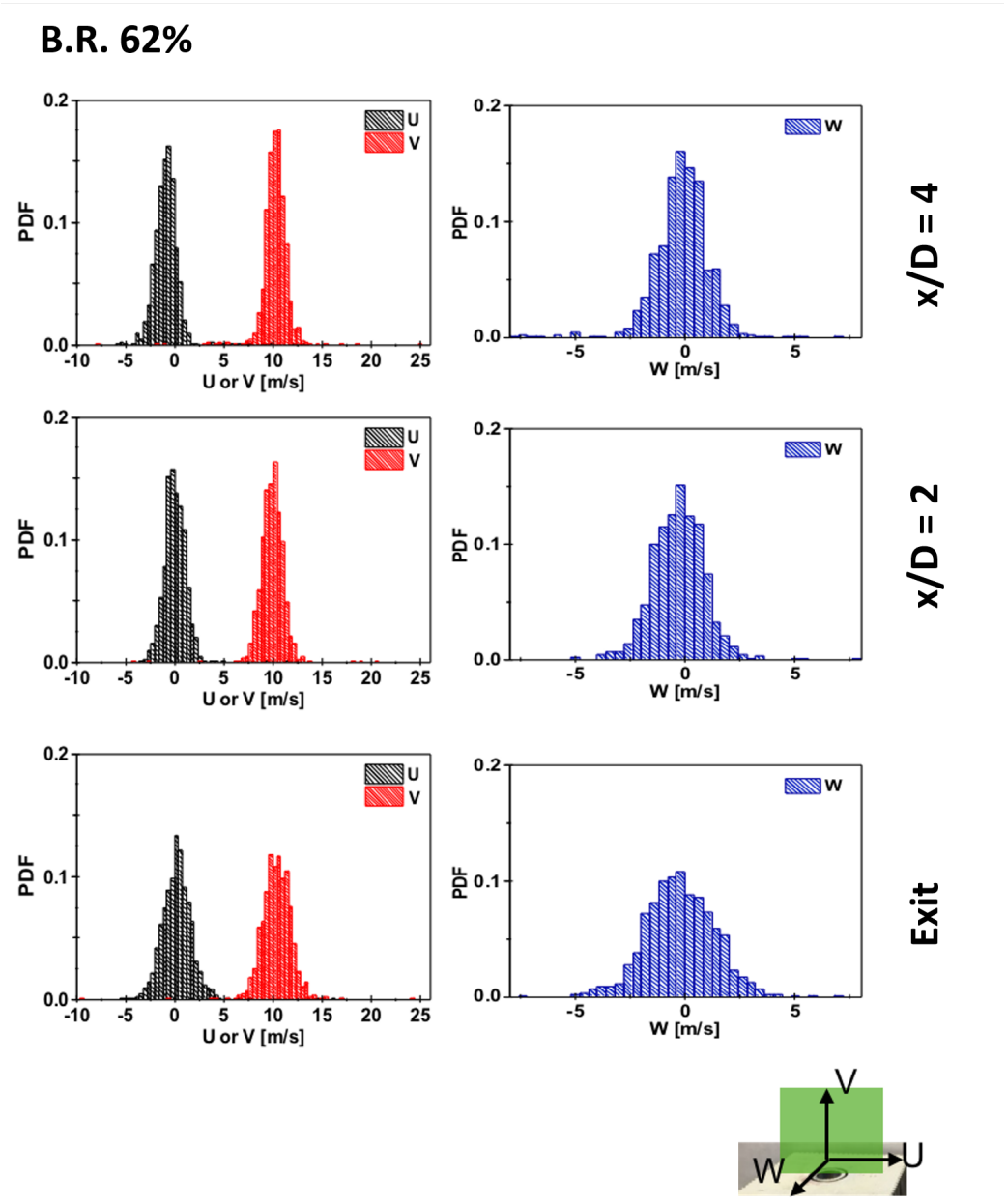

Fig. 5.7. Probability density function (PDF) at three axial locations for 62 % B.R and Reynolds number 10,000. PDF is measured at the three axial locations, exit, 2D(36 mm above the exit), and 4D(72 mm above the exit) along the center of the burner exit.

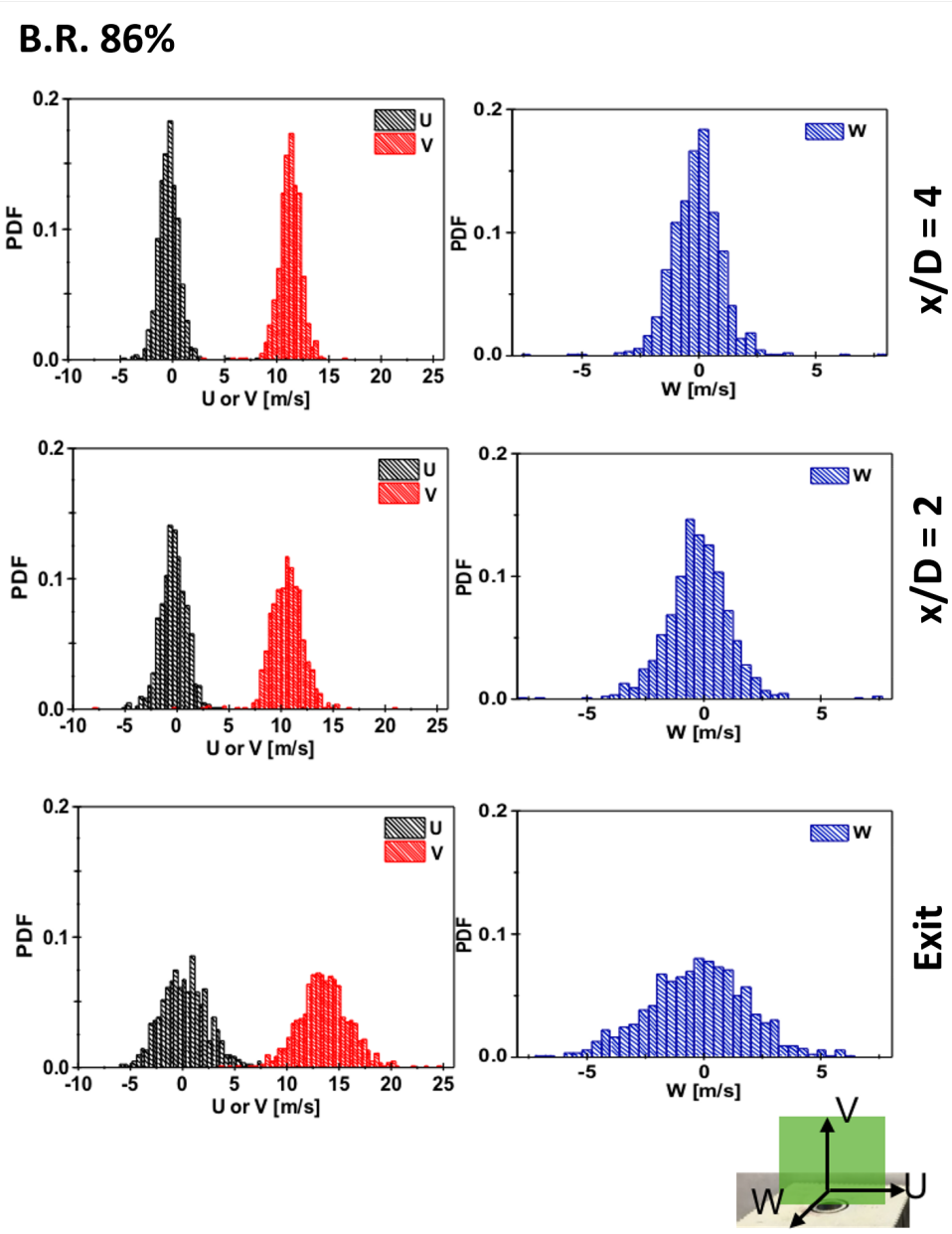

Fig. 5.8. Probability density function (PDF) at three axial locations for 86 % B.R and Reynolds number 10,000. PDF is measured at the three axial locations, exit, 2D(36 mm above the exit), and 4D(72 mm above the exit) along the center of the burner exit

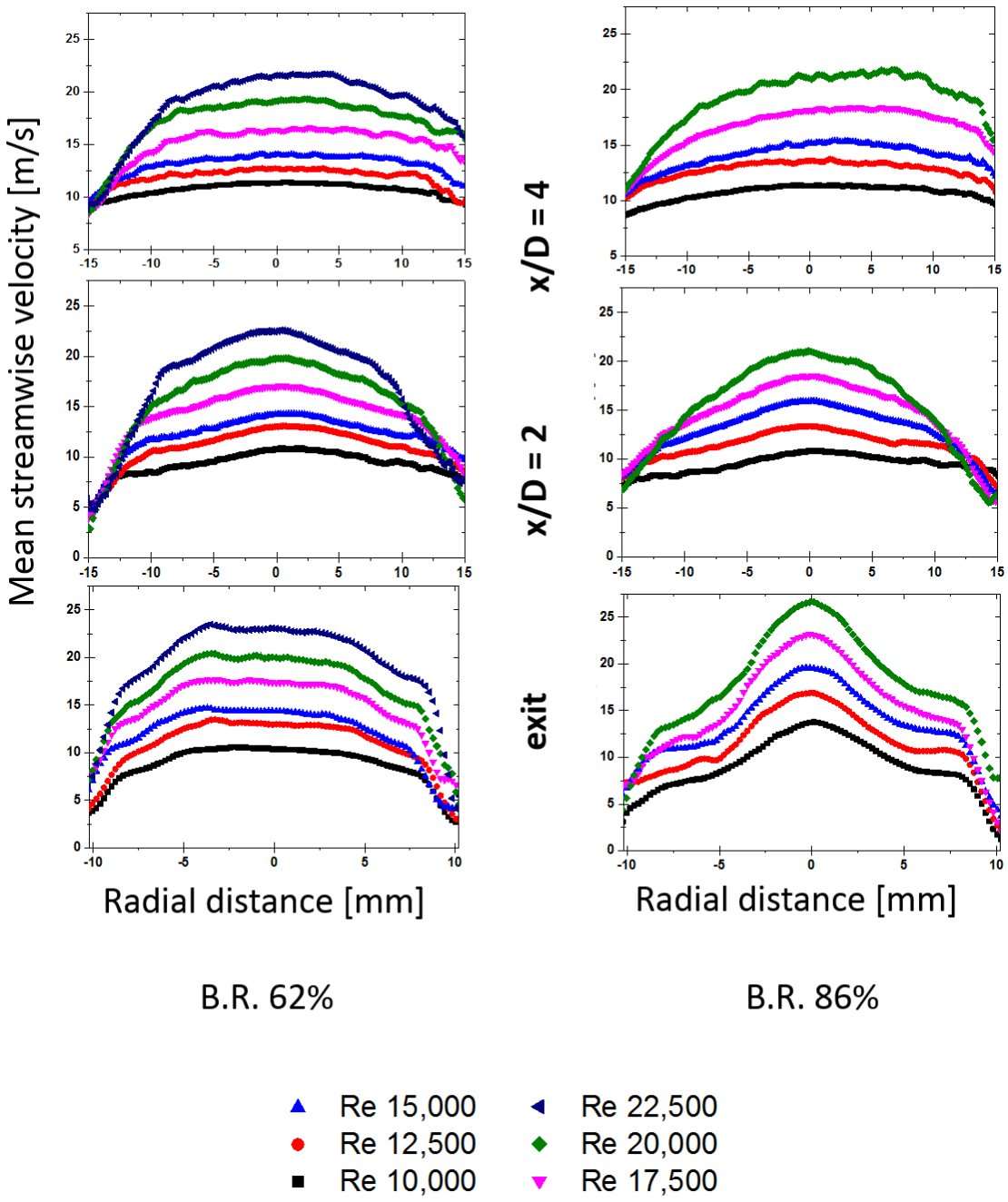

Fig. 5.9. Streamwise velocity profiles along radial direction for all Reynolds numbers performed in this study. Streamwise velocity profiles of 62 % B.R (left) and velocity profiles of 86 % B.R (right) at three axial locations, exit, 2D(36 mm above the exit), and 4D(72 mm above the exit). Reynolds numbers are from 10,000 to 22,500 with 2,500 interval.

Table 5.1.
Properties of flames. Axial (streamwise) mean velocity V_{mean} and rms velocity V_{rms} in m/s for B.R. 62% and B.R. 86%

Re #	10,000	12,500	15,000	17,500	20,000	22,500
B.R. 62%						
V_{mean}	10.8	13.0	15.2	17.0	19.8	22.5
V_{rms}	1.78	2.25	3.15	4.09	4.18	4.47
B.R. 86%						
V_{mean}	13.7	16.9	19.5	23.1	26.6	28.7
V_{rms}	3.10	3.41	4.05	5.56	5.79	5.84

fluctuations at the near 1D axial location and then remains constant until an axial location of 2D. Beyond this location, the normalized rms velocity shows a significant recovery back to the exit value at the 4.5 D location. This is in significant contrast with the continuous decline to values between 50% and 60% at 4.5 D downstream of the burner exit for the B.R. 86% flame.

The mean velocities between non-reacting and reacting flows for Re=10,000 is shown in Fig. 5.11. There is a significant difference in the mean axial (stream-wise) velocity by combustion. In the case of B.R. 62%, the mean axial velocity has no meaningful change at the center area ($-0.2<r/D<0.2$) where there is no combustion happens, while the velocity is slower at the side ($-0.5<r/D<-0.2$ and $0.2<r/D<0.5$)) where combustion is proceeding above the location. In the outer area ($r/D<-0.5$ and $r/D>0.5$), the velocity affected by combustion is higher than a non-reacting flow. In the case of B.R. 86%, the mean axial velocities between reacting and non-reacting flows show the same phenomenon except the center area. The center area for B.R. 86% contains combustion zone which leads to the higher mean velocity affected by combustion. Thus, if the measurement location is in the reaction zone, the velocity is increased. However, the velocity is retarded if the measurement location is below the reaction zone. The radial (span-wise) and azimuthal (out-of-plane) velocities cannot find a significant difference at this location ($x/D=0.13$). It would be helpful to know where the combustion zone is through OH PLIF images such as Fig. 6.4

The RMS velocities between non-reacting and reacting flows for Re=10,000 is shown in Fig. 5.12. Through turbulence by combustion, RMS velocities for all directions are increased. However, the ratio of the increase in B.R. 86% was smaller than the case of B.R. 62%.

The decay of stream-wise mean velocity between non-reacting and reacting flows for Re=10,000 is shown in Fig. 5.13. The gap between two cases are caused by turbulence generated by flame as mentioned in [53]. The two physical models presented in [50]. Interestingly, the gap between two cases can lead to estimation of a height of potential core (Fig. 5.14 and 5.15. When the gap reaches to minimum point, it

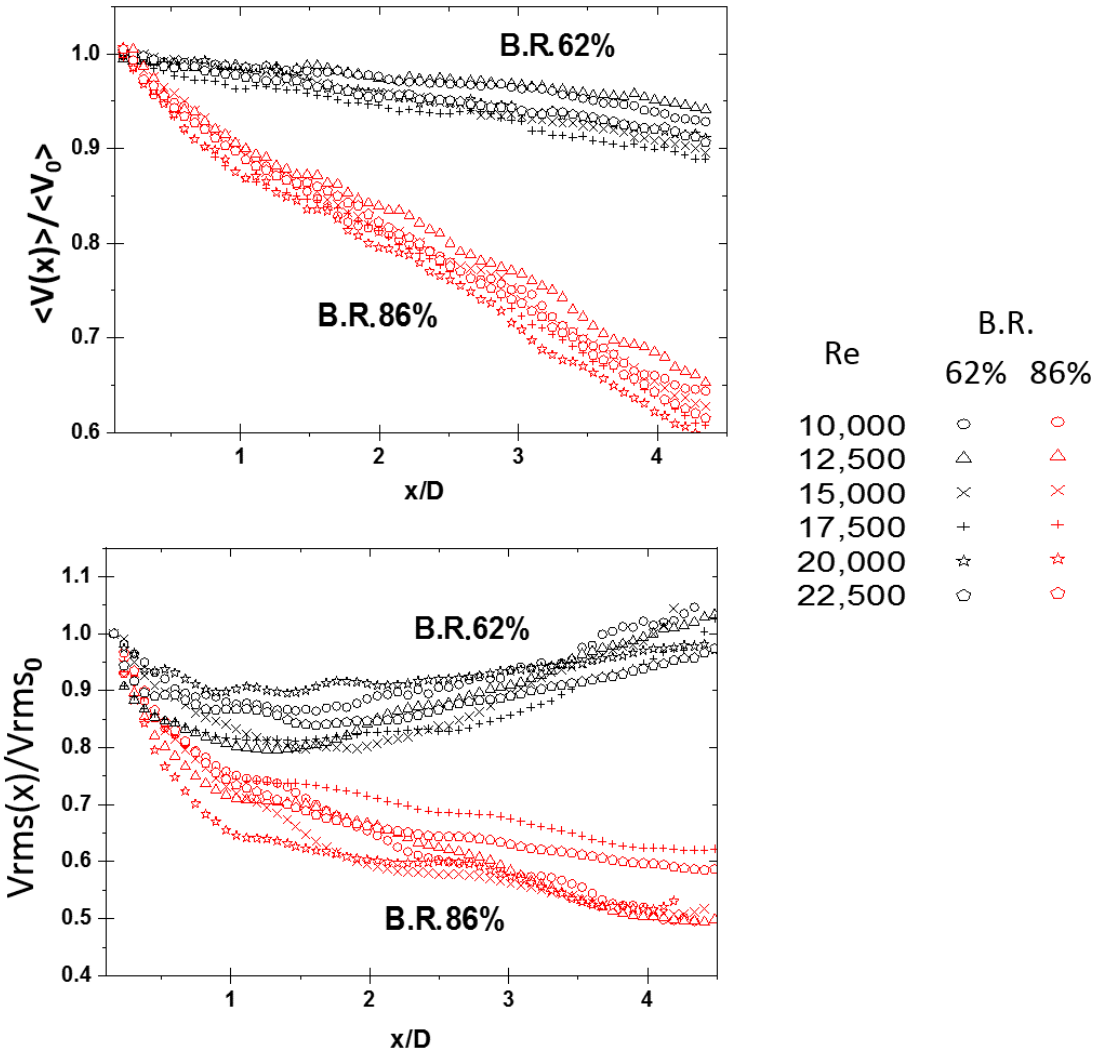

Fig. 5.10. Stream-wise velocity decay along the streamwise direction for B.R 62% and 86%. Normalized mean streamwise velocity (top) and normalized rms streamwise velocity (bottom) are presented.

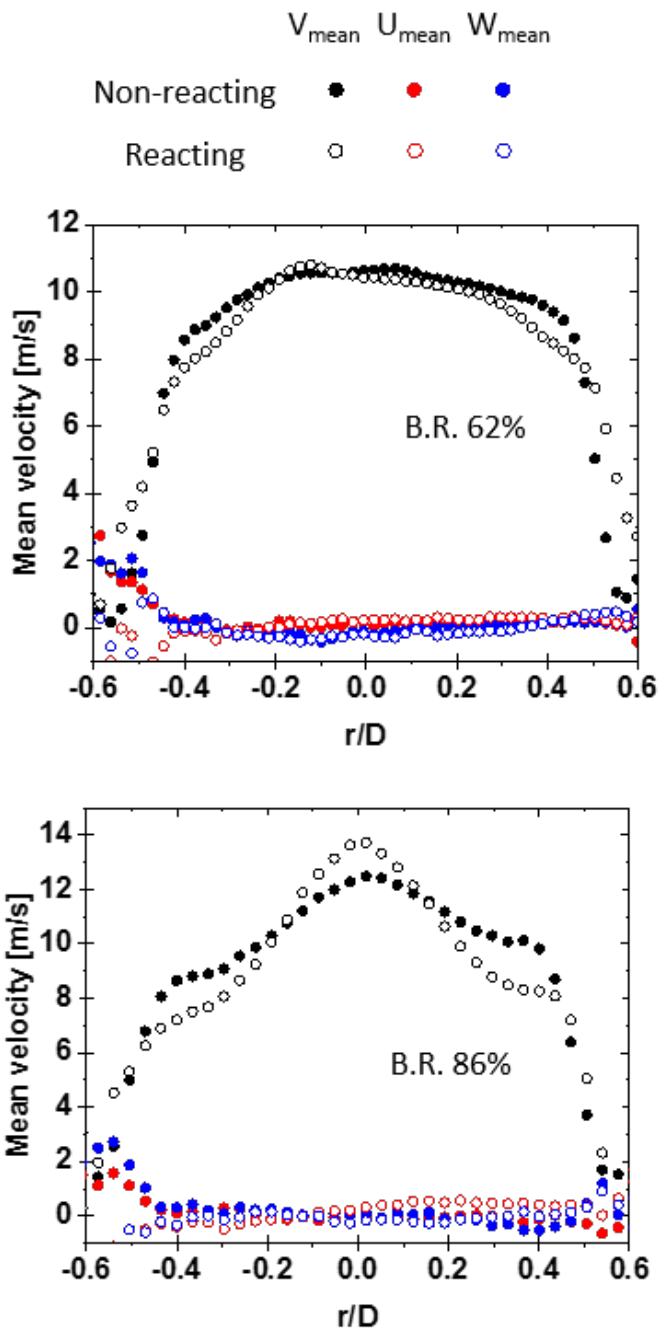

Fig. 5.11. Mean velocities along radial direction for both B.R.s. Re=10,000. x/D=0.13

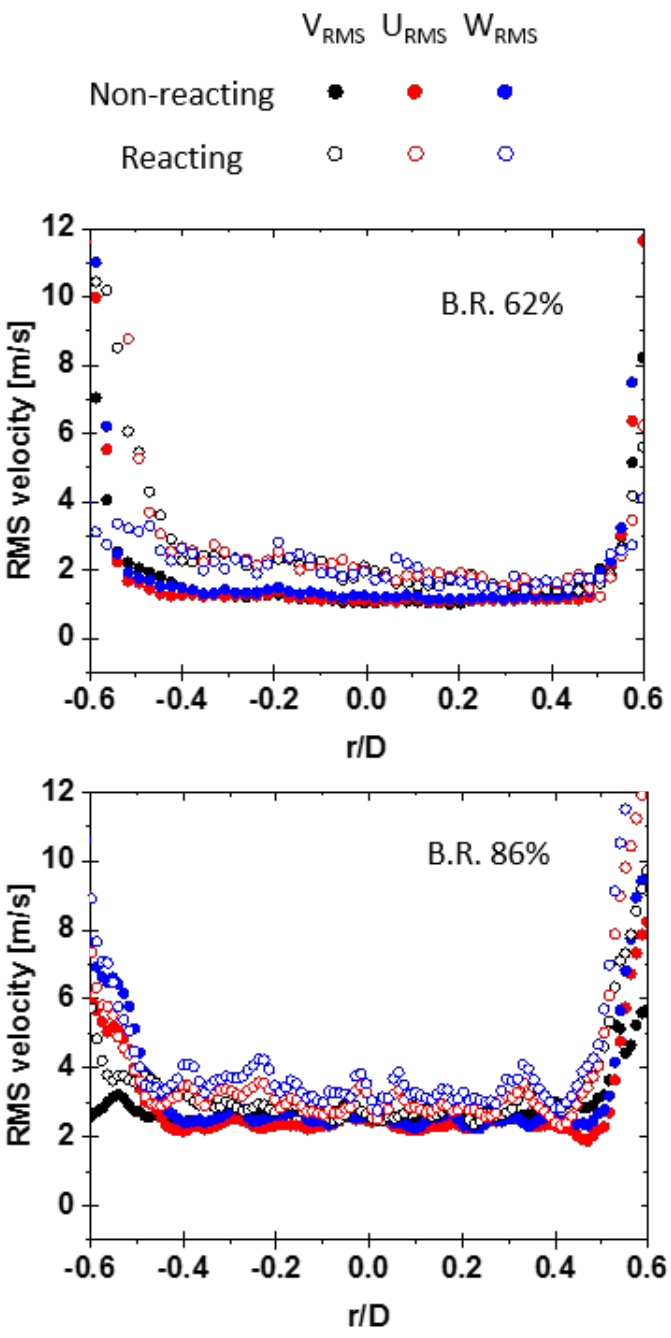

Fig. 5.12. RMS velocities along radial direction for both B.R.s. Re=10,000. x/D=0.13

corresponds to the height of The estimation from a visible image was explained in chapter 4.2. These two estimations with the estimation by CARS are in the good agreement. Now, it can be concluded that streamwise velocity is retarded near the borderline of reactants core and accelerates in a flame where the reaction starts. Simultaneously, rms velocity jumps beyond the fluctuation by a turbulence generator plate due to combustion effect.

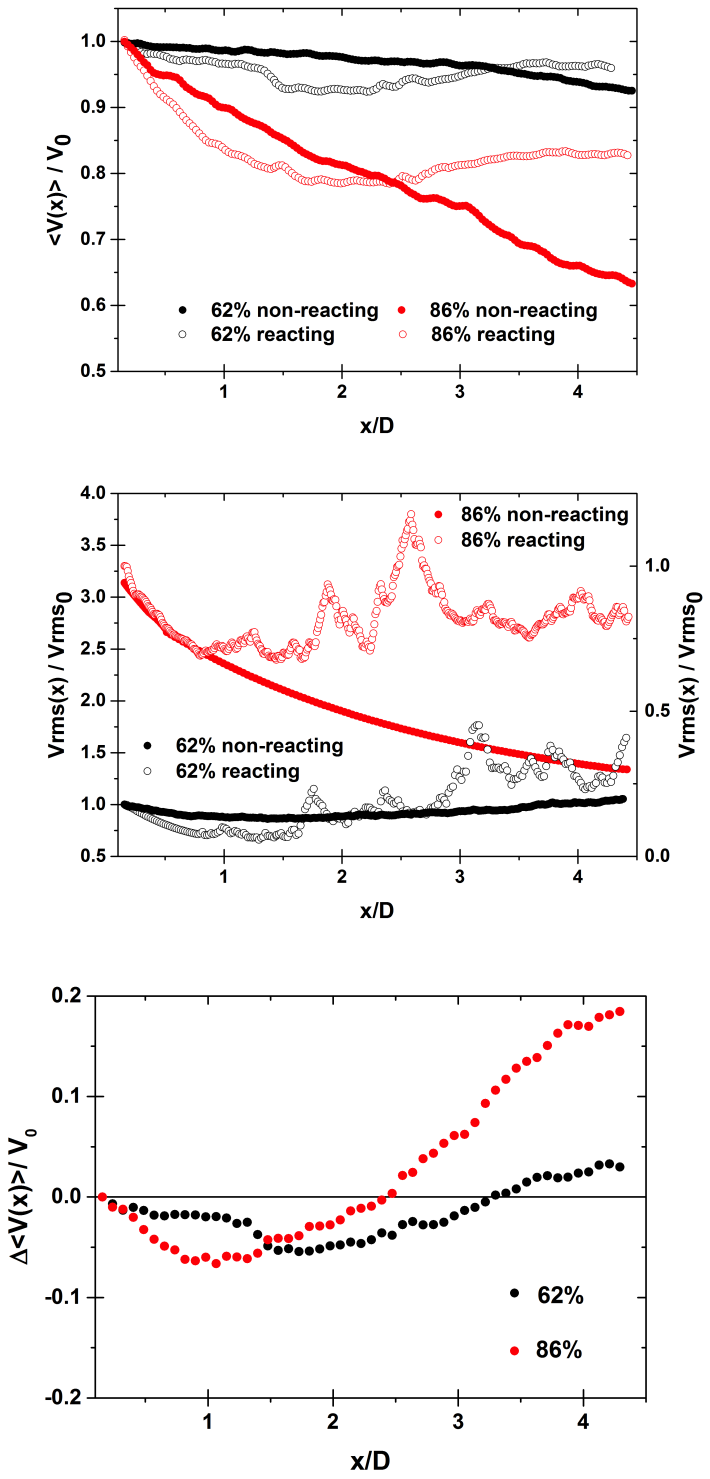

Fig. 5.13. An axial velocity decaying along streamwise direction for both B.R. Reynolds number is 10,000

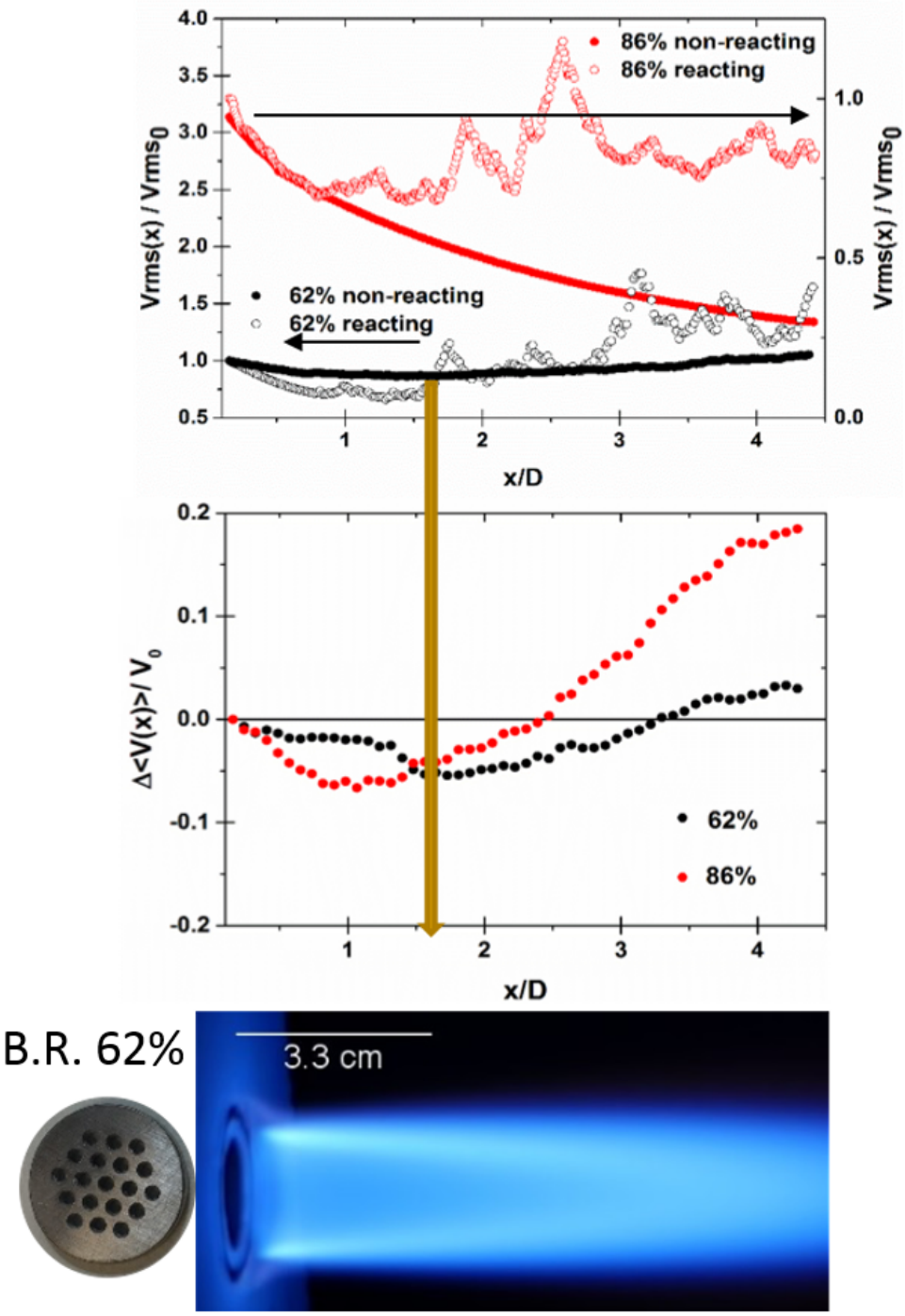

Fig. 5.14. Estimation of a height of a potential core for 62 % B.R using an axial velocity decaying along streamwise direction.

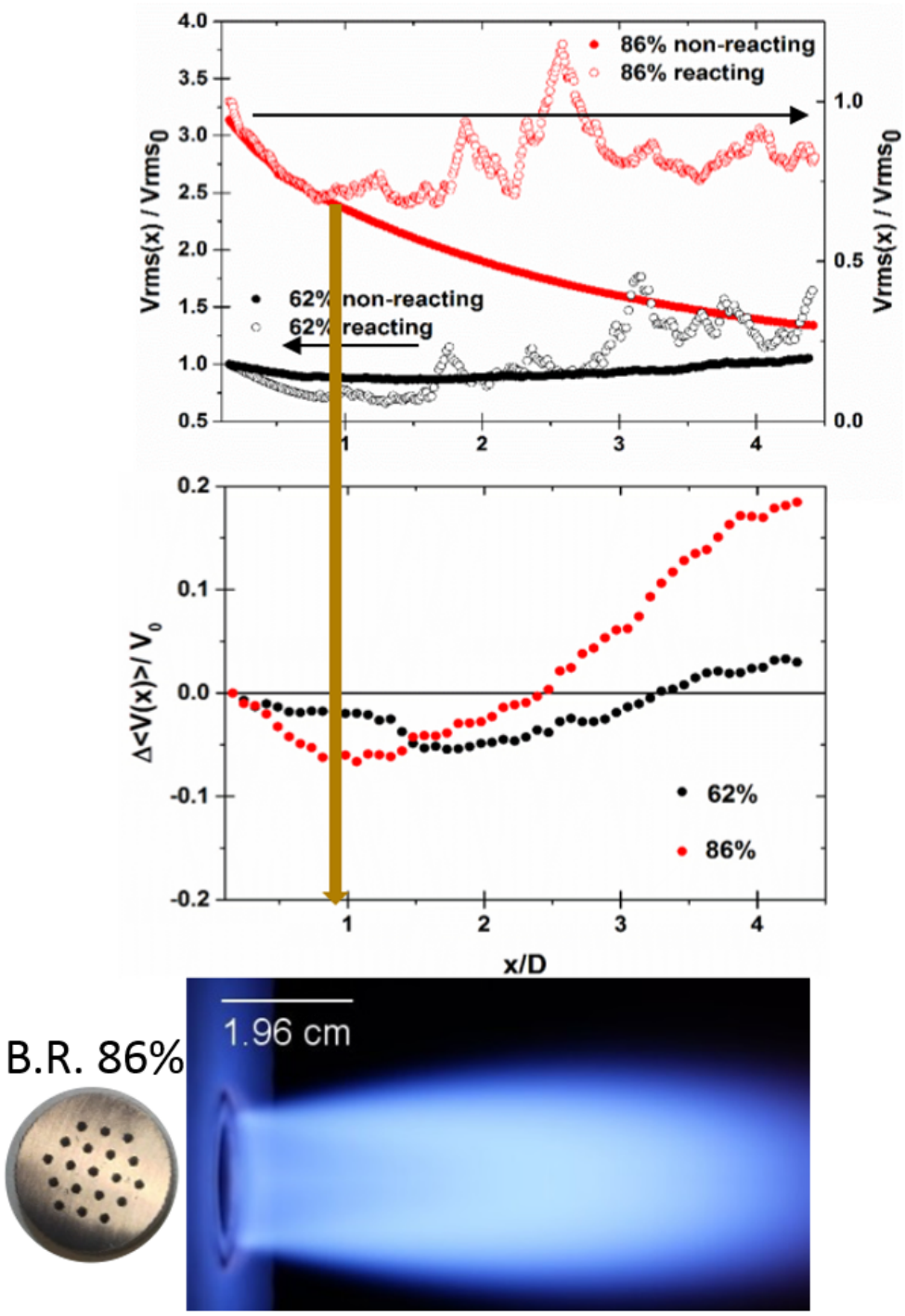

Fig. 5.15. Estimation of a height of a potential core for 86 % B.R using an axial velocity decaying along the stream-wise direction.

6. OH PLANAR LASER-INDUCED FLUORESCENCE ON TURBULENT PREMIXED FLAMES

6.1 Experimental setup

Planar laser-induced fluorescence (PLIF) using OH $Q_1(8)$ transition in the $X^2\Pi(v" = 0) \rightarrow A^2\Sigma^+(v' = 1)$ vibrational band was employed to characterize flame structures. A frequency-doubled, Q-switched Nd:YAG laser (Spectra-Physics Quanta-Ray GCR series) operates at 532 nm delivering 700 mJ per pulse at 10 Hz with a 9 ns pulse duration was used to pump a dye laser operating at 566.64 nm. The wavelength of the dye laser was measured using a High Finesse wavelength meter (WS6 Precision). Again, the wavelength was frequency-doubled using a BBO crystal to 283.32 nm in order to excite the $Q_1(8)$ transition. The OH fluorescence signal near 310 nm was collected using a Semrock interference filter (FF01-320/40-25) in combination with a UV-grade lens. A transmission of 74% at 310 nm was provided for the Semrock interference filter transmits only the OH fluorescence signal and block the scattered laser radiation at 283 nm. Furthermore, the polarization of the incoming laser was set to be orthogonal to the camera axis so that the scattered light to the camera is minimized. An intensified CCD camera (PI-MAX 4 ICCD camera, Princeton Instruments) was used to acquire OH signals. The camera system was positioned orthogonal to the direction of the laser propagation and the plane of the laser. To avoid saturated OH fluorescence, the laser power is set to 0.85 mJ per pulse. The time gate and gain of the intensified camera were adjusted to 2 s and 40. These settings give only OH fluorescence signal of 310 nm. The camera operated at 10 fps at full resolution of 1024x1024 with 16-bit image depth.

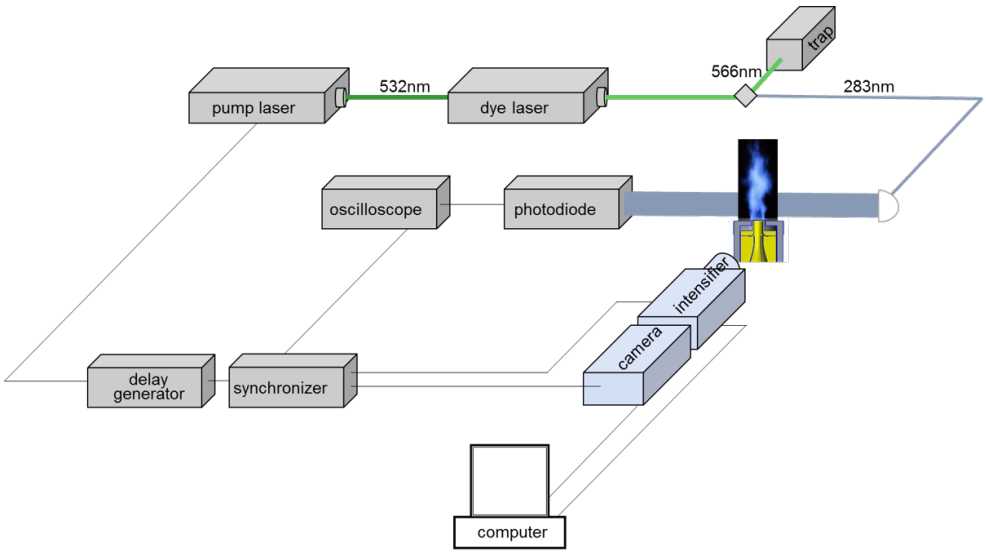

Fig. 6.1. Experimental setup of the OH PLIF system applied to characterize the structure of flames from PARAT burner.

6.2 OH PLIF data processing

To obtain high signal-to-noise of OH fluorescence, a few steps of image processing were performed. The image itself has a 16-bit depth, but it is also affected by a laser profile and absorption along the laser propagation direction. An intensity profile of the laser sheet (Fig. 6.2) was acquired from the averaged image of OH fluorescence captured at a higher location than a flame tip. A single OH fluorescence image of the constant and uniform OH concentration in the laser sheet is the most preferred condition, but it is impossible in practical conditions. Thus, the practical method to recognize the intensity profile of the laser sheet is averaging OH fluorescence images where OH molecules are uniformly distributed as much as possible, and the OH concentration is low so that there is the least effect of absorption. The location where these conditions meet is far downstream of a flame. It would be desirable that the flame is broad so that the air entrainment from the side to a flame area is minimized. Then, more uniformly distributed and unperturbed OH concentration can be achieved.

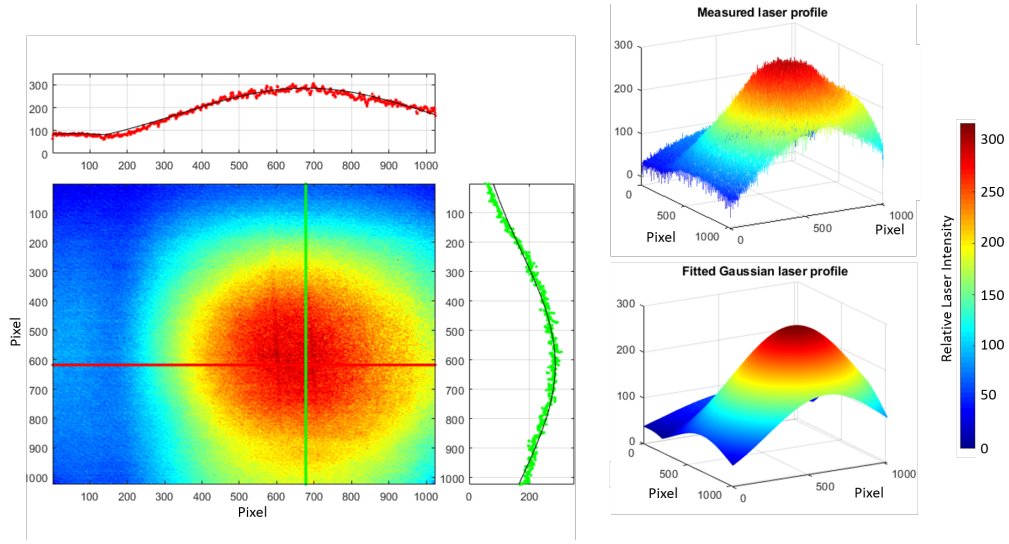

Fig. 6.2. The laser intensity profile of the sheet forming to OH PLIF. The resolution is identical for images of OH fluorescence (1024pixel x 1024pixel with 30 m per pixel).

The laser is coming from left to right in the figure and is focusing at 620 pixel (vertical) and 680 pixel (horizontal). The intensity profile of the laser sheet is a result of a combination of the laser beam profile and converging-diverging by lenses. This explains why the laser has Gaussian profile along vertical, horizontal, and azimuthal directions. The measured laser intensity profile is well fitted with Gaussian profile. The fitted profile is applied to correct the intensity of OH fluorescence. The absorption coefficient is calculated from instantaneous OH fluorescence images along horizontal direction at each vertical location.

Fig. 6.3 shows the sequence of PLIF image processing. Step 1 shows a raw image of OH PLIF. Then, the laser intensity profile of Fig. 6.2 including information about laser absorption corrected resulting in a raw image shown in Step 2. Step 3 is a binarized image to detect the reaction layer by separating the reactants and products. The blue-colored area presents the reactant, and the yellow-colored area displays the product. The blue-colored area at the lower left on the image presents pure air from the surrounding, not from the burner.

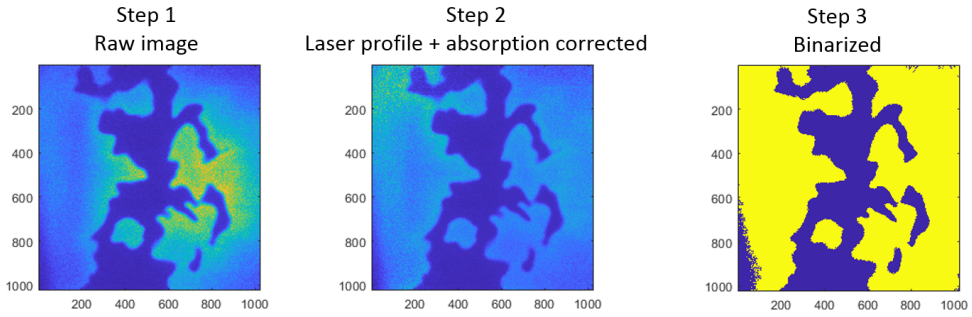

Fig. 6.3. The sequence of image processing for images of OH fluorescence.

It is difficult to quantify a number of OH molecules using PLIF, but it is desirable to detect more accurate signal for OH molecules which allows us to quantify where is flame fronts. The reason why OH PLIF images are difficult to quantify is because the number of photons collected per CCD array pixel on the flame and quenching rate in the probe volume is dependent not only the number density of OH molecules but also temperature. Thus, even if laser correction is applied, a number of OH molecules is only available after temperature profile is procured. Fortunately, the temperature dependency is less than the signal to noise ratio of OH PLIF image which allow us to quantify the location of the flame front.

6.3 Results and discussion

6.3.1 OH PLIF image

Based on the two distinct regimes, reacting flows with the conditions tabulated in Table 1 are established and compared. Primarily, Fig. 6.4 (a) shows the images for the flames with B.R. 62% and 86% with the Reynolds number 10k and equivalence ratio 0.8. The images are ensemble averaged for 12 seconds with 60 fps. The focus and exposure time are identical for the images. A white scale bar on the left side indicates the height of the inner boundary of a pure reactant core, that was determined from

the mean progress variable surface. It presents a borderline of reactant gases and intermediate product gases. It can also be interpreted as a start line of the reaction zone at the center of the flame along the streamwise direction. The blue-colored reaction zone in the flame image exists until the flame tip. This flame tip is shown as a yellow scale bar on the right side. The B.R. 62% gives a longer flame length, but the B.R. 86% gives a thicker waist of flame as well as a shorter pure reactant area.

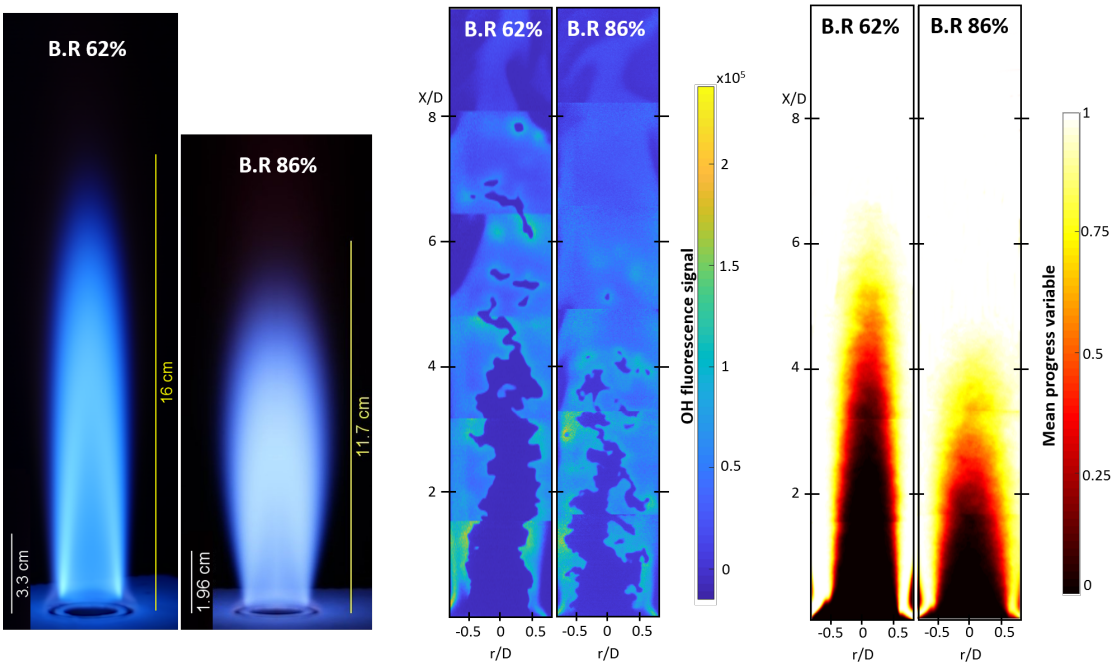

Fig. 6.4. (a) Flame image by a regular camera. (b) Instantaneous OH PLIF image. (c) Mean progress variable determined by the ensemble-averaged image of the reactant/product zones. The condition of the flames was at equivalence ratio 0.8 and Reynolds number 10,000. The image on the left side is for B.R. 62%, and the image on the right side is for B.R. 86%.

Fig. 6.4 (b) presents a representative instantaneous OH PLIF image. It is noted that this image is correlated spatially but not temporally. In agreement with the flame images, the B.R. 62% gives a more extended reactant area. The B.R. 86% generates a much shorter reactant area including more wrinkling flame front and

more unburned pockets. A contour of the mean progress variable is shown in Fig. 6.4 (c) by calculating the ensemble-averaged binarized OH PLIF image. The mean progress variable provides the same trend for the reactant area.

6.3.2 Mean progress variable

The flame structure can be compared using profiles of the mean progress variable. Fig. 6.5 presents the mean progress variable along the radial direction at $x/D < 2.75$. The location where the mean progress variable starts to increase from $< C >= 0$ is compared to discuss the burning speed. The B.R. 86% starts to burn earlier than B.R. 62% at the same axial locations. For instance, the B.R. 86% starts to burn at $r/D = 0.35$ and the B.R. 62% does at $r/D = 0.42$. The mean progress variable for B.R. 86% starts to increase at the inner radial location as compare to the case of B.R. 62% for all axial locations. The B.R. 86% has a slower burning rate which can be concluded from the lower slope of the mean progress variable along the radial direction. The lower slope corresponds to a thicker flame brush thickness. At $x/D = 2.75$, the B.R. 62% still starts from $< C >= 0$, while the B.R. 86% starts from $< C >= 0.5$.

Fig. 6.6 presents the mean progress variables along the radial direction at x/D higher than 2.75. The B.R. 86% starts to react from the mean progress variable 0.5, 0.65, 0.85 at x/D =2.75, 4, and 5 respectively, while the B.R. 62% initiates a reaction from the mean progress variable 0, 0.35, 0.62 at the same locations. At $x/D = 5.5$, the B.R. 62% starts to burn from the mean progress variable 0.81.

The flame waist, which is the maximum radial distance when a flame reaches $< C >= 1.0$, can be determined from the mean progress variable. For B.R. 62%, the flame waist is 0.70D and exists at $x/D = 4$. For B.R. 86%, the flame waist is 0.72D and exists at $x/D = 1.5$. That is, the B.R. 86% has a wider flame.

In Fig. 6.7, it is apparent that for B.R. 86%, burning starts and completes at the earlier locations than B.R. 62%. To compare these locations, $< C >= 1.0$ and 0 are

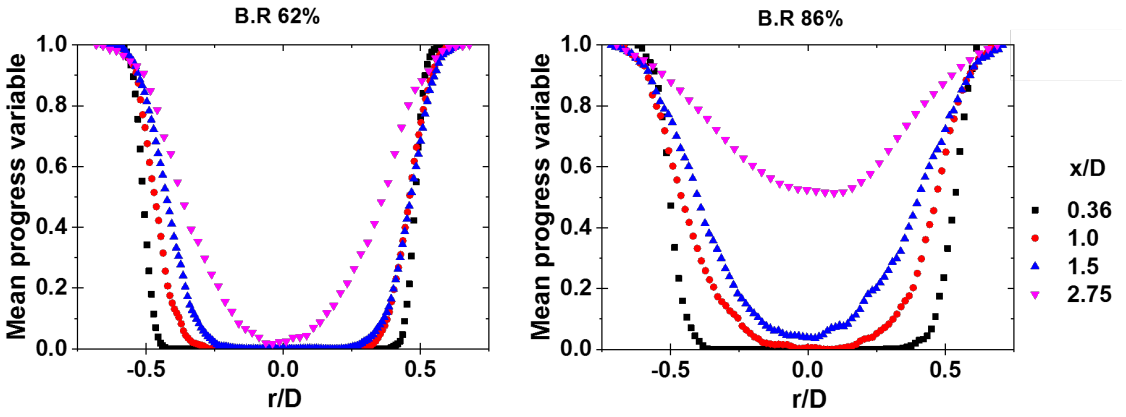

Fig. 6.5. Mean progress variable along the radial direction for B.R. 62% and B.R. 86% at $x/D < 2.75$. The condition of the flames was at equivalence ratio 0.8 and Reynolds number 10,000.

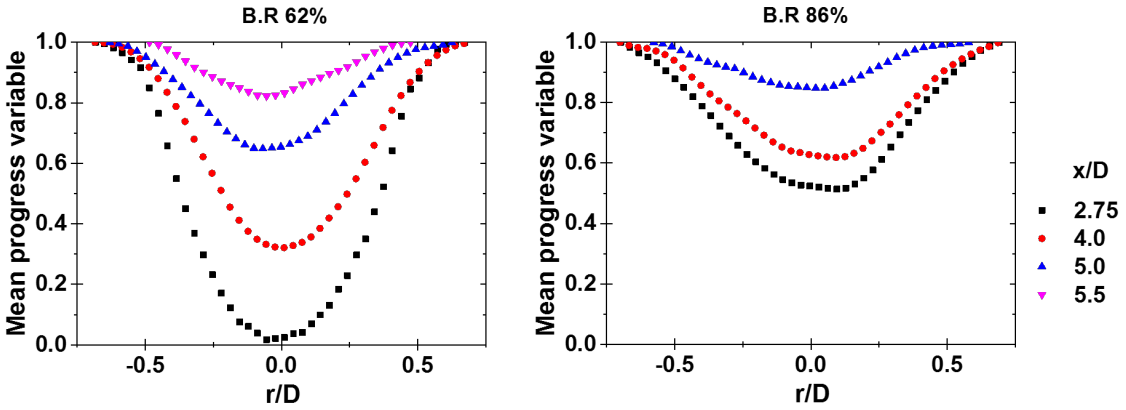

Fig. 6.6. Mean progress variable along the radial direction for B.R. 62% and B.R. 86% at $x/D > 2.75$. The condition of the flames was at equivalence ratio 0.8 and Reynolds number 10,000.

used as the leading edge and trailing edge of reaction zone. For B.R. 62%, the fuel/air mixture starts to burn at the axial location 2.1D and finishes the combustion at the axial location 7.2D. However, for B.R. 86% burning occurs from the axial location

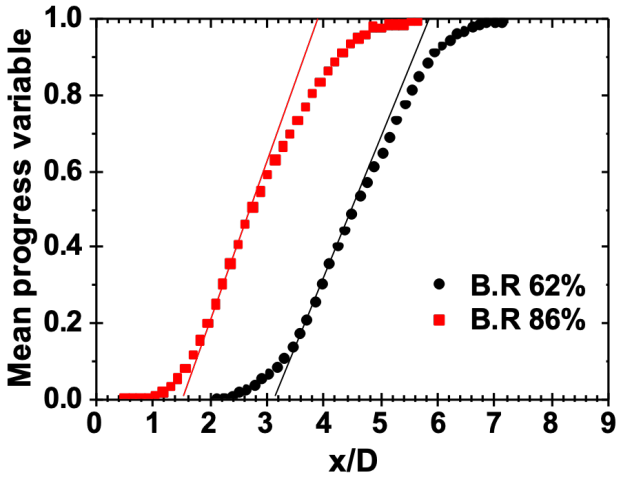

Fig. 6.7. Mean progress variable along the axial direction for B.R. 62% and B.R. 86%. The condition of the flames was at Reynolds number 10,000. The lines indicate the maximum slopes of each curve. The distance in between intersections of the slope and x-axis indicates $\delta_{t,x}$

0.5D to 5.7D. As seen from the difference between the locations, the thickness of reaction zone for the B.R. 86% is 5.2D. It is similar to the range for the B.R. 62% which is 5.1D. However, the mean flame brush thickness along the burner centerline $\delta_{t,x}$ calculated by Eqn (1) gives 2.4D for the B.R. 86% and 2.7D for the B.R. 62%. This is depicted in the figure. The lines indicate the maximum slopes of each curve. The distance in between the intersections of the slope and x-axis indicates $\delta_{t,x}$. It can be interpreted that a wider flame and a shorter mean flame brush thickness along the burner centerline $\delta_{t,x}$ occur as turbulence intensity increases [45, 48], while the thickness of reaction zone that is the distance between $< C >= 1.0$ and 0 is similar even if turbulence level increases.

6.3.3 Flame brush thickness

The turbulent flame brush thickness along the radial direction δ_t is measured based on Eqn 2.1 and compared with Eqn 2.5. Fig. 6.8, 6.9, and 6.10 present the turbulent flame brush thickness along the axial direction. Both are normalized by the burner diameter D. The B.R. 86% has a thicker flame brush than the one of 62%. A higher turbulence level does have an effect on a thicker flame brush thickness along the radial direction, which is opposite from the trend of flame brush thickness along the centerline. The significant difference can be seen when it is compared with the empirical equation Eqn 2.5. The properties used for the equation are listed in Table 1. In the case of B.R. 62%, it is well fitted by the equation. However, the B.R. 86% is not fitted with the empirical equation. Instead, it fits well when $(V(0)/V_0)^{0.6}$ is multiplied to the flame brush thickness in the empirical equation. The updated empirical equation is written as

$$\delta_T^2 = 4U_K \pi u_{rms}^2 \tau_L t \left\{ 1 - \frac{\tau_L}{t} \left[1 - \left(-\frac{t}{\tau_L} \right) \right] \right\} \tag{6.1}$$

where $U_K = (V(0)/V_0\ )^{1.2}$ is a correction factor involving $V(0)$ the streamwise velocity at the centerline and V_0 is the bulk velocity which is calculated by $\frac{Q[m^3/s]}{Exit\ area[m^2]}$. In the figure, the fitting line with uncorrected is plotted by the empirical equation Eqn 2.5, and the other line with corrected is plotted by Eqn 6.1. It can be proposed that this difference is originated from the flow regime. The increase of flame brush thickness affected by a higher turbulence level is limited, while the characteristic of the vortex-dominant flow regime significantly increases the flame brush thickness.

The empirical equation underestimates the flame brush thickness [48] at the downstream where the mean progress variable starts from nonzero. The measured flame brush thicknesses were not shown at these locations. For B.R. 62%, the locations are beyond $x/D = 3$, 4, and 5 for Reynold number 10k, 12.5k, and 15k respectively. For B.R. 86%, the locations are beyond $x/D = 4$, 5, and 6 for Reynold number 10k, 12.5k, and 15k respectively.

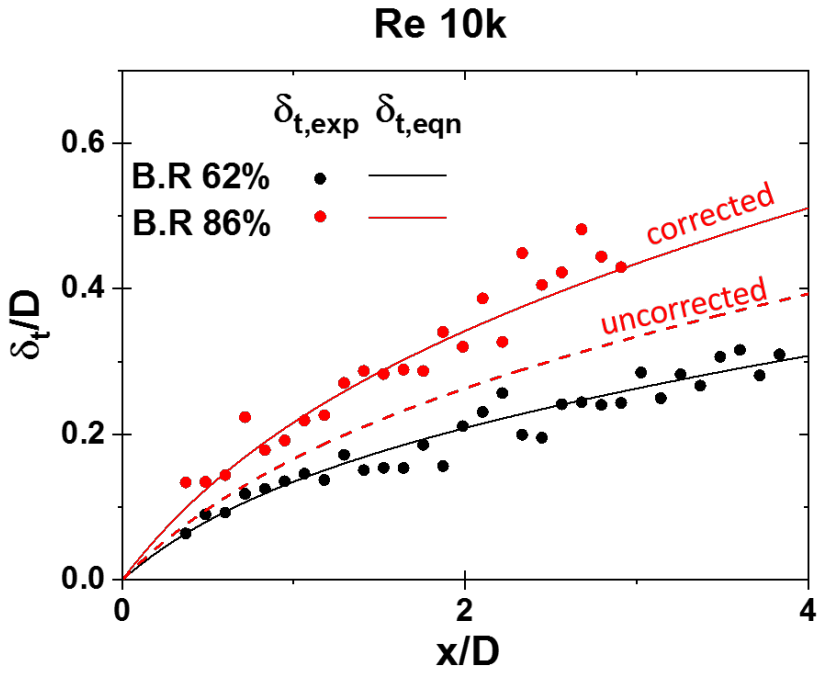

Fig. 6.8. Flame brush thickness normalized by the burner diameter along the axial direction normalized by the burner diameter. Reynolds number is 10,000. The empirical equation of flame brush thickness for the B.R. 86% requires a correction to fit with the experimental flame brush thickness, whereas the B.R. 62% does not.

6.3.4 Flame surface density

Fig. 6.11 provides the flame surface density (FSD) vs. the mean progress variable for the Reynolds number 10k. It is calculated over a flame. The B.R. 62% has several points for flame surface density beyond 0.15 mm^{-1} apart from the mainstream. Except these scattered points, the B.R. 86% has more distributed flame surface density than the B.R. 62%. This distribution is getting wider toward $< C >= 0.5$ along the mean progress variable. Meanwhile, the B.R. 62% has relatively constant distribution except the scattered points. The wider distribution may be because of the higher degree of flamelet wrinkling near $< C >= 0.5$ for the B.R. 86%. On the other hand, lesser wrinkling of flamelet leads to thin and constant distribution of flame surface

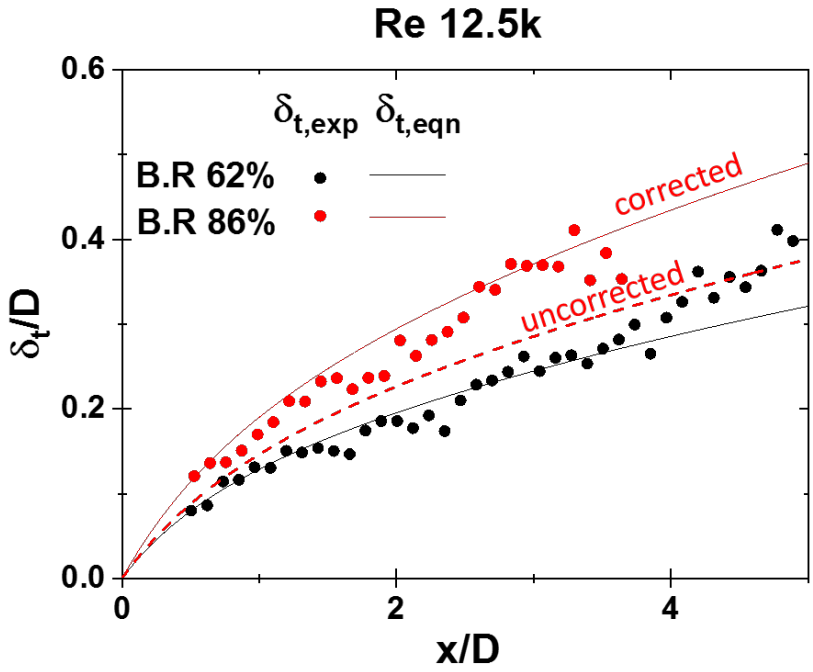

Fig. 6.9. Flame brush thickness normalized by the burner diameter along the axial direction normalized by the burner diameter. Reynolds number is 12,500. The empirical equation of flame brush thickness for the B.R. 86% requires a correction to fit with the experimental flame brush thickness, whereas the B.R. 62% does not.

density. The scattered points may come from the locations where certain parts of the flamelet remain unperturbed even if the flamelet fluctuates.

The mean flame surface density vs. the mean progress variable for the entire flame is shown in Fig. 6.12, 6.13, and 6.14. The mean flame surface density vs. the mean progress variable for $0.4 < x/D < 2$ is shown in Fig. 6.15, 6.16, and 6.17.They are for Reynolds number = 10,000, 12,500, and 15,000. Below $x/D = 0.4$ is not included due to the effect of the pilot flame. The mean flame surface density for the entire flame shows that the B.R. 86% has higher values at all mean progress variables. However, it is opposite at the upstream of the flame. That is, the B.R. 62% is higher. In addition, the maximum flame surface density for the B.R. 62% decreases from 0.21

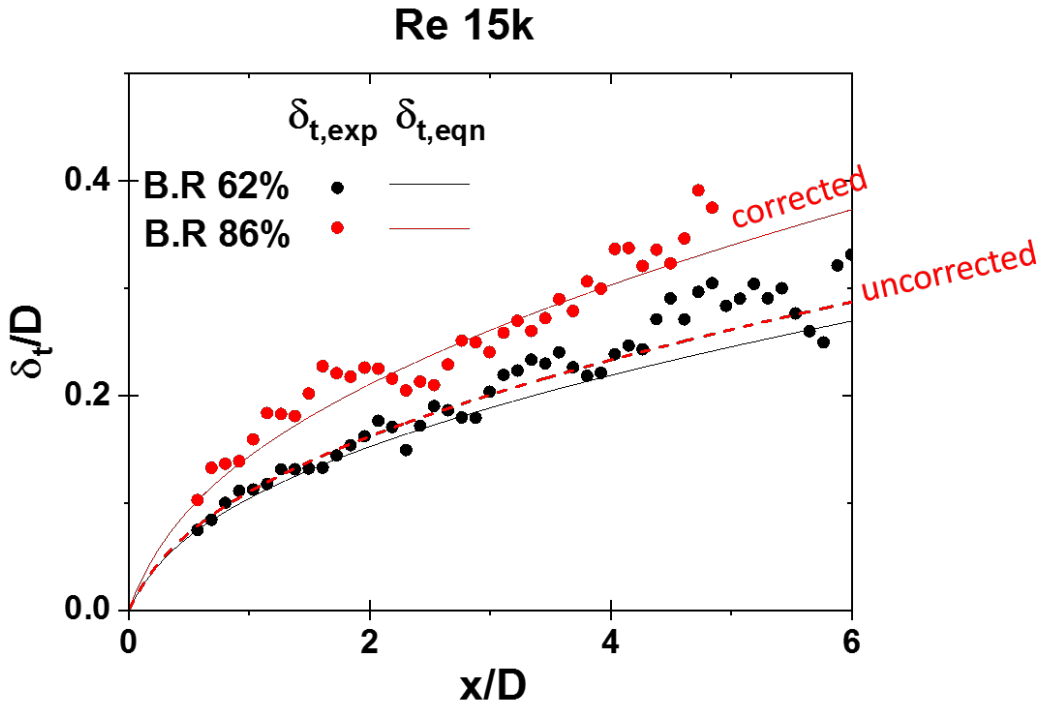

Fig. 6.10. Flame brush thickness normalized by the burner diameter along the axial direction normalized by the burner diameter. Reynolds number is 15,000. The empirical equation of flame brush thickness for the B.R. 86% requires a correction to fit with the experimental flame brush thickness, whereas the B.R. 62% does not.

at the upstream to 0.13 for the entire flame, whereas the maximum flame surface density for the B.R. 86% shows a relatively less change from 0.17 to 0.13. It can be inferred that the B.R. 62% generates a drastic drop of flame surface density along the flame axis and the B.R. 86% generates a relatively constant flame surface density along the flame axis. The vortex-dominant flow regime would cause the difference. Higher turbulence existing in the vortex-zone is not consumed easily and retains its strength until flame tip, then generates a high level of flamelet wrinkling resulting in a relatively constant flame surface density. Low turbulence originated from a low B.R. may generate greater flame surface density at the upstream, but the low turbulence

gets consumed in a short distance. Then, a level of flamelet wrinkling relies on the turbulence originated from the interference between flow and the surroundings.

The maximum mean flame surface density for the entire flame is decreasing as Reynolds number increases, while the maximum mean flame surface density for $0.4 < x/D < 2$ is increasing as Reynolds number increases.

Fig. 6.18, 6.19,and 6.20 shows the flame surface density along the centerline. The B.R. 86% makes a sharper and higher flame surface density profile than B.R. 62%. The existence of the vortex-zone resulting in higher turbulence could produce the higher flame surface density profile.

6.3.5 Global consumption speed

The global consumption speed $S_{T,GC} = \frac{\dot{m}_R}{\rho_R A_{<C>}}$ at $< C >= 0.05$ was calculated and is shown in Fig. 6.21. The unperturbed laminar flame speed $S_L^o = 0.32$m/s was calculated using CHEMKIN with the GRI 3.0 mechanism. The global consumption speed for Re 10k gives 1.45 m/s for B.R. 62% and 2.33 m/s for B.R. 86%. It implies that B.R. 62% has a greater area of $< C >= 0.05$ with the constant mass flow rate of reactants $\dot{m}_R$ and density of reactants ρ_R. A thicker flame brush is interpreted as a lower consumption speed. The combined effects of the thickened flame brush along the radial direction and the shrunk flame brush along the centerline result in a thinner flame brush per flame. While the global consumption speed increases with turbulence fluctuation at a constant Reynolds number, it decreases with increasing turbulence fluctuation by increasing Reynolds number. The trend of consumption speed or turbulent burning velocity has been reported for both cases: it increases as turbulence fluctuation is rising [43, 45] but starts to decrease at a certain point [12].

The existence of the vortex-zone in turbulent flow has as an important role when the global consumption speed is compared at the same turbulence fluctuation. For instance, $u\prime/S_L^o = 9$ gives , $S_{T,GC}/S_L^o = 4$ for B.R. 62% and $S_{T,GC}/S_L^o = 12$ for B.R.

86%. It can be suggested that the vortex-zone in turbulent flow at the same velocity fluctuation level improves the consumption speed.

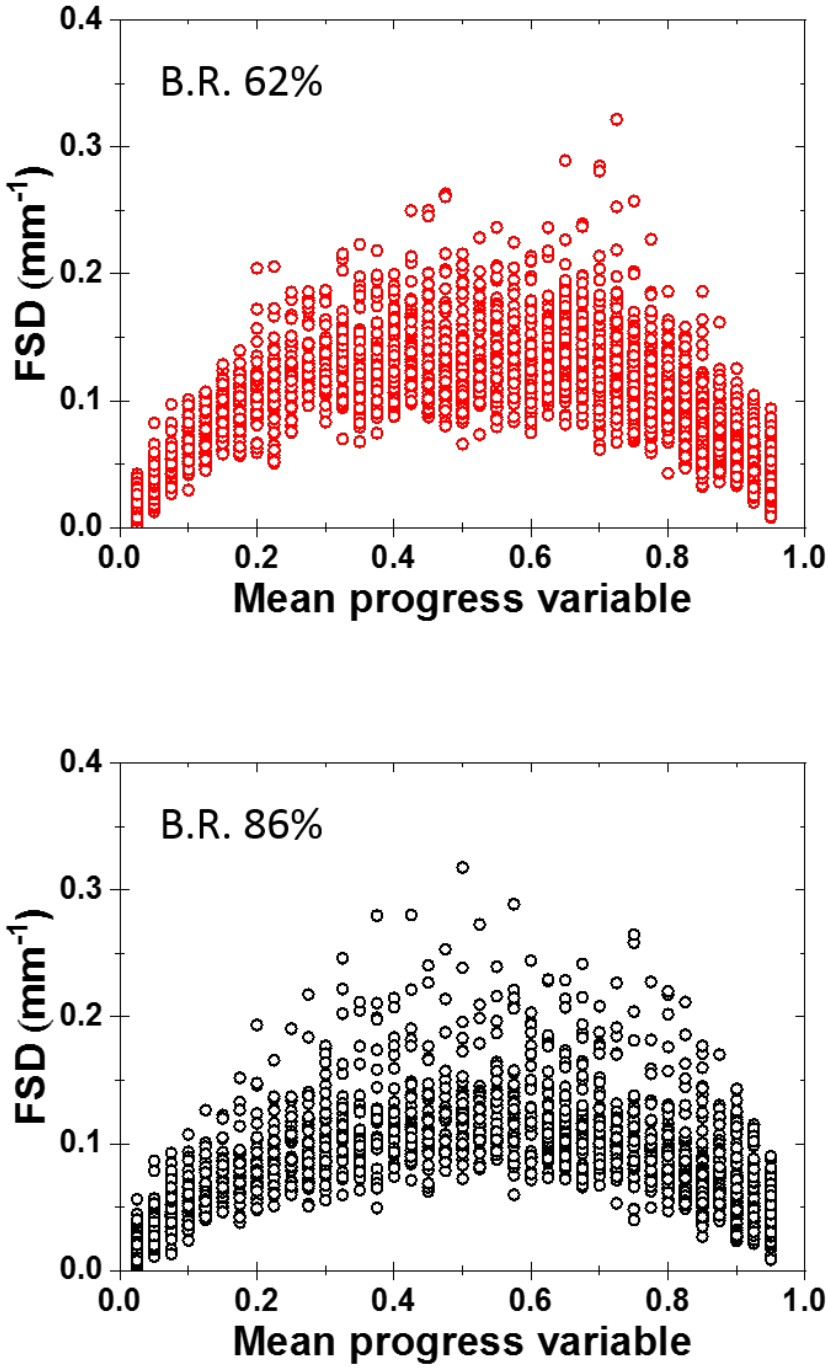

Fig. 6.11. Flame surface density vs. the mean progress variable for Reynolds number = 10000.

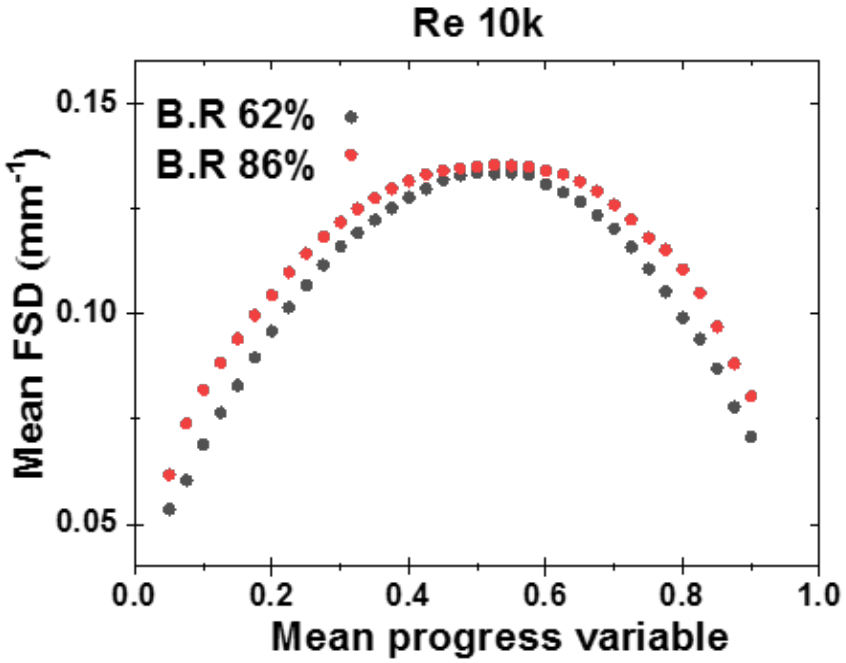

Fig. 6.12. Mean flame surface density vs. the mean progress variable for the entire flame. Reynolds number = 10,000.

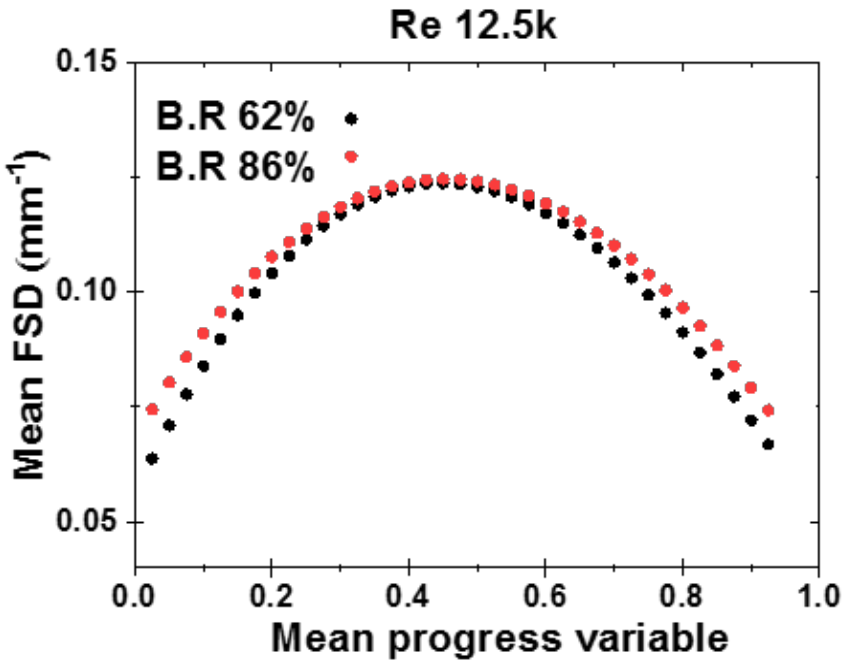

Fig. 6.13. Mean flame surface density vs. the mean progress variable for the entire flame. Reynolds number = 12,500.

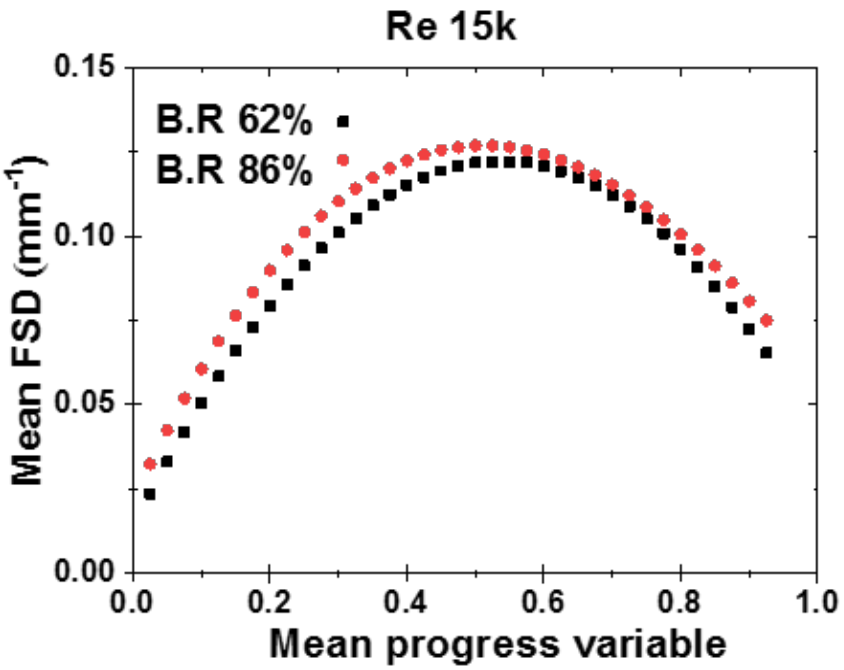

Fig. 6.14. Mean flame surface density vs. the mean progress variable for the entire flame. Reynolds number = 15,000.

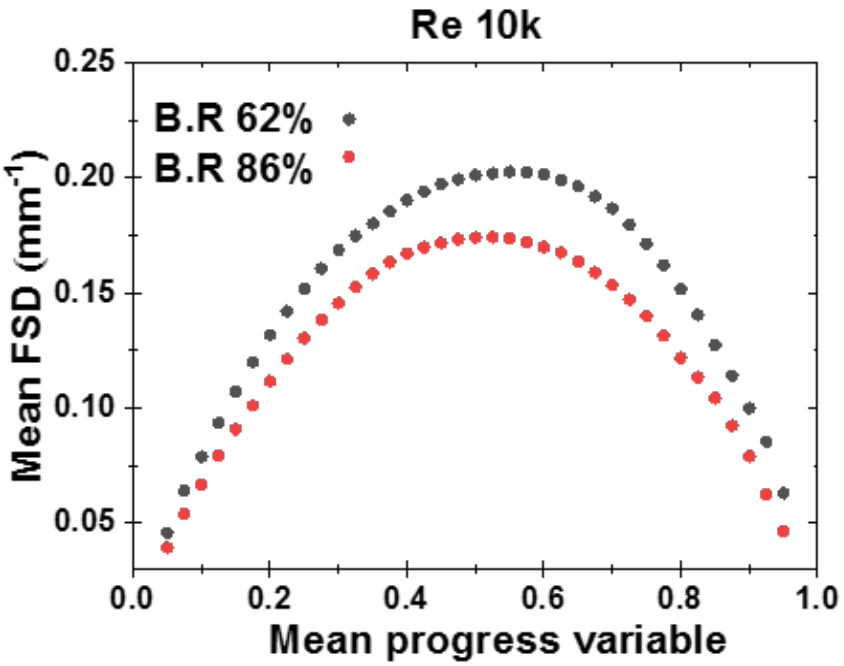

Fig. 6.15. Mean flame surface density vs. the mean progress variable for $0.4 < x/D < 2$. Reynolds number = 10,000.

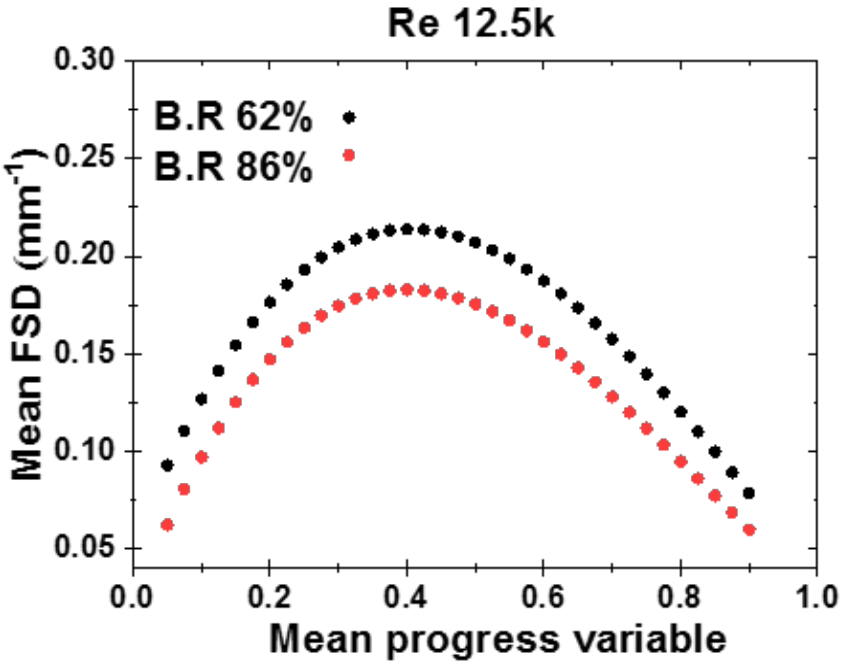

Fig. 6.16. Mean flame surface density vs. the mean progress variable for $0.4 < x/D < 2$. Reynolds number = 12,500.

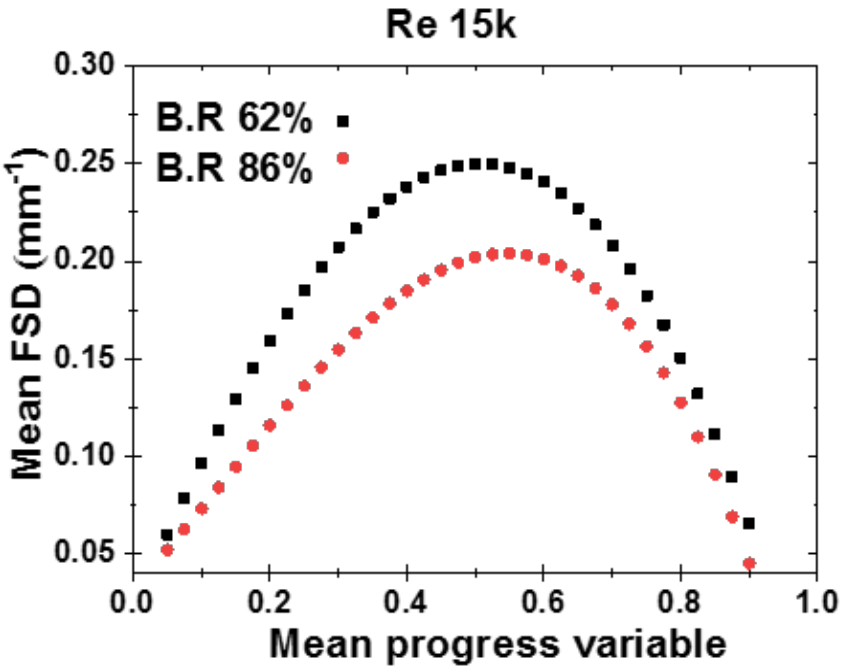

Fig. 6.17. Mean flame surface density vs. the mean progress variable for $0.4 < x/D < 2$. Reynolds number = 15,000.

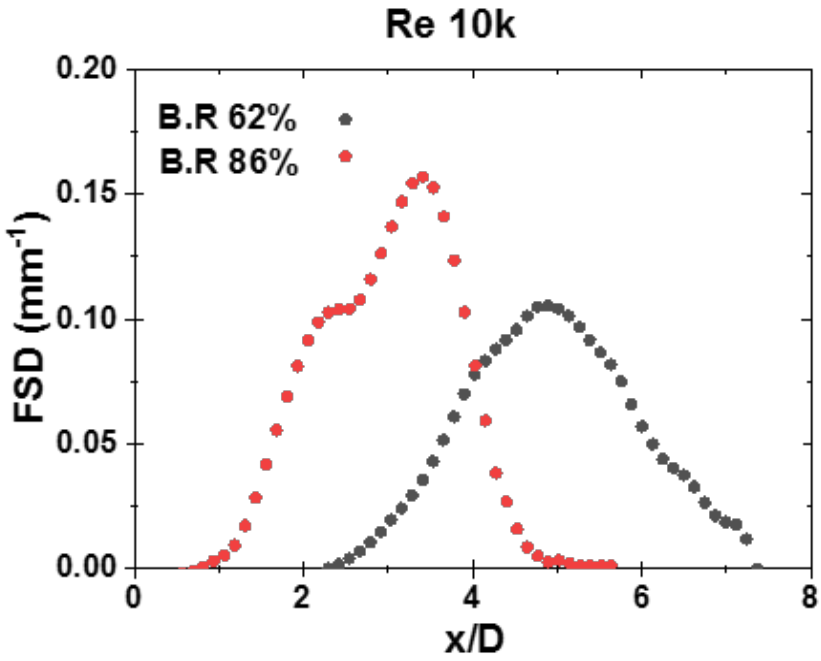

Fig. 6.18. Flame surface density along the centerline. Reynolds number = 10,000.

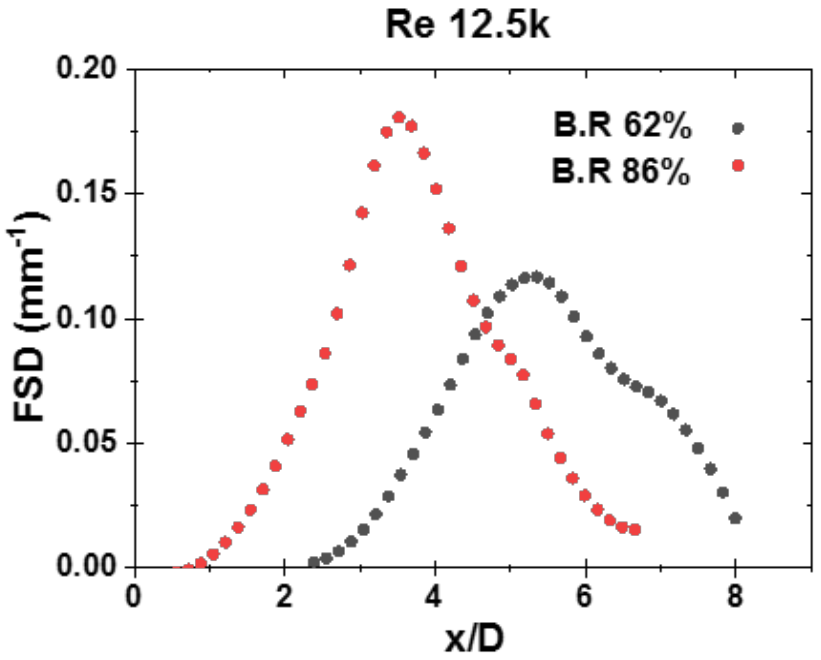

Fig. 6.19. Flame surface density along the centerline. Reynolds number = 12,500.

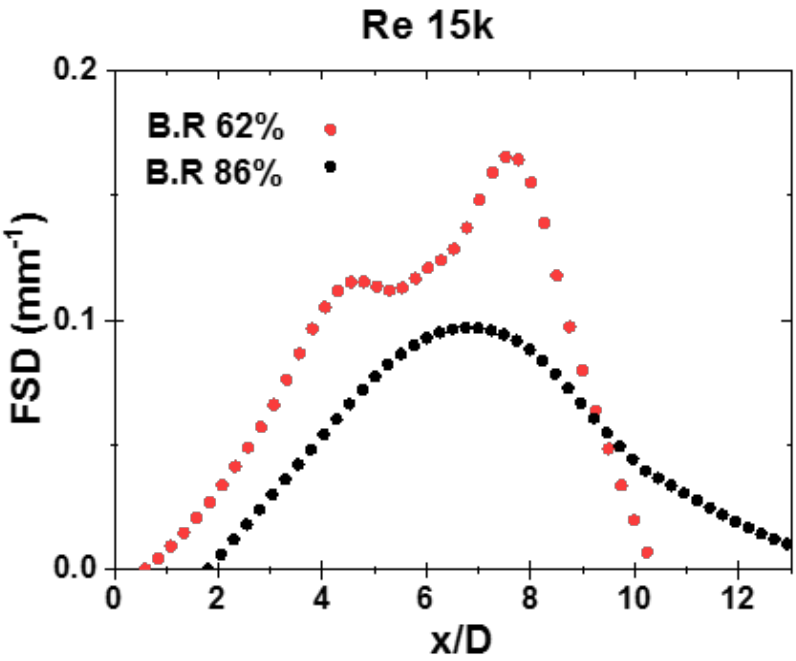

Fig. 6.20. Flame surface density along the centerline. Reynolds number = 15,000.

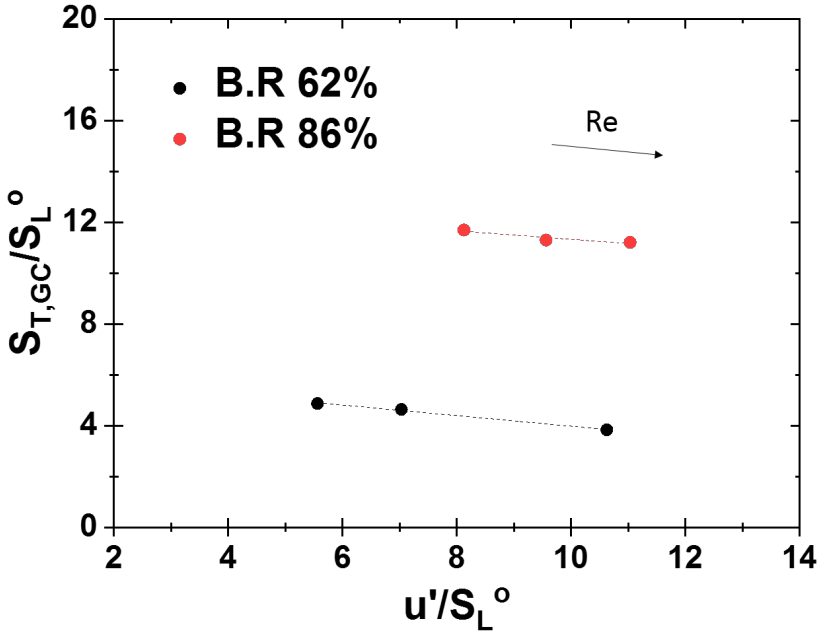

Fig. 6.21. Global consumption speed versus turbulence fluctuation normalized by the unperturbed laminar flame speed.

7. CONCLUSION

In regards to the next generation of gas turbine, which are lean premixed pre-vaporised combustors and axial staged lean-mixture injection, fundamental study about lean turbulent premixed flames was performed. In the condition, flame stabilization is essential and significant for good performance and low NOx combustion. The flame stabilization is accomplished by recirculation. The hot recirculating gases transfer heat to the colder ones ignite those and initiate flame spread. The burned gases carry heat to the recirculation zone to balance the heat lost in igniting the combustible gas. Adequate energy must be supplied to the stabilization zone to continuous ignition on the incoming gas flow. For the recirculation, this study selected to use perforated plate among various turbulence generators because of its popularity. There is a significant factor to select a geometry of perforated plate. That is a blockage ratio. Flow with a perforate plate has a blockage ratio (B.R.) 0-70% generates the stream-dominant turbulent flow, and flow with a perforated plate has a B.R. 80-99% develops the vortex-dominant turbulent flow. In this study, B.R. 62% represents the flow in the stream-dominant turbulence regime, while B.R. 86% represents the flow in the vortex-dominant turbulence regime.

In order to examine the effects of turbulent flow regime on the flame structure, a premixed axisymmetric reactor assisted turbulence burner was newly developed. The experimental apparatus allows a study of the effects of blockage ratio of perforated plate successfully because the burner provides the fully-developed turbulent flow if no perforated plate is installed. Based on the fully-developed turbulent flow, the characteristics of a turbulent flow varied by the different blockage ratio of perforated plate can be examined. Furthermore, the burner has a capability of high-pressure and high-temperature test conditions.

Using the newly designed burner and the two perforated plates with B.R 62% and 86% respectively, the effects of turbulent flow regime on the flame structure was experimentally investigated. We performed analysis of visible image, stereo particle image velocity, and OH planar laser-induced fluorescence measurements. Methane/air mixture was used for the main flame, and hydrogen was used for the pilot flame.

They show entirely different profiles of velocity. The stream-dominant turbulent flow has a top-hat flow profile along the radial direction, but the vortex-dominant turbulent flow has a sharp cone in the center in addition to a top-hat flow profile. Also, the stream-dominant turbulent flow has a low level of turbulence which gets consumed over a short distance, whereas the vortex-dominant turbulent flow provides a high level of turbulence which cannot be consumed over a short distance and hence it is transferred to the far downstream at least until 4.5D. In detail, it was observed that (1) the different streamwise velocity profiles at exit, (2) the different streamwise velocity profiles are converged to the same velocity profile as approaching to x/D = 4, and (3) locally isotropic turbulent fluctuation based on the same magnitude of rms velocities u_{rms}, v_{rms}, and w_{rms}. Turbulent intensity V_{rms}/V_{mean} of B.R 62% is ranged from 16.5 to 20.7%. With a higher B.R, turbulent intensity increases to the range from 18.1 to 24.1%. Mean and rms streamwise velocities increase with a higher B.R. As Reynolds number increases, both B.R 62% and 86% generate higher mean and rms streamwise velocities. At the exit, 86% B.R has a broaden width of PDFs compared to 62% B.R resulting in higher rms velocity. But, as approaching to x/D=4, the shape (the width and height) of PDF is getting equal. The ratio of decay of mean streamwise velocity for B.R 86% is 40% at x/D=4, but B.R 62% makes 10%. B.R 86% keeps decaying rms velocity until 55% of the initial value. In contrast, B.R 62% makes decaying velocity until 85% and recovering to the initial one. The gap of decays between non-reacting and reacting flows is caused by turbulence generated by flame. The gap between two cases can lead to estimation of a height of potential core. These three estimations through visible images, PIV, and CARS are in the good agreement.

Significantly different flames are observed based on flame height, height of pure reactant core, the mean progress variable, flame brush thickness, flame surface density, and consumption speed. Flames with the stream-dominant flow only show the flame structure originated from turbulence. On the other hand, flames with the vortex-dominant flow show the flame structure originated from turbulence and the effects of the vortex-dominant turbulent flow. The effects of turbulence are (1) higher turbulence produces a wider and shorter flame and (2) higher turbulence generates a bigger horizontal flame brush thickness and a smaller longitudinal flame brush thickness. The effects of vortex-dominant turbulent flow can be described into three. First, the vortex-dominant turbulent flow regime makes the horizontal flame brush thickness much larger than what it is expected by the turbulence diffusion theory [53]. This disagreement can be corrected by multiplying a correction factor $U_K = (V(0)/V_0\ )^{1.2}$ where $V(0)$ is the streamwise velocity at the centerline and V_0 is the bulk velocity which is calculated by $\frac{Q[m^3/s]}{Exit\ area[m^2]}$. Second, the vortex-dominant turbulent flow shows 47% decreasing of mean flame surface density along the streamwise direction, while the stream-dominant turbulent flow forms 77% drop of mean flame surface density along the streamwise direction. Thus, the vortex-dominant turbulent flow has a lesser change in mean flame surface density. Third, the vortex-dominant turbulent flow increases the consumption speed by 300% in comparison to the stream-dominant turbulent flow with the same velocity fluctuation level.

Flow with a perforate plate has a blockage ratio (B.R.) 0-70% generates the stream-dominant turbulent flow, and flow with a perforated plate has a B.R. 80-99% develops the vortex-dominant turbulent flow. In this study, B.R. 62% represents the flow in the stream-dominant turbulence regime, while B.R. 86% represents the flow in the vortex-dominant turbulence regime.

This is a significant practical result for combustor designer interested in utilizing a perforated plate. They have to consider a B.R. of perforated plate. To emphasize the two distinct flow regime, I would like to duplicate the sentence. Flow with a perforate plate has a blockage ratio (B.R.) 0-70% generates the stream-dominant

turbulent flow, and flow with a perforated plate has a B.R. 80-99% develops the vortex-dominant turbulent flow.

REFERENCES

REFERENCES

[1] A. Mazas, D. Lacoste, and T. Schuller, "Experimental and numerical investigation on the laminar flame speed of ch4/o2 mixtures diluted with co2 and h2o," in *ASME Turbo Expo 2010: Power for Land, Sea, and Air*. American Society of Mechanical Engineers, 2010, pp. 411–421.

[2] H. K. Kim, Y. Kim, S. M. Lee, and K. Y. Ahn, "No reduction in 0.03–0.2 mw oxy-fuel combustor using flue gas recirculation technology," *Proceedings of the combustion institute*, vol. 31, no. 2, pp. 3377–3384, 2007.

[3] Z. Chen, X. Qin, B. Xu, Y. Ju, and F. Liu, "Studies of radiation absorption on flame speed and flammability limit of co2 diluted methane flames at elevated pressures," *Proceedings of the Combustion Institute*, vol. 31, no. 2, pp. 2693–2700, 2007.

[4] D. Han, A. Satija, J. P. Gore, and R. P. Lucht, "Experimental study of co 2 diluted, piloted, turbulent ch 4/air premixed flames using high-repetition-rate oh plif," *Combustion and Flame*, vol. 193, pp. 145–156, 2018.

[5] T. Lieuwen and K. McManus, "Introduction: combustion dynamics in lean-premixed prevaporized (lpp) gas turbines," *Journal of Propulsion and Power*, vol. 19, no. 5, pp. 721–721, 2003.

[6] S. K. Dhanuka, J. E. Temme, J. F. Driscoll, and H. C. Mongia, "Vortex-shedding and mixing layer effects on periodic flashback in a lean premixed prevaporized gas turbine combustor," *Proceedings of the Combustion Institute*, vol. 32, no. 2, pp. 2901–2908, 2009.

[7] J. E. Temme, P. M. Allison, and J. F. Driscoll, "Combustion instability of a lean premixed prevaporized gas turbine combustor studied using phase-averaged piv," *Combustion and Flame*, vol. 161, no. 4, pp. 958–970, 2014.

[8] T. Yamamoto, K. Shimodaira, S. Yoshida, and Y. Kurosawa, "Emission reduction of fuel-staged aircraft engine combustor using an additional premixed fuel nozzle," *Journal of engineering for gas turbines and power*, vol. 135, no. 3, p. 031502, 2013.

[9] T. Saitoh, T. Nakasu, T. Hiroi, H. Yamada, and S. Hayashi, "Emissions characteristics of combustion of lean secondary premixed gas jets injected into burned gas from primary stage by lean premixed combustion supported by reverse jet flame holding," in *ASME Turbo Expo 2016: Turbomachinery Technical Conference and Exposition*. American Society of Mechanical Engineers, 2016, pp. V04AT04A047–V04AT04A047.

[10] S. Adachi, A. Iwamoto, S. Hayashi, H. Yamada, and S. Kaneko, "Emissions in combustion of lean methane-air and biomass-air mixtures supported by primary hot burned gas in a multi-stage gas turbine combustor," *Proceedings of the Combustion Institute*, vol. 31, no. 2, pp. 3131–3138, 2007.

[11] S. R. Turns *et al.*, *An introduction to combustion*. McGraw-hill New York, 1996, vol. 499.

[12] A. Lipatnikov, *Fundamentals of premixed turbulent combustion*. CRC Press, 2013.

[13] N. Swaminathan and K. N. C. Bray, *Turbulent premixed flames*. Cambridge University Press, 2011.

[14] C. K. Law, *Combustion physics*. Cambridge university press, 2010.

[15] T. Poinsot and D. Veynante, *Theoretical and numerical combustion*. RT Edwards, Inc., 2005.

[16] V. Katre and S. Bhele, "A review of laminar burning velocity of gases and liquid fuels," *International Journal of Computational Engineering Research. Vol*, vol. 3, pp. 33–38, 2013.

[17] B. R. Chowdhury and B. M. Cetegen, "Effects of free stream flow turbulence on blowoff characteristics of bluff-body stabilized premixed flames," *Combustion and Flame*, vol. 190, pp. 302–316, 2018.

[18] ——, "Experimental study of the effects of free stream turbulence on characteristics and flame structure of bluff-body stabilized conical lean premixed flames," *Combustion and Flame*, vol. 178, pp. 311–328, 2017.

[19] A. Fan, J. Wan, Y. Liu, B. Pi, H. Yao, and W. Liu, "Effect of bluff body shape on the blow-off limit of hydrogen/air flame in a planar micro-combustor," *Applied Thermal Engineering*, vol. 62, no. 1, pp. 13–19, 2014.

[20] J. Wan, A. Fan, Y. Liu, H. Yao, W. Liu, X. Gou, and D. Zhao, "Experimental investigation and numerical analysis on flame stabilization of ch4/air mixture in a mesoscale channel with wall cavities," *Combustion and Flame*, vol. 162, no. 4, pp. 1035–1045, 2015.

[21] D. Michaels and A. F. Ghoniem, "Impact of the bluff-body material on the flame leading edge structure and flame–flow interaction of premixed ch4/air flames," *Combustion and Flame*, vol. 172, pp. 62–78, 2016.

[22] F. Proch, P. Domingo, L. Vervisch, and A. M. Kempf, "Flame resolved simulation of a turbulent premixed bluff-body burner experiment. part i: Analysis of the reaction zone dynamics with tabulated chemistry," *Combustion and Flame*, vol. 180, pp. 321–339, 2017.

[23] K. S. Kedia and A. F. Ghoniem, "The blow-off mechanism of a bluff-body stabilized laminar premixed flame," *Combustion and Flame*, vol. 162, no. 4, pp. 1304–1315, 2015.

[24] M. Stöhr, C. M. Arndt, and W. Meier, "Transient effects of fuel–air mixing in a partially-premixed turbulent swirl flame," *Proceedings of the Combustion Institute*, vol. 35, no. 3, pp. 3327–3335, 2015.

[25] A. Marshall, J. Lundrigan, P. Venkateswaran, J. Seitzman, and T. Lieuwen, "Measurements of stretch statistics at flame leading points for high hydrogen content fuels," *Journal of Engineering for Gas Turbines and Power*, vol. 139, no. 11, p. 111503, 2017.

[26] R. Cheng, D. Littlejohn, W. A. Nazeer, and K. Smith, "Laboratory studies of the flow field characteristics of low-swirl injectors for adaptation to fuel-flexible turbines," *Journal of Engineering for Gas Turbines and Power*, vol. 130, no. 2, p. 021501, 2008.

[27] C. Chan, K. Lau, W. Chin, and R. Cheng, "Freely propagating open premixed turbulent flames stabilized by swirl," in *Symposium (International) on Combustion*, vol. 24, no. 1. Elsevier, 1992, pp. 511–518.

[28] R. Cheng, "Velocity and scalar characteristics of premixed turbulent flames stabilized by weak swirl," *Combustion and flame*, vol. 101, no. 1-2, pp. 1–14, 1995.

[29] F. M. Berger, T. Hummel, M. Hertweck, J. Kaufmann, B. Schuermans, and T. Sattelmayer, "High-frequency thermoacoustic modulation mechanisms in swirl-stabilized gas turbine combustorspart i: Experimental investigation of local flame response," *Journal of Engineering for Gas Turbines and Power*, vol. 139, no. 7, p. 071501, 2017.

[30] M. Summerfield, "The structure and propagation mechanism of turbulent flames in high speed flow," *Journal of Jet Propulsion*, vol. 25, no. 8, pp. 377–384, 1955.

[31] S. Kheirkhah and Ö. L. Gülder, "Consumption speed and burning velocity in counter-gradient and gradient diffusion regimes of turbulent premixed combustion," *Combustion and Flame*, vol. 162, no. 4, pp. 1422–1439, 2015.

[32] A. W. Skiba, T. M. Wabel, J. Temme, and J. F. Driscoll, "Experimental Assessment of Premixed Flames Subjected to Extreme Turbulence," *54th AIAA Aerospace Sciences Meeting*, no. January, pp. 1–26, 2016.

[33] B. Sundaram, A. Y. Klimenko, M. J. Cleary, and U. Maas, "Prediction of NOx in premixed high-pressure lean methane flames with a MMC-partially stirred reactor," *Proceedings of the Combustion Institute*, vol. 35, no. 2, pp. 1517–1525, 2015.

[34] R. Fragner, F. Halter, N. Mazellier, C. Chauveau, and I. Gökalp, "Investigation of pressure effects on the small scale wrinkling of turbulent premixed bunsen flames," *Proceedings of the Combustion Institute*, vol. 35, no. 2, pp. 1527–1535, 2015.

[35] S. H. Won, B. Windom, B. Jiang, and Y. Ju, "The role of low temperature fuel chemistry on turbulent flame propagation," *Combustion and Flame*, vol. 161, no. 2, pp. 475–483, 2014.

[36] P. Venkateswaran, A. Marshall, D. H. Shin, D. Noble, J. Seitzman, and T. Lieuwen, "Measurements and analysis of turbulent consumption speeds of h2/co mixtures," *Combustion and Flame*, vol. 158, no. 8, pp. 1602–1614, 2011.

[37] P. Venkateswaran, A. Marshall, J. Seitzman, and T. Lieuwen, "Pressure and fuel effects on turbulent consumption speeds of h2/co blends," *Proceedings of the Combustion Institute*, vol. 34, no. 1, pp. 1527–1535, 2013.

[38] G. Damköhler, "The effect of turbulence on the flame velocity in gas mixtures," 1947.

[39] J. F. Driscoll, "Turbulent premixed combustion: Flamelet structure and its effect on turbulent burning velocities," *Progress in Energy and Combustion Science*, vol. 34, no. 1, pp. 91–134, 2008.

[40] A. W. Skiba, C. D. Carter, S. D. Hammack, and T. Lee, "A simplified approach to simultaneous multi-scalar imaging in turbulent flames," *Combustion and Flame*, vol. 189, pp. 207–211, 2018.

[41] F. Gouldin and P. Miles, "Chemical closure and burning rates in premixed turbulent flames," *Combustion and Flame*, vol. 100, no. 1-2, pp. 202–210, 1995.

[42] G. G. Lee, K. Y. Huh, and H. Kobayashi, "Measurement and analysis of flame surface density for turbulent premixed combustion on a nozzle-type burner," *Combustion and flame*, vol. 122, no. 1-2, pp. 43–57, 2000.

[43] P. Griebel, P. Siewert, and P. Jansohn, "Flame characteristics of turbulent lean premixed methane/air flames at high pressure: Turbulent flame speed and flame brush thickness," *Proceedings of the Combustion Institute*, vol. 31, no. 2, pp. 3083–3090, 2007.

[44] P. Venkateswaran, "Measurements and modeling of turbulent consumption speeds of syngas fuel blends," Ph.D. dissertation, Georgia Institute of Technology, 2013.

[45] P. Tamadonfar and Ö. L. Gülder, "Flame brush characteristics and burning velocities of premixed turbulent methane/air bunsen flames," *Combustion and Flame*, vol. 161, no. 12, pp. 3154–3165, 2014.

[46] M. Namazian, I. Shepherd, and L. Talbot, "Characterization of the density fluctuations in turbulent v-shaped premixed flames," *Combustion and flame*, vol. 64, no. 3, pp. 299–308, 1986.

[47] A. Boukhalfa and I. Gökalp, "Influence of the damköhler number on the average thickness of conical turbulent premixed methane/air flames," *Combustion and flame*, vol. 73, no. 1, pp. 75–87, 1988.

[48] A. Lipatnikov and J. Chomiak, "Turbulent flame speed and thickness: phenomenology, evaluation, and application in multi-dimensional simulations," *Progress in energy and combustion science*, vol. 28, no. 1, pp. 1–74, 2002.

[49] B. Renou, A. Mura, E. Samson, and A. Boukhalfa, "Characterization of the local flame structure and the flame surface density for freely propagating premixed flames at various lewis numbers," *Combustion science and technology*, vol. 174, no. 4, pp. 143–179, 2002.

[50] A. Lipatnikov and J. Chomiak, "Effects of premixed flames on turbulence and turbulent scalar transport," *Progress in Energy and Combustion Science*, vol. 36, no. 1, pp. 1–102, 2010.

[51] S. Kheirkhah and Ö. Gülder, "Turbulent premixed combustion in v-shaped flames: Characteristics of flame front," *Physics of Fluids*, vol. 25, no. 5, p. 055107, 2013.

[52] ——, "Topology and brush thickness of turbulent premixed v-shaped flames," *Flow, turbulence and combustion*, vol. 93, no. 3, pp. 439–459, 2014.

[53] B. Karlovitz, D. W. Denniston Jr, and F. E. Wells, "Investigation of turbulent flames," *The Journal of Chemical Physics*, vol. 19, no. 5, pp. 541–547, 1951.

[54] G. Taylor, "The statistical theory of isotropic turbulence," *Journal of the Aeronautical Sciences*, vol. 4, no. 8, pp. 311–315, 1937.

[55] F. Gouldin and K. Dandekar, "Time-resolved density measurements in premixed turbulent flames," *AIAA journal*, vol. 22, no. 5, pp. 655–663, 1984.

[56] P. Goix, P. Paranthoen, and M. Trinite, "A tomographic study of measurements in a v-shaped h2 air flame and a lagrangian interpretation of the turbulent flame brush evolution," *Combustion and Flame*, vol. 81, no. 3-4, pp. 229–241, 1990.

[57] P. Tamadonfar and Ö. L. Gülder, "Effects of mixture composition and turbulence intensity on flame front structure and burning velocities of premixed turbulent hydrocarbon/air bunsen flames," *Combustion and Flame*, vol. 162, no. 12, pp. 4417–4441, 2015.

[58] I. G. Shepherd and W. T. Ashurst, "Flame front geometry in premixed turbulent flames," *Symposium (International) on Combustion*, vol. 24, no. 1, pp. 485–491, 1992.

[59] I. Shepherd, "Flame surface density and burning rate in premixed turbulent flames," in *Symposium (International) on Combustion*, vol. 26, no. 1. Elsevier, 1996, pp. 373–379.

[60] I. G. Shepherd and R. K. Cheng, "The burning rate of premixed flames in moderate and intense turbulence," *Combustion and Flame*, vol. 127, no. 3, pp. 2066–2075, 2001.

[61] T. Lachaux, F. Halter, C. Chauveau, I. Gökalp, and I. Shepherd, "Flame front analysis of high-pressure turbulent lean premixed methane–air flames," *Proceedings of the Combustion Institute*, vol. 30, no. 1, pp. 819–826, 2005.

[62] F. Halter, C. Chauveau, and I. Gökalp, "Characterization of the effects of hydrogen addition in premixed methane/air flames," *International Journal of Hydrogen Energy*, vol. 32, no. 13, pp. 2585–2592, 2007.

[63] F. Yuen and Ö. L. Gülder, "Investigation of dynamics of lean turbulent premixed flames by rayleigh imaging," *AIAA J*, vol. 47, no. 12, pp. 2964–2973, 2009.

[64] C. Cohe, C. Chauveau, I. Gökalp, and D. F. Kurtuluş, "Co2 addition and pressure effects on laminar and turbulent lean premixed ch4 air flames," *Proceedings of the Combustion Institute*, vol. 32, no. 2, pp. 1803–1810, 2009.

[65] M. Zhang, J. Wang, Y. Xie, Z. Wei, W. Jin, Z. Huang, and H. Kobayashi, "Measurement on instantaneous flame front structure of turbulent premixed ch4/h2/air flames," *Experimental Thermal and Fluid Science*, vol. 52, pp. 288–296, 2014.

[66] M. Zhang, J. Wang, J. Wu, Z. Wei, Z. Huang, and H. Kobayashi, "Flame front structure of turbulent premixed flames of syngas oxyfuel mixtures," *international journal of hydrogen energy*, vol. 39, no. 10, pp. 5176–5185, 2014.

[67] I. Shepherd, R. Cheng, T. Plessing, C. Kortschik, and N. Peters, "Premixed flame front structure in intense turbulence," *Proceedings of the Combustion Institute*, vol. 29, no. 2, pp. 1833–1840, 2002.

[68] S. A. Filatyev, J. F. Driscoll, C. D. Carter, and J. M. Donbar, "Measured properties of turbulent premixed flames for model assessment, including burning velocities, stretch rates, and surface densities," *Combustion and Flame*, vol. 141, no. 1-2, pp. 1–21, 2005.

[69] S. Pope, "The evolution of surfaces in turbulence," *International journal of engineering science*, vol. 26, no. 5, pp. 445–469, 1988.

[70] F. Halter, C. Chauveau, I. Gökalp, and D. Veynante, "Analysis of flame surface density measurements in turbulent premixed combustion," *Combustion and Flame*, vol. 156, no. 3, pp. 657–664, 2009.

[71] C. Lawn and R. Schefer, "Scaling of premixed turbulent flames in the corrugated regime," *Combustion and flame*, vol. 146, no. 1-2, pp. 180–199, 2006.

[72] I. Shepherd and R. Cheng, "The burning rate of premixed flames in moderate and intense turbulence," *Combustion and Flame*, vol. 127, no. 3, pp. 2066–2075, 2001.

[73] H.-P. Schmid, P. Habisreuther, and W. Leuckel, "A model for calculating heat release in premixed turbulent flames," *Combustion and Flame*, vol. 113, no. 1-2, pp. 79–91, 1998.

[74] H. Kawanabe, M. Shioji, T. Tsunooka, and Y. Ali, "Cfd simulation for predicting combustion and pollutant formation in a homogeneous-charge spark-ignition engine," in *International Symposium COMODIA*, vol. 98, 1998, pp. 233–238.

[75] N. Peters, "The turbulent burning velocity for large-scale and small-scale turbulence," *Journal of Fluid mechanics*, vol. 384, pp. 107–132, 1999.

[76] ——, *Turbulent combustion*. Cambridge university press, 2000.

[77] B. Videto and D. Santavicca, "A turbulent flow system for studying turbulent combustion processes," *Combustion Science and technology*, vol. 76, no. 1-3, pp. 159–164, 1991.

[78] A. W. Skiba, T. M. Wabel, C. D. Carter, S. D. Hammack, J. E. Temme, and J. F. Driscoll, "Premixed flames subjected to extreme levels of turbulence part i: Flame structure and a new measured regime diagram," *Combustion and Flame*, vol. 189, pp. 407–432, 2018.

[79] B. D. Videto and D. A. Santavicca, "Flame-Turbulence Interactions in a Freely-Propagating, Premixed Flame," *Combustion Science and Technology*, vol. 70, no. 1-3, pp. 47–73, 1990.

[80] K. Thole, D. Bogard, and J. Whan-Tong, "Generating high freestream turbulence levels," *Experiments in Fluids*, vol. 17, no. 6, pp. 375–380, 1994.

[81] I. Castro, "perforated plates normal to an air-stream," *J. Fluid Mech*, vol. 46, no. part 3, pp. 599–609, 1971.

[82] R. Liu, D. S. Ting, and G. W. Rankin, "On the generation of turbulence with a perforated plate," *Experimental Thermal and Fluid Science*, vol. 28, no. 4, pp. 307–316, 2004.

[83] R. Liu and D. S.-K. Ting, "Turbulent flow downstream of a perforated plate: sharp-edged orifice versus finite-thickness holes," *Journal of Fluids Engineering*, vol. 129, no. 9, pp. 1164–1171, 2007.

[84] R. Liu, D. S.-K. Ting, and M. D. Checkel, "Constant reynolds number turbulence downstream of an orificed perforated plate," *Experimental thermal and fluid science*, vol. 31, no. 8, pp. 897–908, 2007.

[85] W. Quinn, "Upstream nozzle shaping effects on near field flow in round turbulent free jets," *European Journal of Mechanics-B/Fluids*, vol. 25, no. 3, pp. 279–301, 2006.

[86] G. Coppola and A. Gomez, "Experimental investigation on a turbulence generation system with high-blockage plates," *Experimental Thermal and Fluid Science*, vol. 33, no. 7, pp. 1037–1048, 2009.

[87] F. C. Nicolleau, S. M. Salim, and A. F. Nowakowski, "Experimental study of a turbulent pipe flow through a fractal plate," *Journal of Turbulence*, vol. 12, no. July, p. N44, 2011.

[88] A. Marshall, P. Venkateswaran, D. Noble, J. Seitzman, and T. Lieuwen, "Development and characterization of a variable turbulence generation system," *Experiments in Fluids*, vol. 51, no. 3, p. 611, 2011.

[89] S. H. Won, B. Jiang, B. C. Windom, S. Hammack, T. Ombrello, and C. D. Carter, "Detailed Characterization of Low Temperature Chemistry and Turbulence Interaction in Reactor-Assisted Turbulent," *52nd Aerospace Sciences Meeting*, no. January, pp. 1–8, 2014.

[90] B. Sundaram, A. Klimenko, M. Cleary, and U. Maas, "Prediction of nox in premixed high-pressure lean methane flames with a mmc-partially stirred reactor," *Proceedings of the Combustion Institute*, vol. 35, no. 2, pp. 1517–1525, 2015.

[91] A. W. Skiba, T. M. Wabel, J. Temme, and J. F. Driscoll, "Experimental assessment of premixed flames subjected to extreme turbulence," in *54th AIAA Aerospace Sciences Meeting*, 2016, p. 1454.

[92] T. M. Wabel, A. W. Skiba, and J. F. Driscoll, "Turbulent burning velocity measurements: Extended to extreme levels of turbulence," *Proceedings of the Combustion Institute*, vol. 36, no. 2, pp. 1801–1808, 2017.

[93] A. Marshall, "Turbulent Flame Propagation Characteristics of High Hydrogen Content Fuels," *Dissertation*, no. August, 2015.

[94] A. Marshall, J. Lundrigan, P. Venkateswaran, J. Seitzman, and T. Lieuwen, "Measurements of Stretch Statistics at Flame Leading Points for High Hydrogen Content Fuels," in *Proceedings of ASME Turbo Expo 2014, June 16 20, 2014, Düsseldorf, Germany*, 2014, pp. 2014–26 420.

[95] S. Horender, "Turbulent flow downstream of a large solidity perforated plate: near-field characteristics of interacting jets," *Fluid Dynamics Research*, vol. 45, no. 2, p. 025501, 2013.

[96] P. Venkateswaran, A. D. Marshall, J. M. Seitzman, and T. C. Lieuwen, "Turbulent Consumption Speeds of High Hydrogen Content Fuels From 120 atm," *Journal of Engineering for Gas Turbines and Power*, vol. 136, no. 1, p. 011504, 2013.

[97] B. Windom, S. H. Won, T. Wada, B. Jiang, and Y. Ju, "Study of turbulent flame propagation and surface characteristics at large reynolds numbers," *51st AIAA Aerospace Sciences Meeting including the New Horizons Forum and Aerospace Exposition 2013*, no. January, pp. 1–9, 2013.

[98] J. Wang, F. Matsuno, M. Okuyama, Y. Ogami, H. Kobayashi, and Z. Huang, "Flame front characteristics of turbulent premixed flames diluted with CO2 and H2O at high pressure and high temperature," *Proceedings of the Combustion Institute*, vol. 34, no. 1, pp. 1429–1436, 2013.

[99] A. D. Marshall, P. Venkateswaran, J. M. Seitzman, and T. C. Lieuwen, "Pressure Effects on the Turbulent Consumption Speeds of High H2 Mixtures," *Volume 2: Combustion, Fuels and Emissions, Parts A and B*, p. 231, 2012.

[100] K. S. Kedia and A. F. Ghoniem, "Mechanisms of stabilization and blowoff of a premixed flame downstream of a heat-conducting perforated plate," *Combustion and Flame*, vol. 159, no. 3, pp. 1055–1069, 2012.

[101] C. W. Chiu, Y. C. Dong, and S. S. Shy, "High-pressure hydrogen/carbon monoxide syngas turbulent burning velocities measured at constant turbulent Reynolds numbers," *International Journal of Hydrogen Energy*, vol. 37, no. 14, pp. 10 935–10 946, 2012.

[102] R. S. Barlow, M. J. Dunn, M. S. Sweeney, and S. Hochgreb, "Effects of preferential transport in turbulent bluff-body-stabilized lean premixed CH 4/air flames," *Combustion and Flame*, vol. 159, no. 8, pp. 2563–2575, 2012.

[103] M. Day, S. Tachibana, J. Bell, M. Lijewski, V. Beckner, and R. K. Cheng, "A combined computational and experimental characterization of lean premixed turbulent low swirl laboratory flames I. Methane flame," *Combustion and Flame*, vol. 159, no. 1, pp. 275–290, 2012.

[104] ——, "A combined computational and experimental characterization of lean premixed turbulent low swirl laboratory flames II. Hydrogen flames," *Combustion and Flame*, vol. 162, no. 5, pp. 2148–2165, 2015.

[105] N. Mazellier, L. Danaila, and B. Renou, "Multi-scale energy injection: a new tool to generate intense homogeneous and isotropic turbulence for premixed combustion," *Journal of Turbulence*, vol. 11, no. May, p. N43, 2010.

[106] T. Sponfeldner, S. Henkel, N. Soulopoulos, F. Beyrau, Y. Hardalupas, A. Taylor, and J. Vassilicos, "A parametric study of the effect of fractal-grid generated turbulence on the structure of premixed flames," in *European Combustion Meeting*, 2011.

[107] M. F. Othman, B. Manshoor, and A. Khalid, "Circle grid fractal plate as a turbulent generator for premixed flame: an overview," in *IOP Conference Series: Materials Science and Engineering*, vol. 50, no. 1. IOP Publishing, 2013, p. 012050.

[108] F. Scarano, "Tomographic piv: principles and practice," *Measurement Science and Technology*, vol. 24, no. 1, p. 012001, 2012.

[109] K. D. Hinsch, "Holographic particle image velocimetry," *Measurement Science and Technology*, vol. 13, no. 7, p. R61, 2002.

[110] A. K. Prasad, "Stereoscopic particle image velocimetry," *Experiments in fluids*, vol. 29, no. 2, pp. 103–116, 2000.

[111] M. Gharib, M. Raffel, O. Ronneberger, and J. Kompenhans, "Feasibility study of three-dimensional piv by correlating images of particles within parallel light sheet planes," *Experiments in Fluids*, vol. 19, no. 2, pp. 69–77, 1995.

[112] J. Westerweel, G. E. Elsinga, and R. J. Adrian, "Particle image velocimetry for complex and turbulent flows," *Annual Review of Fluid Mechanics*, vol. 45, pp. 409–436, 2013.

[113] M. Raffel, C. E. Willert, F. Scarano, C. J. Kähler, S. T. Wereley, and J. Kompenhans, *Particle image velocimetry: a practical guide*. Springer, 2018.

[114] R. J. Adrian and J. Westerweel, *Particle image velocimetry*. Cambridge University Press, 2011, no. 30.

[115] M. Stanislas, J. Kompenhans, and J. Westerweel, *Particle image velocimetry: Progress towards industrial application*. Springer Science & Business Media, 2013, vol. 56.

[116] A. Schroeder and C. E. Willert, *Particle image velocimetry: new developments and recent applications*. Springer Science & Business Media, 2008, vol. 112.

[117] C. Willert, "Stereoscopic digital particle image velocimetry for application in wind tunnel flows," *Measurement science and technology*, vol. 8, no. 12, p. 1465, 1997.

[118] S. M. Soloff, R. J. Adrian, and Z.-C. Liu, "Distortion compensation for generalized stereoscopic particle image velocimetry," *Measurement science and technology*, vol. 8, no. 12, p. 1441, 1997.

[119] A. C. Eckstein, J. Charonko, and P. Vlachos, "Phase correlation processing for DPIV measurements," *Experiments in Fluids*, vol. 45, no. 3, pp. 485–500, 2008.

[120] A. Eckstein and P. P. Vlachos, "Assessment of advanced windowing techniques for digital particle image velocimetry (DPIV)," *Measurement Science and Technology*, vol. 20, no. 7, p. 075402, 2009.

[121] ——, "Digital particle image velocimetry (DPIV) robust phase correlation," *Measurement Science and Technology*, vol. 20, no. 5, p. 055401, 2009.

[122] B. M. Wilson and B. L. Smith, "Uncertainty on PIV mean and fluctuating velocity due to bias and random errors," *Measurement Science and Technology*, vol. 24, no. 3, p. 035302, 2013.

[123] M. P. Wernet, "Symmetric phase only filtering: a new paradigm for dpiv data processing," *Measurement Science and Technology*, vol. 16, no. 3, p. 601, 2005.

[124] D. P. Hart, "The elimination of correlation errors in piv processing," in *9th International Symposium on Applications of Laser Techniques to Fluid Mechanics*, 1998, pp. 13–16.

[125] ——, "Piv error correction," *Experiments in fluids*, vol. 29, no. 1, pp. 13–22, 2000.

[126] J. Westerweel, D. Dabiri, and M. Gharib, "The effect of a discrete window offset on the accuracy of cross-correlation analysis of digital piv recordings," *Experiments in fluids*, vol. 23, no. 1, pp. 20–28, 1997.

[127] F. Scarano and M. L. Riethmuller, "Iterative multigrid approach in piv image processing with discrete window offset," *Experiments in Fluids*, vol. 26, no. 6, pp. 513–523, 1999.

[128] A. Sciacchitano, F. Scarano, and B. Wieneke, "Multi-frame pyramid correlation for time-resolved piv," *Experiments in fluids*, vol. 53, no. 4, pp. 1087–1105, 2012.

[129] F. Scarano, "Iterative image deformation methods in piv," *Measurement science and technology*, vol. 13, no. 1, p. R1, 2001.

[130] J. Westerweel, "Efficient detection of spurious vectors in particle image velocimetry data," *Experiments in Fluids*, vol. 16, no. 3-4, pp. 236–247, 1994.

[131] J. Westerweel and F. Scarano, "Universal outlier detection for piv data," *Experiments in fluids*, vol. 39, no. 6, pp. 1096–1100, 2005.

[132] S. Bhattacharya, J. J. Charonko, and P. P. Vlachos, "Stereo-particle image velocimetry uncertainty quantification," *Measurement Science and Technology*, vol. 28, no. 1, p. 015301, 2017.

[133] A. Boomsma, S. Bhattacharya, D. Troolin, S. Pothos, and P. Vlachos, "A comparative experimental evaluation of uncertainty estimation methods for two-component PIV," *Measurement Science and Technology*, vol. 27, no. 9, p. 094006, 2016.

[134] A. Sciacchitano, D. R. Neal, B. L. Smith, S. O. Warner, P. P. Vlachos, B. Wieneke, and F. Scarano, "Collaborative framework for PIV uncertainty quantification: comparative assessment of methods," *Measurement Science and Technology*, vol. 26, no. 7, p. 074004, 2015.

[135] Z. Xue, J. J. Charonko, and P. P. Vlachos, "Particle image velocimetry correlation signal-to-noise ratio metrics and measurement uncertainty quantification," *Measurement Science and Technology*, vol. 25, no. 11, p. 115301, 2014.

[136] A. Sciacchitano, B. Wieneke, and F. Scarano, "Piv uncertainty quantification by image matching," *Measurement Science and Technology*, vol. 24, no. 4, p. 045302, 2013.

[137] Z. Xue, J. Charonko, and P. Vlachos, "Signal-to-noise ratio, error and uncertainty of PIV measurement," *10th International Symposium on Particle Image Velocimetry*, 2013.

[138] B. Hof, C. W. van Doorne, J. Westerweel, F. T. Nieuwstadt, H. Faisst, B. Eckhardt, H. Wedin, R. R. Kerswell, and F. Waleffe, "Experimental observation of nonlinear traveling waves in turbulent pipe flow," *Science*, vol. 305, no. 5690, pp. 1594–1598, 2004.

[139] A. Kalpakli and R. Örlü, "Turbulent pipe flow downstream a 90?? pipe bend with and without superimposed swirl," *International Journal of Heat and Fluid Flow*, vol. 41, pp. 103–111, 2013.

[140] M. El Hassan and A. Meslem, "Time-resolved stereoscopic particle image velocimetry investigation of the entrainment in the near field of circular daisy-shaped orifice jets," *Physics of Fluids*, vol. 22, no. 3, pp. 7–26, 2010.

[141] S. Herpin, C. Y. Wong, M. Stanislas, and J. Soria, "Stereoscopic PIV measurements of a turbulent boundary layer with a large spatial dynamic range," *Experiments in Fluids*, vol. 45, no. 4, pp. 745–763, 2008.

[142] M. Tanahashi, T. Hirayama, S. Taka, and T. Miyauchi, "Measurement of fine scale structure in turbulence by time-resolved dual-plane stereoscopic PIV," *International Journal of Heat and Fluid Flow*, vol. 29, no. 3, pp. 792–802, 2008.

[143] I. Boxx, C. Slabaugh, P. Kutne, R. P. Lucht, and W. Meier, "3 kHz PIV/OH-PLIF measurements in a gas turbine combustor at elevated pressure," *Proceedings of the Combustion Institute*, vol. 35, no. 3, pp. 3793–3802, 2015.

[144] J. Weinkauff, P. Trunk, J. H. Frank, M. J. Dunn, A. Dreizler, and B. B??hm, "Investigation of flame propagation in a partially premixed jet by high-speed-Stereo-PIV and acetone-PLIF," *Proceedings of the Combustion Institute*, vol. 35, no. 3, pp. 3773–3781, 2015.

[145] P. J. Trunk, I. Boxx, C. Heeger, W. Meier, B. Böhm, and A. Dreizler, "Premixed flame propagation in turbulent flow by means of stereoscopic PIV and dual-plane OH-PLIF at sustained kHz repetition rates," *Proceedings of the Combustion Institute*, vol. 34, no. 2, pp. 3565–3572, 2013.

[146] A. M. Steinberg, J. F. Driscoll, and S. L. Ceccio, "Three-dimensional temporally resolved measurements of turbulence-flame interactions using orthogonal-plane cinema-stereoscopic PIV," *Experiments in Fluids*, vol. 47, no. 3, pp. 527–547, 2009.

[147] ——, "Measurements of turbulent premixed flame dynamics using cinema stereoscopic PIV," *Experiments in Fluids*, vol. 44, no. 6, pp. 985–999, 2008.

[148] P. Petersson, J. Olofsson, C. Brackman, H. Seyfried, J. Zetterberg, M. Richter, M. Aldén, M. A. Linne, R. K. Cheng, A. Nauert, D. Geyer, and A. Dreizler, "Simultaneous PIV/OH-PLIF, Rayleigh thermometry/OH-PLIF and stereo PIV measurements in a low-swirl flame," *Applied Optics*, vol. 46, no. 19, p. 3928, 2007.

[149] J. M. Seitzman, R. K. Hanson, P. DeBarber, and C. Hess, "Application of quantitative two-line oh planar laser-induced fluorescence for temporally resolved planar thermometry in reacting flows," *Applied Optics*, vol. 33, no. 18, pp. 4000–4012, 1994.

[150] B. Hiller and R. K. Hanson, "Simultaneous planar measurements of velocity and pressure fields in gas flows using laser-induced fluorescence," *Applied Optics*, vol. 27, no. 1, pp. 33–48, 1988.

[151] G. Kychakoff, R. D. Howe, and R. K. Hanson, "Quantitative flow visualization technique for measurements in combustion gases," *Applied optics*, vol. 23, no. 5, pp. 704–712, 1984.

[152] C. D. Carter, S. Hammack, and T. Lee, "High-speed planar laser-induced fluorescence of the CH radical using the C2??+ - X2??(0, 0) band," *Applied Physics B: Lasers and Optics*, vol. 116, no. 3, pp. 515–519, 2014.

[153] H. Najm, O. Knio, P. Paul, and P. Wyckoff, "A study of flame observables in premixed methane-air flames," *Combustion Science and Technology*, vol. 140, no. 1-6, pp. 369–403, 1998.

[154] J. B. Jeffries, R. A. Copeland, and D. R. Crosley, "Transition probabilities in the c2+-x2 ii system of ch," *Journal of Quantitative Spectroscopy and Radiative Transfer*, vol. 37, no. 5, pp. 419–423, 1987.

[155] R. K. Hanson, R. M. Spearrin, and C. S. Goldenstein, *Spectroscopy and optical diagnostics for gases*. Springer, 2016.

[156] S. Pfadler, F. Beyrau, and A. Leipertz, "Flame front detection and characterization using conditioned particle image velocimetry (cpiv)," *Optics Express*, vol. 15, no. 23, pp. 15 444–15 456, 2007.

[157] D. Han, A. Satija, J. Kim, Y. Weng, J. Gore, and R. Lucht, "Dual-pump vibrational CARS measurements of temperature and species concentrations in turbulent premixed flames with CO¡inf¿2¡/inf¿ addition," *Combustion and Flame*, vol. 181, 2017.

[158] J. Temme, T. M. Wabel, A. W. Skiba, and J. F. Driscoll, "Measurements of premixed turbulent combustion regimes of high reynolds number flames," in *53rd AIAA Aerospace Sciences Meeting*, 2015, p. 0168.

[159] M. Thurber and R. Hanson, "Simultaneous imaging of temperature and mole fraction using acetone planar laser-induced fluorescence," *Experiments in Fluids*, vol. 30, no. 1, pp. 93–101, 2001.

[160] A. Eckstein and P. P. Vlachos, "Digital particle image velocimetry (dpiv) robust phase correlation," *Measurement Science and Technology*, vol. 20, no. 5, p. 055401, 2009.

[161] B. Wieneke, "Stereo-PIV using self-calibration on particle images," *Experiments in Fluids*, vol. 39, no. 2, pp. 267–280, 2005.

[162] A. C. Eckstein, J. Charonko, and P. Vlachos, "Phase correlation processing for dpiv measurements," *Experiments in Fluids*, vol. 45, no. 3, pp. 485–500, 2008.

[163] C. J. Kähler, T. Astarita, P. P. Vlachos, J. Sakakibara, R. Hain, S. Discetti, R. La Foy, and C. Cierpka, "Main results of the 4th International PIV Challenge," *Experiments in Fluids*, vol. 57, no. 6, 2016.